ALMA MATER STUDIORUM
UNIVERSITÀ DI BOLOGNA

DOTTORATO DI RICERCA IN

CHIMICA

Ciclo 37

Settore Concorsuale: 03/A2 - MODELLI E METODOLOGIE PER LE SCIENZE CHIMICHE

Settore Scientifico Disciplinare: CHIM/02 - CHIMICA FISICA

IMPROVING SUSTAINABILITY OF ELECTROCHEMICAL ENERGY STORAGE SYSTEMS ADOPTING NOVEL SOLUTIONS FOR DIFFERENT DEVICE COMPONENTS

Presentata da: Luca Bargnesi

Coordinatore Dottorato

Cristina Puzzarini

Supervisore

Catia Arbizzani

Co-supervisore

Massimo Marcaccio

Esame finale anno 2025

Abstract

My Ph. D work was focused on sustainable and safer energy storage systems. For that, I've considered to increase the overall sustainability of batteries through the implementation of biopolymers and to stabilize the life cycle and stability of lithium metal anodes that guarantees the highest energy density. At the very beginning I studied the implementation of chitosan, a renewable and biodegradable as binder for electrodes processed in aqueous environment and operating in different environments. With the experience gained with chitosan I tried to obtain a separator made of partially biodegradable polymers with phase inversion technique that could also be adopted for industrial production processes. In the end I tried to extend the idea of using biopolymers in batteries components by investigating the feasibility of polymeric electrolyte made of cellulose to increase the sustainability of the cells as well as improving the safety of lithium metal anodes reducing the risk of short circuits and cell failures.

Context

Over the past few decades, a deeper understanding of environmental processes has raised awareness of human-induced climate change and its alarming consequences for future generations. Today, one of the major causes of rising global temperatures is the greenhouse gas CO_2, which is predominantly produced by the burning of fossil fuels for energy generation and transportation [1–6].

Moreover, taking into account the rising demand for energy, driven especially by the Asiatic developing countries, nearly the entire global community committed to the Paris Agreement in 2015 with the aim to reduce greenhouse gas emissions and stabilize global temperatures. The agreement aims to facilitate a widespread transition to clean energy production and usage, incorporating renewable energy sources (RES) such as solar and wind power, along with emission-free transportation [7–9]. Government policies, social movements, advancements in renewable energy technologies, current installation trends, and research from both academia and industry are all pointing toward a future electricity sector free of emissions [10,11].

The integration of RES into the main electric grid presents several technical challenges as imbalances between peak generation and peak demand, and voltage fluctuations due to production variability depending on weather conditions. Therefore RES, can provide clean energy but with the cost of stability distress and technical challenges yet to be resolved. Among the various energy storage technologies, electrochemical energy storage systems (EESS) gained a lot of resonance and interest over the past decades and emerged as the most promising candidates to address the challenges emerged by the implementation of RES in the electric power grid, particularly by

improving power system stability. EESS includes several devices based on different technologies, including batteries, supercapacitor and electrolytic capacitors [12–18].

Currently, rechargeable lithium - ion batteries (LIBs) are the EESSs that attract most interest, also because of their widespread application, largely due to recent advancements in technology and significant reductions in costs. Additionally, the range of services that batteries can provide has expanded considerably over the past decade, ranging from portable devices to hybrid and electric vehicles (EVs), up to stationary storage systems. [19–22]. However, the ever-increasing number of LIBs on the market to support RES implementation into the grid and mobility electrification, pose the question of the environmental impact of LIBs production and end of life [23–25]. Therefore, to achieve the carbon neutrality and Paris agreement targets, it is essential the switch towards clean energy production, coupled with the design and development of more environmentally friendly batteries. Batteries with increasing specific and volumetric energy, especially for EVs, with anodes based on Si-graphite or lithium metal, are also under study. Lithium metal batteries (LMBs) are the 4th generation batteries, which can achieve specific energy of the order of 500 Wh kg^{-1}. However, the reactivity of lithium and the formation of dendrites during the LMBs charging process are still the main concerns. Understanding the processes occurring at the Li/electrolyte interphase is of paramount importance for improving LMBs stability and safety.

Aim of the thesis

The key objective of this thesis was to increase the overall sustainability and security of LIBs, adopting a multi-pronged approach. The first approach was the replacement of conventional fluorinated polymers used either as binder for the electrodes or separator between anode and cathode, with biopolymers, which are obtained from renewable source and feature biodegradation. In addition, aqueous processing of different batteries components, such as electrodes and separator, was investigated, to further reduce the environmental impact of LIBs production, and a novel electrode formulation was developed for "self-standing" electrodes that didn't need the use of a current collector. In parallel, to increase the safety and life cycle of lithium metal anodes for LMBs, different ammonium salts were evaluated as additives for liquid electrolytes. Lastly, functionalized cellulose in polymer blend has been synthesized and used as polymer electrolyte (PE) for solid state batteries (SSB). PEs feature a good electrochemical stability and compatibility with lithium metal anodes and, crucially, could meet the requirements of safety, by reducing fire hazard following failures, and sustainability, avoiding the use of volatile organic solvents and possibly obtaining the electrolyte from renewable feedstocks or with less impactful processes.

1. Introduction

This chapter gives a brief overview of different energy storage technologies and the importance of the current energy transition.

1.1 Energy needs

Energy, especially electrical energy, is essential for sustaining our standard of living. Figure 1.1 shows that in 2023 global human activity consumed 592 quadrillion BTUs (equivalent to 606.7 × 10^{18} joules (exaJ)) [26], and this demand is projected to increase by 28%, reaching 730 quadrillion BTUs (or 776.5 × 10^{18} joules) by 2040 [27]. More than 75% of the electricity is generated through fossil fuels (coal, natural gas and petroleum); the reasons behind that domination in global electricity production are the reliability of power supply and the cheapness of sourcing [27,28].
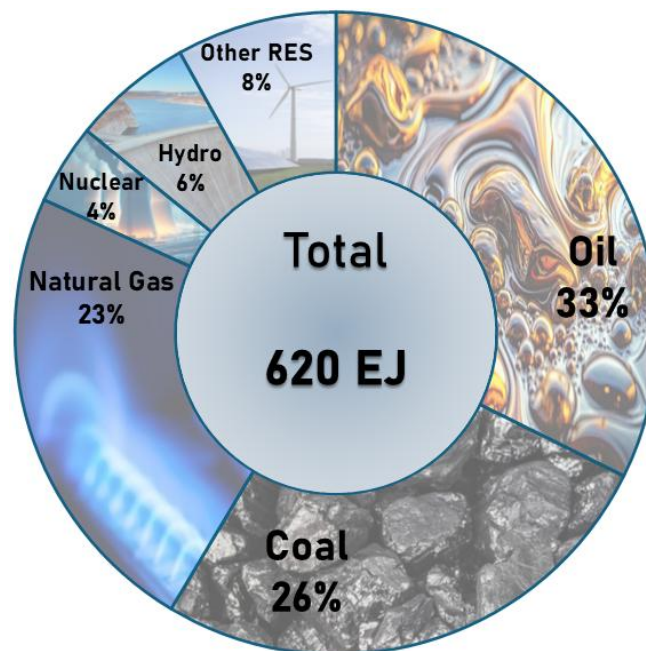
Figure 1.1 Global primary energy consumption by fuel, in exajoules, in 2023. Data is from the Energy Institute, 2024 Statistical Review of World Energy [26]

The massive usage of fossil sources over the decades has significantly contributed to raise the CO_2 amount in the atmosphere, reaching last year the maximum value of 420 ppmv [29,30]. CO_2 plays a key role in regulating the planet temperature. It absorbs infrared radiation emitted from Earth's surface, and re-radiates it in all directions, including back toward the surface, creating a "greenhouse effect" that maintains Earth's average temperature near 16°C [31].

Following increasing and significant social, political and environmental pressures to reduce carbon emissions, in 2015 UN Climate Change Conference in Paris, all countries agreed to reduce carbon emissions to mitigate the impacts of climate change. The goal of 2015 Paris Agreement is to combat climate change by limiting global warming below 2°C above pre-industrial levels, with efforts to limit the temperature increase even further to 1.5°C, by the year 2100. However, its success depends on countries' commitments and actions to fulfil their goals [7].

Given these constraints of climate change policies and the need for independence from fossil fuel reserves, energy sources must now meet new criteria of being both emission-free and renewable. Hydropower, geothermal, tidal, eolic and photovoltaic, represents nowadays the already established and known RES, as could be seen in Figure 1.2, appearing to be the most viable alternatives [32]. Certain RES pose challenges for power generation due to their intermittent and unpredictable availability. Electricity demand fluctuates both seasonally and throughout the day, making it difficult to increase the share of RES, while gradually phasing out conventional sources evidence significant challenge for energy grids [29,32].

Renewable Energy Capacity Through Time
2000–2023

Global renewable energy capacity has grown by 415% since 2000.

Here's how each region has contributed to this growth.

World Total in 2000: 752 GW

	2023 Additions (GW)	Total Capacity (GW)
China	298	1,454
Europe	71	787
U.S.	31	388
Asia (excl. China & India)	17	331
Brazil	17	194
India	13	176
Canada	2	109
South America (excl. Brazil)	5	95
Africa	3	62
Rest of World	16	274
World Total	473	3,870

Source: IRENA
Renewables include solar, wind, hydro (excluding pumped storage), bioenergy, geothermal, and marine energy

Figure 1.2 Evolution of installed capacity of world region since 2000, using the latest data from the International Renewable Energy Agency (IRENA)[33]

1.2 Energy storage systems

Given that electricity is the most versatile form of energy, capable of being transmitted over vast distances and distributed to consumers with minimal losses, energy storage systems (ESS) have gained significant interest. They are the most feasible option to regulate load peaks requests and overcome the gap between the installed capacities for intermittent sources, such as solar and wind, and the actual amounts of electricity they generated, in pursuit of achieving a clean and sustainable energy future [34,35].

Specifically, ESS technologies can be categorized according to various factors, such as storage duration (short-term, mid-term, or long-term), response time (fast or slow),

scale (small, medium, or large), form of energy stored (electrochemical, magnetic, or mechanical). ESS requirements are highly varied and depend largely on the specific application. No single technology can fulfil all the necessary criteria or metrics for large-scale, grid-quality storage [32,36]. "Electrochemical systems" is a subcategory of ESS (Figure 1.3) that includes batteries and hydrogen storage with fuel cells, as well as supercapacitors. For applications where rapid adjustments and regulations are essential, EESS family represent a viable option either for large - scale applications or for systems where lightness and compact dimensions are the main requirements [36–38].
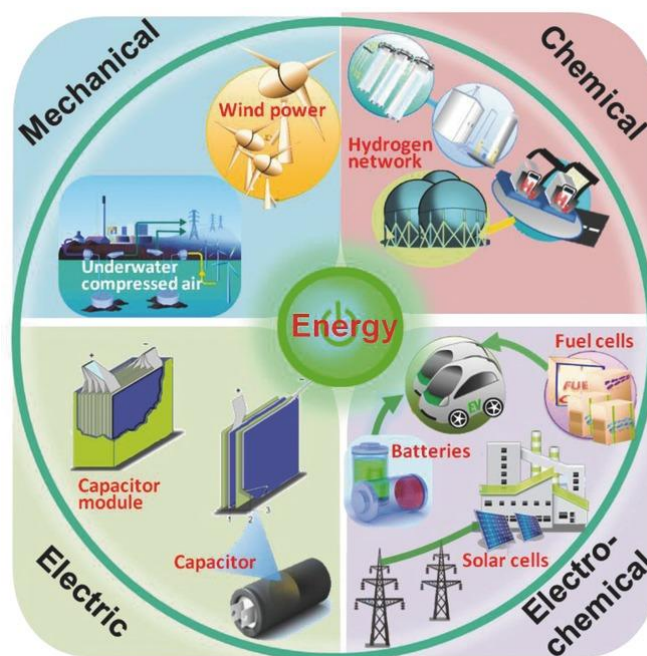
Figure 1.3 Classification of different energy storage/conversion technologies [39]

While several technologies, such as lead - acid (Pb - acid), and sodium - sulfur (NaS), are already proven and fully integrated for large - scale stationary use, other systems are current under developing or at prototyping stages, e.g. redox flow batteries. The significant portion of current energy storage research is focused on improving LIBs or alternative battery chemistries to address some of the existing limitations of LIBs. This

focus is especially driven by the widespread use of lithium-ion technology in everything from electric vehicles EVs to consumer electronics and grid small-scale energy storage, e.g. domestic, small business or localized applications [37,40,41].

1.3 Electrochemical energy storage systems overview

The fundamental operating principle of electrochemical devices involves three main processes: charge separation, transport of charged species, and charge recombination. This principle applies to a wide range of devices, including batteries, supercapacitors and electrolytic capacitors, and photoelectrochemical devices. However, each type operates through different mechanisms, with interfaces playing a critical role [42,43]. Focusing on conventional batteries, they are closed systems where the anode and cathode store the charge and serve as the charge-transfer medium and actively participate in the redox reactions as "active masses". Therefore, the materials required for each electrochemical system vary significantly, and many of these have been extensively reviewed. Batteries, fuel cells and supercapacitors all share a common structure consisting of two electrodes in contact with an electrolyte solution, as shown in Figure 1.4 [44]. The requirements for electron and ion conduction within the electrodes and electrolyte, respectively, apply to all the three systems.
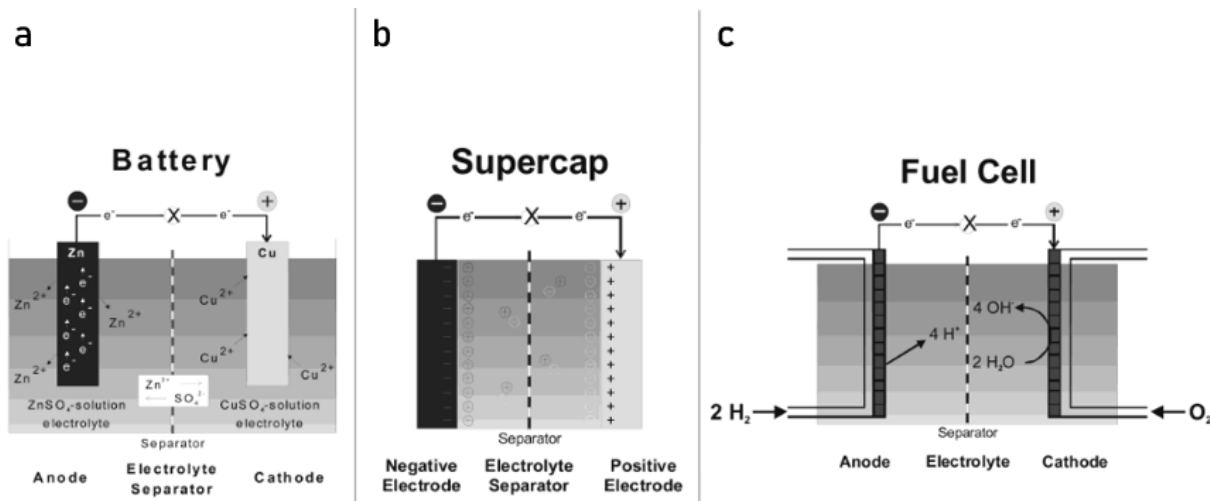
Figure 1.4 Representation of energy conversion in different electrochemical systems: a) battery (Daniell cell) showing the key features of battery operation and the requirements of electron and ion conduction, b) an electrochemical capacitor (supercapacitor), with the energy conversion relying in the electric double layers at the electrode interfaces, and c) a fuel cell with energy conversion relying in the continuous supply of reactants (hydrogen and oxygen at the anode and cathode respectively) and the corresponding redox reactions.[44]

In batteries, which can be secondary or primary depending on if they are rechargeable or not, the spontaneous process is the discharge. The anode, where the oxidation occurs, typically operates at lower electrode potentials than the cathode, where reduction occurs. For this reason, the terms "negative" and "positive" electrodes, as well as the terms anode and cathode, independently from the fact that the discharge or the charge is considered. [44,45].

As can be seen, batteries are highly efficient devices for storing electrical energy and are widely used in various applications, including transportation, portable and mobile devices, as well as stationary backup power systems. In general, they provide desirable solutions for cost-effective and compact energy storage, offering pollution-free operation, high overall efficiency, adequate cycle life, and considerable shelf and service life [29,41,46].

Secondary batteries, depending on the materials used for their electrodes and electrolytes, can be classified into several types: lead-acid, alkaline, metal-air, high-temperature batteries, and LIBs. The operational characteristics among different types are commonly shown using Ragone diagrams. As shown in Ragone plot in Figure 1.5, specific power is plotted against specific energy for most popular rechargeable battery systems, allowing for comparisons between various types of batteries and those based on lithium chemistry. The superior properties of lithium - based technologies, with the best compromise of energy and power, as highlighted in Figure 1.5, explain the substantial market success of this technology [38,47].
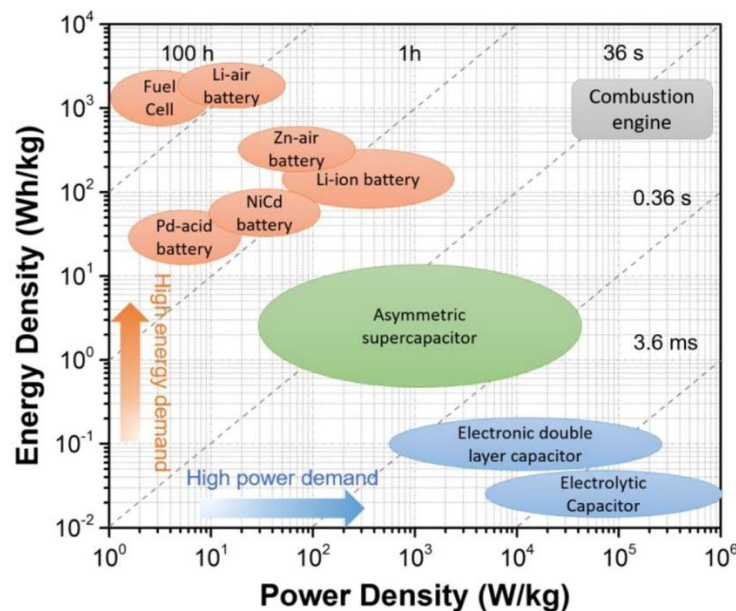
Figure 1.5 Ragone plot illustrating the performances of specific power vs specific energy for different electrochemical systems. Times shown in the plot are the discharge time, obtained by dividing the energy density by the power density [48]

2. Electrochemical energy storage systems

2.1 Lithium ion batteries components

Beyond their different chemistries, all batteries share certain fundamental elements. They could consist of one or more electrochemical cells connected in series or parallel configurations to achieve the desired voltage and capacity [29,49].

As could be seen in Figure 2.1, each cell, typically features two electrodes (positive and negative), a separator in between them soaked with an electrolyte solution.
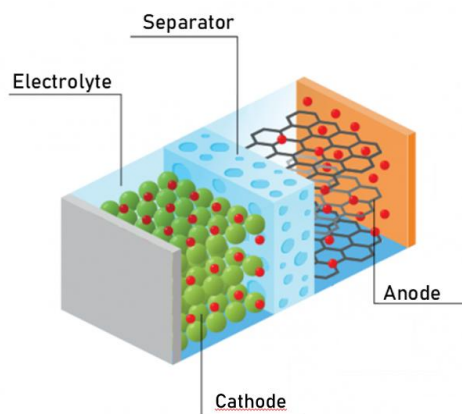
Figure 2.1 Schematic diagram of the fundamental components of a LIB cell

The positive and negative electrodes, more frequently called cathode and anode respectively, serve as charge carriers that contribute to the storage and release of energy; therefore, they should exhibit certain properties:

o The material used as the negative electrode should have a low reduction potential, while the material for the positive electrode should have a high reduction potential. This setup requires the negative electrode to have a high

8

Fermi energy, yet it must remain below the lowest unoccupied molecular orbital (LUMO) of the electrolyte. Similarly, the positive electrode should have a low Fermi energy, staying above the highest occupied molecular orbital (HOMO) of the electrolyte. These conditions ensure compatibility of the electrode materials within the electrolyte's stability window [50].

o For electrochemically active electrodes, reversible faradaic reactions should come with minimal volume changes. This helps to limit structural variations, maintaining stable electrical contact and consequently long cycle life.

o Electrode material should be as lightweight as possible to achieve a high specific capacity, as cells with elevated potentials and high specific capacities are associated with high specific energies.

o Sufficiently high electronic and ionic conductivity (particularly important for metal-ion batteries) along with low charge transfer resistance to facilitate electrode kinetics, thereby ensuring high battery power.

o Adopt environmentally friendly and low-cost materials and production processes as far as possible.

While the electrolyte facilitates ion transport and ionically connects the electrodes, the separator physically divides the electrodes to prevent internal short circuits, allowing the flow of lithium ions (Li^+). It must be chemically and electrochemically stable towards the electrolyte and electrode materials. Structurally, the separator should have enough porosity to retain the liquid electrolyte effectively while also providing high ionic conductivity. Although it does not directly engage with the electrochemical reactions within the cell, the separator adds electrical resistance to the system. Consequently, its structure and properties play a critical role in influencing the overall performance of the cell [51,52].

Malfunctions in any of these components can negatively impact the safety of cells. During operation, depending on the electrode nature, they might generate heat from movement of Li^+ ions (Joule heating), which can severely compromise battery safety and irreversibly damage battery components and become uncontrollable in the event of a battery malfunction. Therefore, establishing appropriate safety regulations based on research into controllable and uncontrollable factors in battery failures is crucial for enhancing the safety performance of LIBs [53,54]. The next chapters will discuss in more details the individual constituents.

2.2 Principles of operation of a lithium-ion cell

A cell can be represented schematically with two electrodes separated by an electrically insulating membrane with an electrolytic medium permeating all these components. When a spontaneous redox reaction occurs, typically the discharging process, current flows through the external circuit. This is the basis of battery operation during discharge, where chemical energy from the reactants is converted into electrical energy. To recharge the cell, the reactants must be restored, requiring the reaction to proceed in the reverse direction. The opposite process is achieved by applying external electrical energy. During charging, electrical energy is converted back into chemical energy, making these cells suitable as storage systems thanks to the capability of reversible energy conversion [55].

The working mechanism of a typical lithium - ion cell is illustrated in Figure 2.2, using a $LiMY_n$/graphite cell as an example; where M is a 3-d transition metal such as Co, Fe, Mn, Ni, and Y is N, O, S, F or PO_4. During the charging process, lithium ions (Li^+) de - intercalate from the cathode material, diffuse into the electrolyte, and pass through the nano-pores of the separator to intercalate into the anode material, the graphite.

Simultaneously, electrons flow in the opposite direction through the external circuit to maintain electro-neutrality. During discharging, that is called the spontaneous process, Li⁺ ions move from the anode back to the cathode and consequently anions move in the opposite direction to balance the charge and maintain the electroneutrality [47].
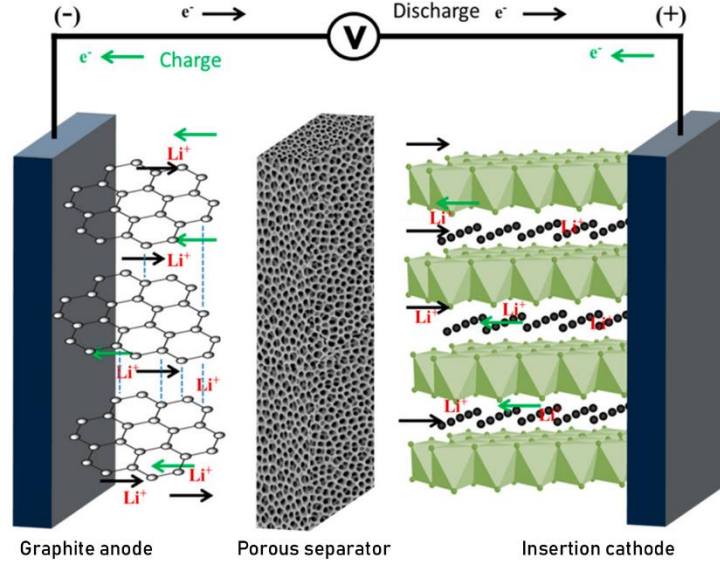
Figure 2.2 Schematic representation of a Li ion cell. During charge process, the cathode is oxidized to produce Li⁺ and electrons (e⁻). The Li⁺ moves across electrolyte and is intercalated into the anode along with the electrons arriving at it through the external circuit. The opposite processes occur during discharge. [56]

The charge and discharge reactions (1-3) are as follows:

Cathode
$$LiMY_n \rightleftarrows Li_{(1-x)}MY_n + xLi^+ + xe^- \tag{1}$$

Anode
$$6C + xLi^+ + xe^- \rightleftarrows Li_xC_{6n} \tag{2}$$

Overall
$$LiMY_n + 6C \rightleftarrows Li_{(1-x)}MY_n + Li_xC_{6n} \tag{3}$$
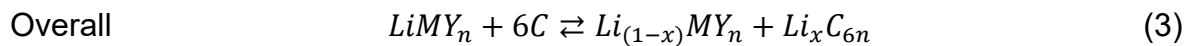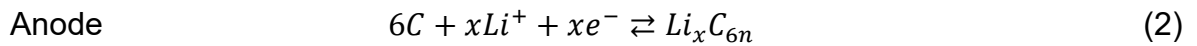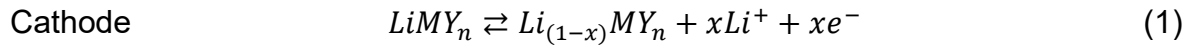
The EESS characteristics of energy and power are intrinsically linked to the fundamental principles of thermodynamics and kinetics, adapted specifically to

electrochemical reactions. The basic thermodynamic equations for a reversible electrochemical transformation are given as (1):

$$\Delta G = \Delta H - T\Delta S \qquad (1)$$

In this context, ΔG represents the Gibbs free energy, which is the energy available from a reaction to perform useful work. ΔH denotes the enthalpy, or the energy released during the reaction, while ΔS represents entropy. T is the absolute temperature, and the term $T\Delta S$ accounts for the heat associated with the organization or disorganization of materials. The variables ΔG, ΔH, and ΔS are state functions, meaning they depend principally on the identity of the materials and the initial and final states of the reaction.

Since ΔG represents the net useful energy available from a given reaction, its electrical equivalent for a reaction in a cell is expressed as:

$$\Delta G = -nFE \qquad (2)$$

Here, n is the number of electrons transferred per mole of reactants, F is the Faraday constant (equal to the charge of one equivalent of electrons), and E is the voltage of the cell associated with the specific chemical reaction. In other words, E represents the electromotive force of the cell reaction.

The cell voltage E is unique for each reaction couple. The total amount of electricity produced, nF, depends on the quantity of reactants available and can be considered a capacity factor. In contrast, the cell voltage can be thought of as an intensity factor. Standard thermodynamic principles regarding the effects of temperature, pressure, and other conditions apply directly to electrochemical reactions. For a process to be spontaneous, the free energy must be negative, and the electromotive force must be positive, when the reaction is written in a reversible manner.

Thermodynamics describes reactions at equilibrium and defines the maximum energy release for a given reaction. Compared to the equilibrium voltage, also known as the open-circuit voltage (V_{OC}), the voltage decreases referred to as "electrode polarization" or "overvoltage" when current is drawn from the battery. This voltage drop occurs due to kinetic limitations of the reactions and other processes that must take place to sustain current flow during operation. Electrochemical reaction kinetics follow the same fundamental principles as bulk chemical reactions. However, electrode kinetics differs in two critical ways. First, the potential drop across the electrical double layer at the electrode/electrolyte interface directly influences the activated complex, impacting the reaction process. Second, unlike bulk chemical reactions, which occur in three dimensions, reactions at electrode interfaces take place in a two-dimensional space.

The mechanism of battery electrode reactions typically involves a sequence of physical, chemical, and electrochemical steps, such as charge-transfer and charge-transport reactions. The overall kinetics of the electrode, and thus the cell or battery, are governed by the rates of these individual steps.

Polarization in an electrochemical cell is influenced by three key kinetic effects. Activation polarization is related to the kinetics of the electrochemical redox or charge-transfer reactions that occur at the electrode/electrolyte interfaces of the anode and cathode. Ohmic polarization arises from the resistance within the cell components and any contact resistance between them. Finally, concentration polarization is a result of mass transport limitations that occur during cell operation. The overall polarization η is described by equation 3:

$$\eta = E_{OCV} - E_T \tag{3}$$

13

where E_{OCV} is the voltage of the cell at open circuitand E_T is the terminal cell voltage with current flowing. The influence of kinetics effect over polarization, are represented in a typical discharge curve, visible in Figure 2.3.
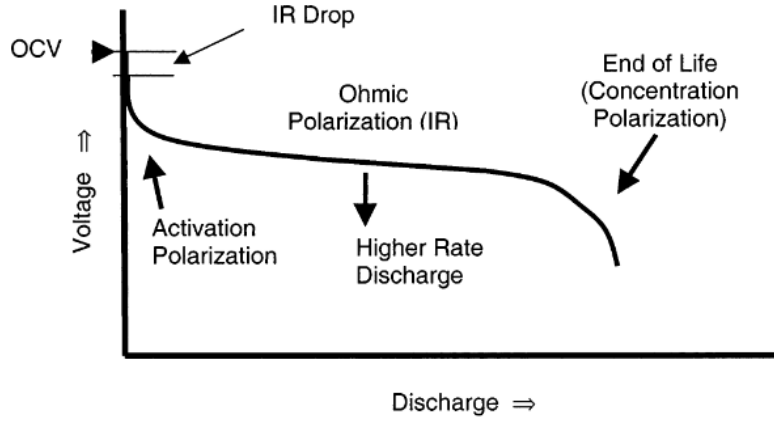
Figure 2.3 Contribution of the overpotential on a potential-current curve.

2.2.1 Significant battery metrics

For battery applications, the amount of charge that the system can provide is crucial. To determine a cell's maximum deliverable charge, it's important to notice that each active material has a theoretical specific capacity, which depends on its molecular weight and the number of electrons involved during the electrochemical reaction. The theoretical capacity, expressed in mAh g^{-1}, can be calculated for each electrode material using the formula (4)

$$Q = \frac{nF}{mw} \tag{4}$$

where mw is the molecular weight of the active material. The experimentally specific capacity is evaluated by integrating over time the measured current normalized by the mass of the electrode material (or the cell, depending on the configuration).

In a well-balanced cell, the anode and cathode capacities should be equal in absolute terms, represented as $C_A m_A = C_C m_C$, where C_C and m_C are the specific capacity and active material mass of the cathode, and C_A and m_A refer to the anode.

[58]In battery science, a handy way to visualize charge and discharge behaviour is through the voltage profile plotted against time. An example of this is shown in Figure 2.4, which illustrates typical voltage profile curves. Discharge capacity is typically specified alongside the current applied, indicated in terms of C-rate, which indicates the amount of time required for completely charging or discharging a cell of a defined capacity.

Figure 2.4 Voltage profile vs specific capacity during a charge-discharge cycle

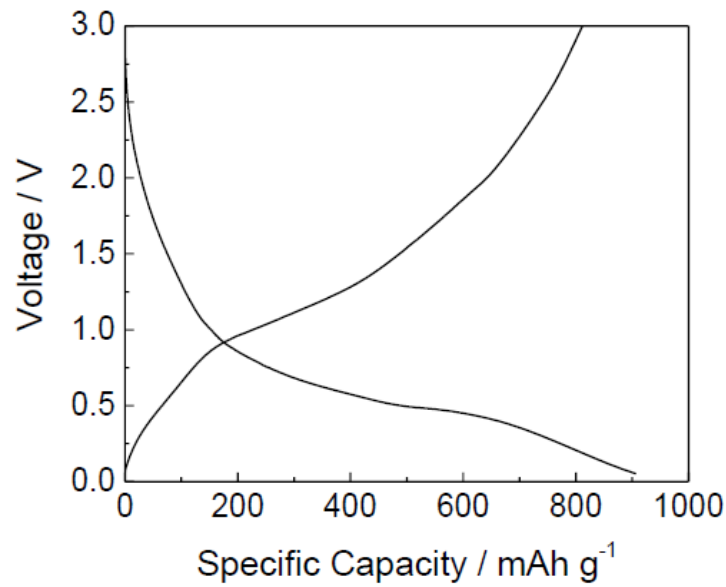The ratio between the total discharged capacity and total charged capacity is named coulombic efficiency ($CE_\%$), and is calculated as follows (5):

$$CE_\% = \frac{Q_{discharge}}{Q_{charge}}\%$$

(5)

$CE_\%$ could also be referred to as single electrode in half-cell setups experiments. In the next sections, the electrode material under studying (Working Electrode, WE) is paired with a non-limiting electrode (Counter Electrode, CE) to evaluate the efficiency of the individual electrochemical process. In addition, energy density (Wh L^{-1}) or specific energy (Wh kg^{-1}) and power density (W kg^{-1}) are commonly used metrics for comparing battery specifications. Energy density is determined by integrating over time the voltage curves obtained at constant current $\int V \, x \, i \, dt$, while power density is calculated as the energy delivered over time (energy t^{-1}).

2.3 Lithium - based batteries

The turning point occurred when Sony introduced the LIBs in 1991; since then, lithium - based batteries achieved the most significant commercial and research interest among all battery technologies, with numerous excellent review articles detailing their advancements and challenges [57,58]. Currently, they dominate nearly two-thirds of the global battery market due to their high energy density, portability, suitable cycle life, and compact dimensions, which offers flexibility in product design particularly for portable electronics and EVs. Furthermore, following the huge demand for LIBs, the prices of batteries have decreased rapidly due to several key factors, including advancements in technology, economies of scale, improvements in the supply chain, and increased competition between producers [59–61].

The energy density of a battery is directly linked to its working voltage $E = Q \, x \, V$, while its power is proportional to the square of its voltage $i \, x \, V = \frac{V^2}{R}$. Consequently, the pursuit of improved systems and materials has often focused on achieving higher voltages.

Lithium-based battery systems are particularly attractive due to lithium's properties: if lithium metal is used as anode electrode, could benefit of the lowest standard reduction potential ($Li^+ + e^- \rightleftharpoons Li$, redox potential = −3.04 V vs. SHE) and lithium is the third lightest element (6.94 g/mol), which results in one of the highest energy densities. Theoretical energy density for lithium-ion batteries is approximately 380 Wh/kg, with commercially available lithium-ion rechargeable batteries offering 150 - 210 Wh/kg. Additionally, lithium ions (Li^+), with a small ionic radius (90 pm), enable fast diffusion through the electrode material, supporting rapid charge and discharge rates [29,62].

2.3.1 Negative electrode materials

Since Sony manufactured LIBs with graphite anodes in 1991, most commercial LIBs keep using graphite anodes. The adoption of layered graphite offers several advantages such as low potential of Li ion intercalation (<0.4 V vs Li), ease and reversibility of Li^+ ions intercalation and low volumetric expansion. Although this widespread diffusion, several alternative anode materials are being developed, especially because of intrinsically technical limitations and sustainability of graphite production [41,60].

These include lithium metal, lithium alloys, and nanostructured host materials such as silicon nanowires. Each of these materials presents its own advantages and challenges in terms of performance and implementation [63].

Particularly, lithium metal is considered the ideal anode material due to its position as the most electropositive element in the periodic table and its exceptionally high specific capacity of 3860 mAh g^{-1} [29]. However, lithium's high reactivity raises significant concerns about the chemical stability of the battery electrolyte, setting increased risks

to safety, reliability, and durability. Exothermic reactions between the lithium anode and the electrolyte can lead to overheating and trigger "thermal runaway." Moreover, during charge-discharge cycling, lithium metal anode surface tends to form dendrites due to non - uniform lithium deposition, often occurring at preferential sites, represented in Figure 2.5. These dendrites can eventually penetrate through electrolyte to the point of piercing the separator, potentially causing electrical short circuits and other serious hazards, including fires and or explosions [49,64–66].
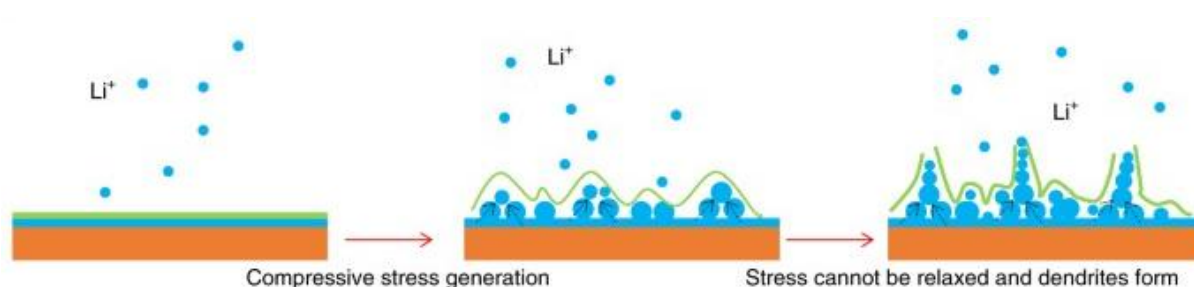
Figure 2.5 Li-plating non homogenous plating upon cycling causes the formation of Li dendrites. Orange, blue, green and represent Cu, Li, and SEI respectively [67]

Indeed, to overcome issues related to dendrite formation while enhancing mechanical durability and extending cycle life, recent attention has shifted toward alternative materials, such as alloying and conversion chemistries, or using additives that could inhibit dendrite formation, or lastly switching from liquid to solid electrolytes that can establish a physical barrier preventing short circuit from dendrites [64–66,68,69].

2.3.2 Positive electrode materials

Although lithium metal-based anodes represent the electrode that operates at more negative potentials, to further increase the energy density of the cell, there has been significant research into cathode materials with high half-cell potentials and high capacities for lithium insertion. As a result, recent developments have increasingly

focused on the positive electrode, which is a key component determining the overall performance of the battery [70–72]. Historically lithium cobalt oxide ($LiCoO_2$, LCO) was the most employed cathode for LIBs until late 2010s, by which cobalt was defined one of the most concerning materials for batteries production, and especially its mining arose major social and environmental issues. As a result, new materials have been developed, such as oxides with a reduced content of cobalt, $LiNi_xMn_yCo_{1-x-y}O_2$ (generally called NMC) or oxides without cobalt content $Li_2Mn_3NiO_8$ (MNO), $LiMn_2O_4$ (LMO), and even phosphates such as $LiFePO_4$ (LFP) and $LiFe_{1-x}Mn_xPO_4$ (LFMP). The crystal structures of the three main classes of Li-insertion materials are shown in Figure 2.6.

layered $LiCoO_2$ spinel $LiMn_2O_4$ olivine $LiFePO_4$
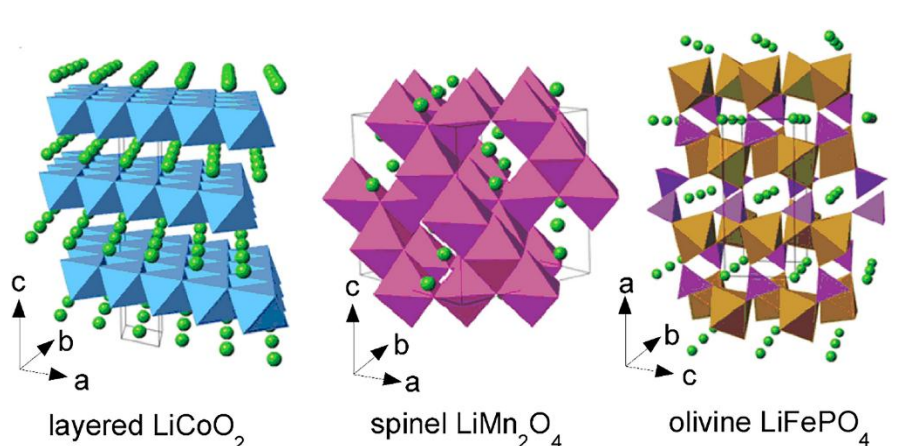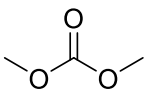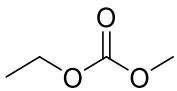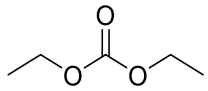
Figure 2.6 Crystal structure of the three lithium-insertion compounds in which the Li^+ ions are mobile through the 2-D (layered), 3-D (spinel) and 1-D (olivine) frameworks [73]

The latter, LFP and LFMP, gained significant interest over last years despite lower voltages of operation and, hence, lower specific energies. Indeed, these materials are extremely robust upon ageing and cycling and more importantly are obtained by abundant materials and easy to recycle [70,74–76].

2.3.3 Electrolytes and porous separator

Alternative approaches dealing with battery safety, sustainability, stability, and dendrite issues in case of LMBs have focused on tailoring the electrolyte and separator or exploring potential improvements and new alternatives, such as switching to solid electrolytes. Both separator and electrolyte in a LIBs plays a critical role in transporting Li$^+$ ions between the positive and negative electrodes [29,77–79]. During operation, electrolyte is in direct contact with the highly reductive anode, the highly oxidative cathode, the separator, and other inactive materials, while also an efficient Li$^+$ ion transport across a broad temperature range is required. Therefore, the electrolyte must meet several key requirements, including high ionic conductivity, a wide electrochemical stability window, and appropriate chemical and thermal stability. The standard electrolytes used in lithium-ion batteries are solutions containing lithium salt, like hexafluorophosphate (LiPF$_6$), Bis(trifluoromethanesulfonyl)imide (LiTFSI) and Bis(fluorosulfonyl)imide (LiFSI); dissolved in an organic solvent, typically carbonates mixtures, e.g. ethylene carbonate, dimethyl carbonate, diethyl carbonate [79], which properties are listed in Table 2.1.

Solvent	Structure	M.W. [g mol^{-1}]	Dielectric constant	Viscosity [cP]	Density [g cm^{-3}]
DMC		90	3.12	0.63	1.063
EMC		104	2.93	0.65	1.007
DEC		118	2.82	0.77	0.969
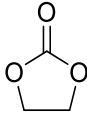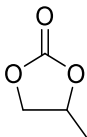
EC		88	90.0	1.9	1.327
PC		102	64.9	2.53	1.201

Table 2.1 Properties of the most used organic carbonates solvents

Liquid electrolytes require a separator to ensure the safety and performance of LIB cells. Currently the most popular membranes employed are typically oil-derived polyolefin with microporous structure, such as polyethylene or polypropylene, in mono or multi - layer forms. These separators often incorporate tailored components or coating, based on end-user needs, as displayed in Figure 2.7, which could improve safety or compatibility with electrodes [77].

Surface functionalization   Morphology design   Multilayer composite

Figure 2.7 Three examples representing modification methods to design functional separators

Finally, the adoption of a solid electrolyte (SE), where the porous separator and liquid electrolyte are replaced with a SE layer that serves as both separator and electrolyte, originated the solid-state battery. This setup offers several advantages over liquid electrolytes, primarily in terms of safety, for the significantly reduced flammability risks, prevent issues like electrolyte leakages and providing increased mechanical resistance towards short circuit, especially towards dendrite formation and, ultimately, could also

21

increase the environmental sustainability of cells depending on the nature of the SE [70,77,80,81].

3 Towards more sustainable LIBs

As already mentioned in previous chapters, to achieve environmental benefits from battery applications, such as emission-free transportation and enhanced efficiency in renewable energy, the battery the battery cradle-to-grave lifecycle

must be made more sustainable. This approach is essential for improving the overall energy balance, reducing the carbon footprint, and enabling advanced, self-sufficient production methods that could meet the expanding demands of the energy storage market [82].

LIBs could achieve greater sustainability through different approaches such as designing sustainable processes and/or implementing less environmental concerning materials by selecting elements that are abundant, with less risks related to shortages of supply. Furthermore, widespread materials reduce reliance on scarce or geopolitically sensitive resources, thus improving supply chain resilience and reducing extraction pressures on limited reserves [83]. LIBs production can also move toward renewable resources, like bio-based polymers or carbon materials derived from agricultural or plant wastes. These options might help in reducing the environmental impact respect to traditional mining and manufacturing processes, ultimately lowering the carbon footprint and contributing to the materials' circular economy.

This approach can facilitate both sustainable production and end-of-life recyclability, aligning LIBs more closely with environmental goals and reducing dependency on non-renewable resources [84–86]. Depending on the different technologies and manufacturers, cathode and anode together make up the largest portion of the total weight in LIBs, comprising around 40%. The current collectors of aluminium and copper come next, making up 15%, followed by the electrolyte at 11%, and finally, the

separator, which accounts for the smallest share at 4%. The case and tab make for the remaining part. It's pretty evident that improvements on electrode materials or processing will have a great impact towards the decarbonization [87].
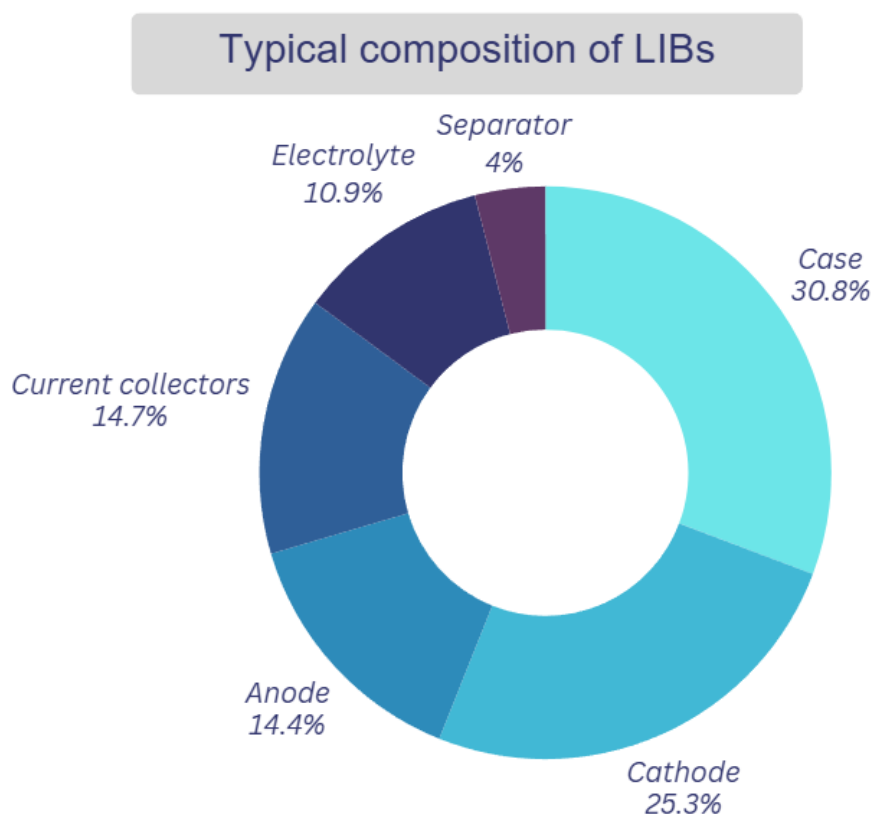
Figure 3.1 Percentage by weight of each component of LIBs

The major target is to evaluate the trade-offs between environmental benefits and practical limitations of the of green alternatives for different parts of an LIB cell and for related technologies and processes.

3.1 Biomaterials for LIBs

In addition to electrode active materials, traditional LIBs include components such as a polymer binder, conductive additive, current collector, and separator. These

components are typically classified as "inactive" materials because they do not directly contribute to the cell's energy storage capacity. However, they serve essential roles in maintaining the structural integrity, stability, and functionality of the battery. The proportion of inactive materials can vary depending on the cell format, the specific active materials used, and the intended application, but they consistently affect the overall energy density, cost, and carbon footprint of the LIB cell [19,86]. Renewable or biobased materials could represent a sustainable alternative to traditional fossil fuel derived materials used in the electrode, electrolyte, and separator components of lithium-based batteries, as displayed in Figure 3.2.

Renewable precursor materials for lithium-ion power sources should meet several key criteria, to enhance sustainability across the battery's lifecycle.

- They should be sourced from abundant biomass that is concentrated and logistically viable, ideally from industrial byproducts.

- They should require minimal physical and chemical processing to reduce resource and energy demands.

- Their performance must match or surpass that of current fossil fuel-based materials to ensure competitiveness.

- They should not contribute to pollution, avoiding harmful waste accumulation or emissions like volatile organic compounds.

- They should be recyclable or reusable after their service life in battery applications.
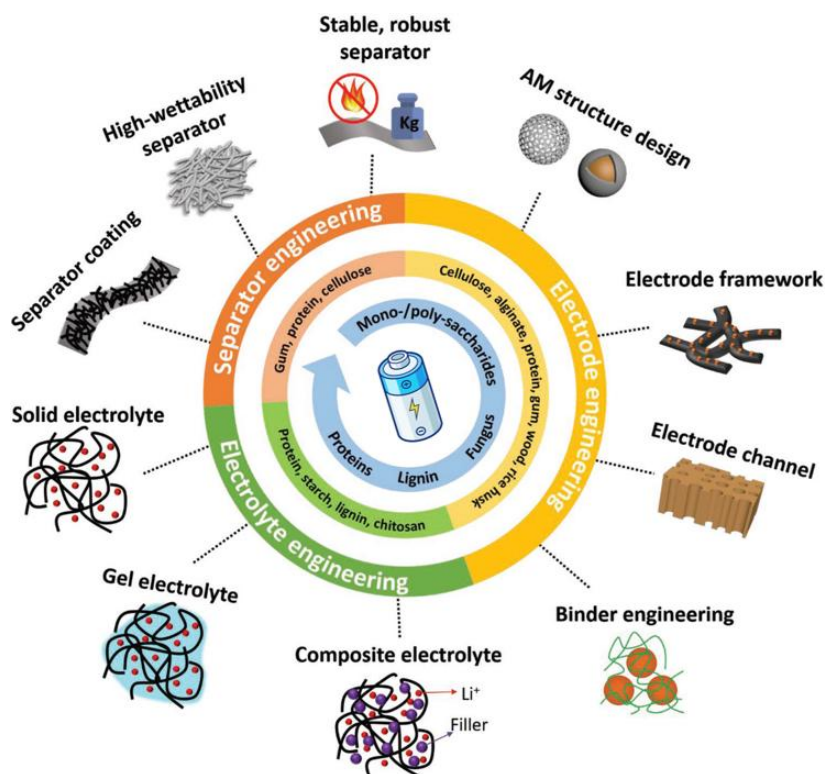
Figure 3.2 Overview of common biomaterials and corresponding strategies for advanced Li-based batteries [88]

Lignocellulosic plant biomass and its primary components cellulose, hemicellulose, and lignin are promising renewable raw materials for battery components. Lignocellulose is readily available from agro-industrial by-products, like cereal straw and corncobs, as well as forestry residues, such as tree bark and sawdust. Additionally, lignin, an aromatic polymer, is available in high purity as a by-product from the production of cellulosic pulp fibres, biofuels, and biochemicals [86,89]. These sources provide a sustainable supply of materials for developing eco-friendly battery components. Along with cellulose and lignin, chitosan and sodium alginate derived from waste biomass, represent the most studied and most widespread biopolymers for lithium ion and lithium metal batteries [86,90].

Cellulose currently represents the most industrially significant renewable polymer in battery electrodes, as evidenced by recent patent applications and an increase in related scientific research. It commonly replaces conventional binders and provides structural support within electrodes [89]. The backbone of unmodified cellulose contains lithophilic polar groups, such as hydroxyl (-OH) and ether (-C-O-C-) groups, which play a critical role in mitigating lithium dendrite formation. Additionally, chemical modifications to cellulose nanocrystals and nanofibrils, introducing sulfate (C-O-SO_3^-) and carboxylic acid (-COOH) groups, hold significant promises as advanced membrane materials for battery applications [85,91]. Chitin and its deacetylated derivative, chitosan, are glucosamine-based polysaccharides that have been employed in creating nitrogen-doped carbon materials for LIB anodes. Chitosan oligosaccharides have demonstrated effectiveness, when used as matrix substrate for lithium deposition, in promoting uniform lithium deposition in lithium metal anodes, leading to enhanced capacities and cycling stability compared to untreated lithium metal anodes when paired with commercial cathode materials [85,92,93]. Additionally, various biomass sources, such as wood, crab shells, and fruit stones, have proven to be excellent materials for producing porous carbon hosts for activated carbon electrodes for EDLCs and sulfur storage in Li-S battery cathodes and as separators in lithium-sulfur batteries [85].

While green sources for high-energy active materials currently might seem limited for industrial applications, options regarding inactive components of LIBs, which doesn't have an active role on the redox process but still play a fundamental role in the proper functioning of the cell, e.g. binder maintaining electrodes integrity or functional separator providing better mechanical resistance or wettability, points at enormous opportunities for more sustainable materials. Natural polymers such as sodium

alginate, chitosan and carboxymethyl cellulose (CMC) coupled with styrene-butadiene rubber (SBR) have been explored as sustainable alternatives to polyvinylidene fluoride (PVDF) as binders in cathodes and anodes in LIBs [85,94]. Unlike PVDF, which is challenging to recycle and requires toxic, high-boiling-point solvents like N-methyl-2-pyrrolidone (NMP), these natural binders offer environmental and functional advantages. Moreover, it appears that conventional PVDF binder struggles to accommodate the significant volume expansion of silicon particles during lithiation, leading to disintegration of the polymer network and mechanical failure of the silicon-based anode. In contrast, the alginate-chitosan binder demonstrates a self-healing capability, effectively restoring the electrode structure post-lithiation. This self-healing effect is attributed to the electrostatic interactions between the carboxylate groups ($-COO^-$) in alginate and the protonated amine groups ($-NH_3^+$) in carboxymethyl chitosan. These interactions enable the polymer scaffold to re-establish its structure after the Si particles undergo volumetric expansion [95], represented in Figure 3.3.
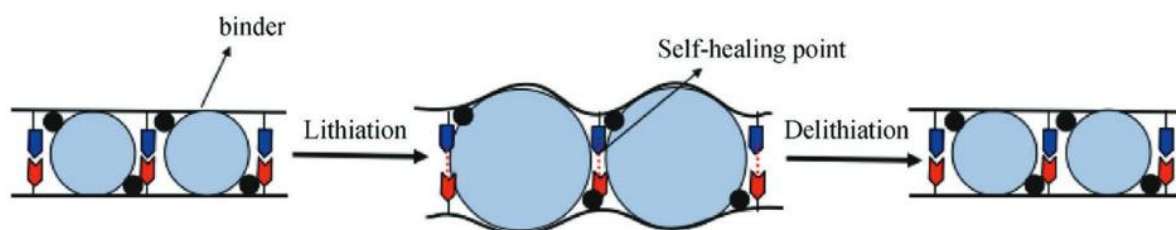
Figure 6 Illustration of the self-healing working principle of binder via electrostatic interactions [95]

A significant step toward more sustainable LIBs electrodes could involve replacing or eliminating metal current collectors. In conventional LIBs, copper foil is used to provide mechanical support and enable current flow in the negative composite electrode, while aluminium foil serves these purposes on the positive side. However, the production of Cu and especially Al is energy-intensive and results in substantial CO_2 emissions.

Additionally, both metals are prone to dissolution under specific operating conditions and chemistries, potentially impacting battery performance and longevity [96]. Freestanding, current-collector-free LIB electrodes offer a promising alternative, potentially contributing significantly to improving the overall energy balance and environmental footprint of LIB cells [97,98].

Finally, conventional liquid electrolytes LIBs necessitate the inclusion of a separator for ensuring both the safety and optimal performance of cells. Currently, commercially available separators are typically microporous mono or multilayer membranes composed of low-cost, oil-derived polyolefins such as PE or PP. These separators, depending on LIB chemistry, comes with tailored number of layers, surface modifications or ceramics coatings to enhance safety by improving thermal and mechanical stability, as well as preventing short circuits from dendritic penetrations in LMB [51,52,99]. Sustainable approaches for LIB separators emphasize the development of polymer matrices derived from biocompatible and eco-friendly materials sourced from renewable resources. Among these, cellulose, the most abundant natural biopolymer, has emerged as a leading candidate for biogenic separator materials [100]. Incorporating cellulose fibres as a primary component in nonwoven composite separators offers several advantages:

- o Enhanced mechanical strength, improving durability and performance under mechanical stress.

- o Improved electrolyte wettability, facilitating better ion transport and cell efficiency.

- Shape retention at elevated temperatures, providing thermal stability and reducing the risk of separator shrinkage or deformation during high-temperature operation.

These properties make cellulose-based separators a promising sustainable alternative to conventional oil-derived polyolefin separators in LIBs [86].

In addition to cellulose, other biopolymers exhibit promising similar properties for use as battery separators [101–103]:

- Chitin, the second most abundant natural polymer, has been used to create nanofiber membranes that outperform polypropylene-based separators in both lithium and sodium metal cells, especially at elevated temperatures [101].

- Silk fibroin, a natural protein, can be processed into membrane films, sponges, and nonwoven membranes through electrospinning. These materials have shown comparable or superior performance as separators in lithium iron phosphate (LiFePO$_4$) cells [103].

- Alginate, a polysaccharide, has demonstrated superior performance as a separator material for high-voltage lithium nickel manganese oxide (LNMO) cells. Its strong polymer backbone, excellent electrochemical stability, and carboxyl groups for effective ion coordination make it an ideal candidate [102].

 Currently, the use of organic solvents and lithium salts with a significant fluorine content is the combination that enables a wide electrochemical stability window. However, the use of fluorinated compounds is becoming increasingly concerning from an environmental perspective and, despite the challenges, developing more sustainable liquid electrolytes appears to be the optimal solution to help reduce the environmental impact [104]. The use of optimized, water-processable biopolymers as

separator and binder materials offers a viable pathway toward more sustainable and environmentally friendly LIB cells, representing a significant step forward in achieving safer and more sustainable battery technologies [105,106].

The next step in achieving more sustainable and safer electrolytes could involve combining the benefits of biogenic polymer matrices with immobilized lithium salts to create PEs[107,108]. A representation of PE is visible in Figure 3.4.
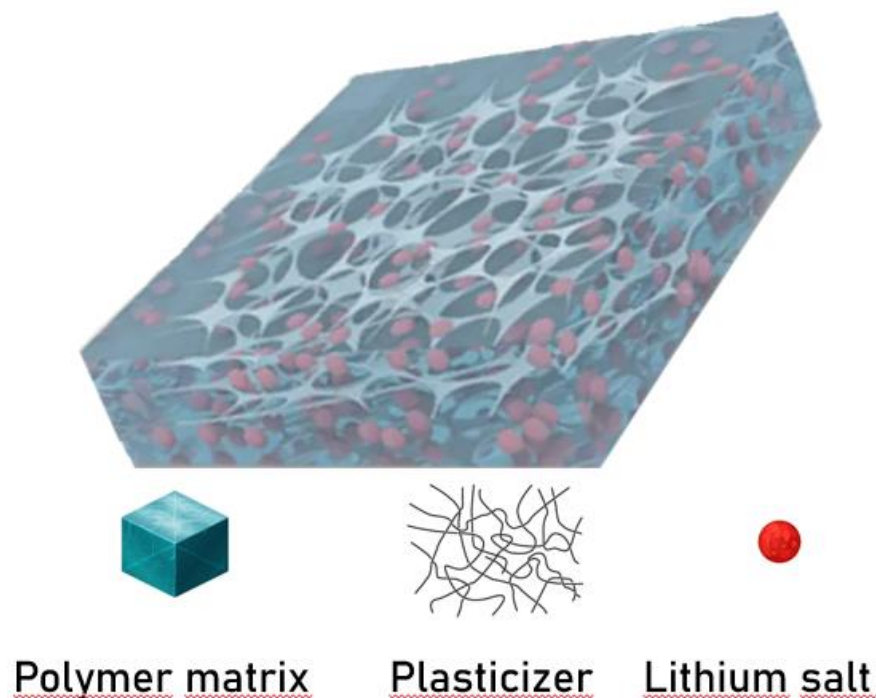
Figure 3.4 Schematic of a gel polymer electrolyte for solid state LIBs

PEs offer several potential advantages over to conventional liquid electrolytes:

- o Enhanced safety: solid polymer electrolytes eliminate the flammability risks associated with liquid electrolytes, improving the overall safety of LIBs.

- o Sustainability: Utilizing biogenic polymers, such as cellulose, chitin, or alginate, as matrices ensures the use of renewable, eco-friendly resources, contributing to reduced environmental impact.

- o Thermal stability: PEs based on biopolymers often exhibit excellent thermal stability, ensuring reliable operation at elevated temperatures.

- o Mechanical strength: biogenic polymers can improve the mechanical support necessary to withstand the stresses of repeated charge-discharge cycles, enhancing battery durability, even if in some cases they are quite brittle.

By leveraging the inherent properties of biogenic polymer matrices and optimizing their interaction with immobilized lithium salts, PEs hold the promise of revolutionizing electrolyte technology, bridging the gap between performance, safety, and sustainability in next-generation batteries [81,107,108].

3.2 Materials processability

Electrode production is heavily influenced by the characteristics of the battery materials employed, and alongside represents a considerable opportunity for further environmental optimization. Electrode processing involves four key steps: i) mixing the electrode slurry or paste, ii) coating, iii) drying, and iv) calendering. While commercial LIB anode preparation has already transitioned to using water-based electrode dispersions, significant ecological challenges persist in cathode production, particularly due to the use of the toxic solvent N-methyl-2-pyrrolidone (NMP) [109]. A visual representation is shown in Figure 3.5.

Solvent	Mixing	Coating	Drying	Recovery
NMP	Hazardous handling requires ventilation system and PSE	Controlled enviroment needed	Solvent vapours need to be collected to avoiding dispersion in the atmosphere	Recovery system required to recycle the expensive solvent
Water	PSE only required for handling of powders	Can be performed in air	No recovery necessary	Not needed

Figure 3.5 Simplified schematic description of electrode manufacturing process. From left to right, the main advantages of water over NMP are highlighted for each step, from the initial mixing of the slurry, its coating on the current collector, the drying of the electrode layer and, finally, the solvent recovery [105]

Shifting from an NMP-based to an aqueous electrode production process offers significant benefits, including drastically reducing energy consumption due to the elimination of the solvent recovery step, lowering costs by over 90% [110]. However, overcoming the challenges associated with aqueous cathode production requires considerable effort. These challenges include side reactions of moisture-sensitive high-energy cathode materials (e.g., Ni-rich materials), such as proton-Li^+ exchange, which leads to delithiation of the active material, and an increase in the dispersion's pH, which can result in the corrosion of the aluminium current collector [109]. However, adjusting the pH value of the slurry by adding amounts of acidic species appeared to be effective towards adverse side reactions [111]. Employing water-based dispersions in the production of composite electrodes also introduces high capillary forces during the drying process. These forces can lead to the formation of cracks in the electrode,

33

particularly as the electrode thickness increases with the aim of achieving cathodes with high amount of active material per area (mass loading) [86]. On the other hand, the challenge of crack formation in thick electrodes due to high capillary forces during drying can be mitigated by incorporating small quantities of isopropyl alcohol into the electrode slurry [112]. An optimized slurry formulation, which includes the selection of an appropriate binder or binder combination, along with rapid processing techniques that minimize water content and reduce the contact time between water and the active materials, is expected to enable the industrial-scale aqueous production of Ni-rich as well as $LiFePO_4$ based cathodes can be produced on a large-scale using water-based preparation methods[109,111]. The latter do not rely on critical metals such as cobalt (Co) or nickel (Ni), making them an environmentally friendly option, particularly in applications where lower energy densities are acceptable [113].

4. Bio-based binder

As discussed in Chapter 3.1, one of the possible strategies to overcome sustainability limits of EESS is to replace conventional binder with polymer that are obtained from renewable sources and are processable in aqueous environment. [114,115].

This Chapter investigates the suitability of chitosan as binder for electrodes operating in different electrolytes, both organic and aqueous. The chemical modification of the binder, the processability in aqueous solutions and the electrochemical performance will be explored in the following section.

The experimental work presented in the following section is focused on the modification of chitosan from water-processable to water-insoluble binder, for use in devices with aqueous electrolytes, and the electrochemical performance will be presented and discussed.

4.1 Binder role for electrodes

Typically, represents together with conductive additive, the inactive components of the electrodes, and accounts only for 3 - 8 wt.% of the electrodes weight depending on the chemistries [116]. Although their quantities within LIBs are relatively low compared to electroactive materials, the significance of these additives is increasingly recognized since they have proven ability to enhance the electrochemical performance of high-capacity electroactive materials, effectively addressing challenges such as stability, conductivity, and interfacial compatibility [117,118].

Among the inactive materials, the polymeric binder - is critical for maintaining the structural integrity of the electrodes. It bonds the electroactive materials with

conductive additives onto the current collector's surface, ensuring mechanical stability and electrical contact, as could be seen in Figure 4.1. This role is particularly crucial during the repeated charge and discharge cycles, where volume changes in the active materials can stress the electrode structure. A reliable binder minimizes material degradation and contributes to the long-term performance and durability of the electrodes [119].
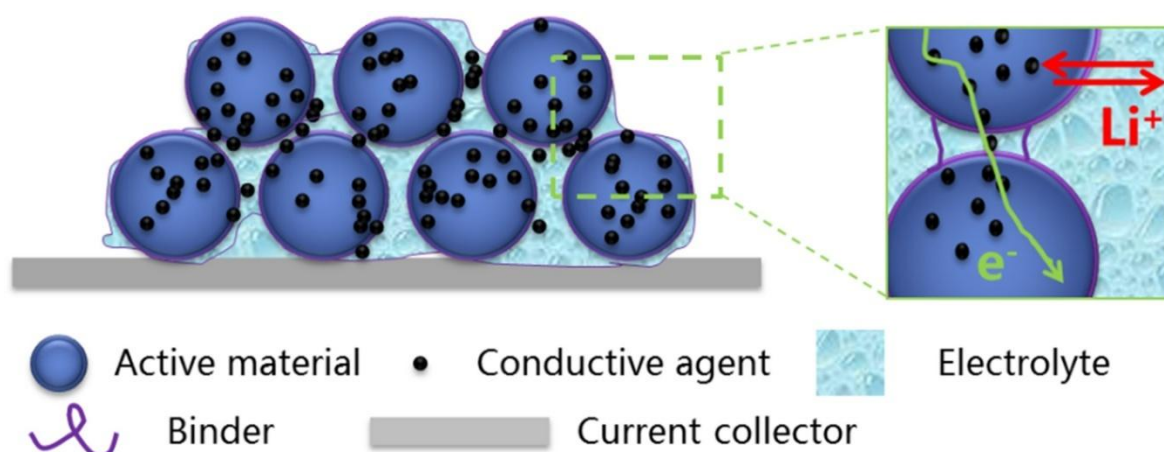
Figure 4.1 Scheme illustrating a typical porous electrode composition, featuring binder, active material and conductive additive particles and the electrolyte (liquid or solid) filling the voids between particles, image courtesy of [120]

The properties of the binder such as the type of polymer, molecular weight, mechanical properties, and the solvent used significantly influence the rheological behaviour of the electrode slurry, which in turn directly influences the electrochemical performance of the battery [121].

The role of the polymer binder in lithium-ion batteries can be understood at both the macroscopic and microscopic levels. At the macroscopic level, the role of the polymer binder is primarily linked to the electrochemical performance of the battery, i.e. electronic conductivity and cycling performance [122].

On the other hand, at the microscopic level, the role of the binder involves several properties such as adhesion, volume expansion, electrolyte interaction and its dispersion and concentration, affects significantly the overall durability and efficiency of the battery [116]. The binder promotes strong adhesion between the active material particles, conductive additives, and the current collector, ensuring consistent electron pathways. During charge/discharge cycles, active materials may expand or contract. The binder helps manage these volume changes, maintaining structural integrity and avoiding particle detachment. The chemical compatibility with the electrolyte is crucial to ensure stability, minimize side reactions, and maintain ionic pathways.

The binder ensures a uniform distribution of active materials and conductive additives within the electrode, which helps optimize electrochemical performance, and provides flexibility and mechanical strength to prevent cracking or delamination under operational stresses. It determines the slurry's rheological properties during electrode manufacturing, influencing coating uniformity and electrode thickness.

Different polymers are used as binder with different electrode materials. Table 4.1 summarizes the most used polymers, the solvent required for the processability and the electrodes with which they are used.

Binder	Solvent	Active material	
		Cathode	Anode
Nafion	NMP	$LiMn_2O_4$	
Poly(acrylic acid) (PAA)	NMP + Water	$LiFePO_4$	Graphite
		$LiCoO_2$	Silicon
		$LiMn_2O_4$	Sulfur
		$LiCoO_2$	
PVdF	NMP	$LiCo_{1/3}Ni_{1/3}Mn_{1/3}O_2$	Silicon
		$LiCo_{0.6}Ni_{0.2}Mn_{0.2}O_2$	Graphite
		$LiCo_{0.8}Ni_{0.1}Mn_{0.1}O_2$	$Li_4Ti_5O_{12}$
		$LiMn_2O_4$	SnO_2
		$LiFePO_4$	Sulfur
		$LiNi_{0.5}Mn_{1.5}O_2$	
Carboxymethyl cellulose (CMC)	Water / Water + iso-propyl alcohol	$LiCo_{1/3}Ni_{1/3}Mn_{1/3}O_2$	
		$LiFePO_4$	
		$LiNi_{0.5}Mn_{1.5}O_2$	
Carboxymethyl cellulose Styrene butadiene block co-polymer (CMC - SBR)	Water / Water + iso-propyl alcohol		Graphite Silicon

Table 4.1 Summary of polymers used as binders for electrodes [116]

As can be seen, most of the binder are processed with NMP, which is a toxic and flammable solvent, and PVdF is the most versatile polymer that found applications for nearly every type of active material thanks to its chemically stability in a lot of solvents and wide electrochemical stability window but is processed with NMP an established toxic and flammable solvent [123].

However, the progressive ban of poly/per-fluorinated alkylated substance (PFAS), raising environmental and human health, which sooner or later will affect also the increasing LIBs market, made the implementation of water processable binder originated from renewable sources more desirable. It would bring benefit to environmental impact and lower production costs related to the manufacture of LIBs, thanks to the lower boiling temperature of water and the absence of condensation system for solvent recovering during processing and drying [115,124].

In recent years there have been significant result by replacing PVdF with the already mentioned CMC and PAA [125,126], and other bio-derived polymer such as chitosan and sodium alginate exhibited promising performance, as part of a possible path towards more sustainable LIBs (Figure 4.2) [127,128].

These improvements might come from functional groups i.e. alcoholic (-OH), carboxylic (-COOR) and aminic ($-NH_2$), grafted or contained in the main backbone. These groups interact with the surface of the active materials, with other polymeric binder chains and even with the current collector, through hydrogen bond or other Van der Waals interaction, in contrast with the low cohesive force arising from the nonreactive functional groups tethered onto the PVdF [129].

Figure 4.2 Criteria for more sustainable approaches in LIBs manufacturing.

Although addition functional groups of biopolymers provide more cohesive forces between adjacent chains, in the case of linear structure polymers the interactions might not be sufficient to maintain structural integrity of electrode expansion and contraction following lithiation and delithiation processes. These moieties, however, offer the opportunity to easily bind polymeric chains through covalent bonds, in order to improve the mechanical resistance or flexibility, depending on the nature of the crosslinked polymer [130].

4.2 Aqueous electrochemical energy storage systems

Although water processable bio-based binder proven already their capabilities to enhance the overall sustainability of electrode manufacturing process, their application in batteries that make use of aqueous electrolytes could not be viable due to the progressive dissolution in the medium.

Water has historically been relevant to the development of electrochemistry and batteries due to its availability, safety, and excellent ionic conductivity when coupled with appropriate salts. However, water's thermodynamic characteristics significantly

limit its application due to its narrow electrochemical stability window (ESW). Water ESW is defined by its decomposition reactions: the anodic process of oxygen evolution and the cathodic process of hydrogen evolution. These processes define the voltage range within which water is thermodynamically stable, with a span of 1.23 V under standard conditions and remains unaffected with respect to pH [131]. However, the stability window of water can be extended beyond the theoretical 1.23 V by considering kinetic effects and electrolyte modifications, particularly with the use of high salt concentrations [132]. Nevertheless, even if the battery market is dominated by organic electrolytes-based LIBs, aqueous electrolytes offer several advantages, such as providing higher ionic conductivity as well as enhancing safety and environmental benigness [133].

Aqueous electrolytes eliminate the fire hazards associated with organic solvents, preventing thermal runaway, making them safer for large-scale energy storage. Nonetheless, they are significantly abundant and cheaper than organic solvents and there's no need for the strict moisture-free conditions required for organic electrolyte handling, as well as less environmental harmful disposal processes. Moreover, water has a higher dielectric constant, facilitating faster ion transport and resulting in higher ionic conductivity, enabling rapid charge/discharge cycles

Where high energy densities and reduced dimensions doesn't represent a priority, aqueous EESS could represent a viable environmentally friendly option for energy storage [133]. The implementation of the above-mentioned biobased, water-soluble binders could also represent a major progress in the effort to a complete sustainability of aqueous batteries and supercapacitors.

4.3   Aqueous electrochemical supercapacitors

As mentioned in Chapter 1.3, EDLCs represent another class of EESS, their development and application to support the current energetic transition is complementary to batteries [134]. Where batteries provide and store significant amount of charge albeit without the ability to withstand very fast charge and discharge times, EDLCs could deliver the stored charge on much shorter time scales (10^0 - 10^2 s) [135,136]. Moreover, the high-power density and rapid charge-discharge cycles of supercapacitors make them ideal for applications requiring quick and robust power output, such as computer chips, precision machinery, and portable electronic devices. However, their limited energy density restricts their use in energy backup applications. To address this limitation, supercapacitors are often paired with batteries or fuel cells, serving as temporary energy storage devices. In such hybrid systems, they efficiently provide high power output [136].

Storing charge mechanism in EDLCs occurring through a simple electric double layer formation arising from electrostatic attraction between electrolyte and electrode surface involving ion accumulation and adsorption, without any redox process taking part [136]. This property grants EDLCs exceptional stability, leading to a significantly longer life cycle compared to traditional batteries. The performance of EDLCs is affected by factors such as electrode surface area, ionic conductivity, ion size, and electrolyte viscosity [137].

Commonly utilized electrode materials in supercapacitors include activated carbon (AC), graphene, carbon nanotubes, conducting polymers, and transition metal oxides. These materials are selected based on their ability to provide high surface area, excellent electrical conductivity, and favourable electrochemical properties to enhance

energy and power density [138]. Specifically, activated carbon materials are used in EDLCs due to their high specific surface area, excellent electronic conductivity, outstanding chemical stability, ease of processing, cheapness and availability from biogenic sources. Conventional AC, with a theoretical capacitance range of 100-300 F g^{-1}, depending on the electrolyte, demonstrates excellent cycling stability [139–142].

Electrolytes play a critical role in determining the performance of supercapacitors, significantly affecting their overall efficiency and functionality. They influence key parameters such as energy density, power density, and operating voltage window, thereby contributing substantially to the device's performance and durability [143]. The choice of electrolyte, in conjunction with electrodes optimized for pore size, plays a crucial role in determining the equivalent series resistance (ESR) of supercapacitors, which directly affects their power density. Electrolytes characterized by high ionic conductivity are preferred for high-power-density applications. Moreover, the ionic size of the electrolyte is directly linked to capacitance [144]. Decreasing the size of electrolyte ions enhances their diffusion into the electrode pores and facilitates adsorption onto the electrode surface, which boosts the supercapacitor's overall performance. Consequently, both pore size and ionic radius are critical factors for improving charge storage performance. An overview of factors that influence the properties of electrolytes in supercapacitors are shown in Figure 4.3.
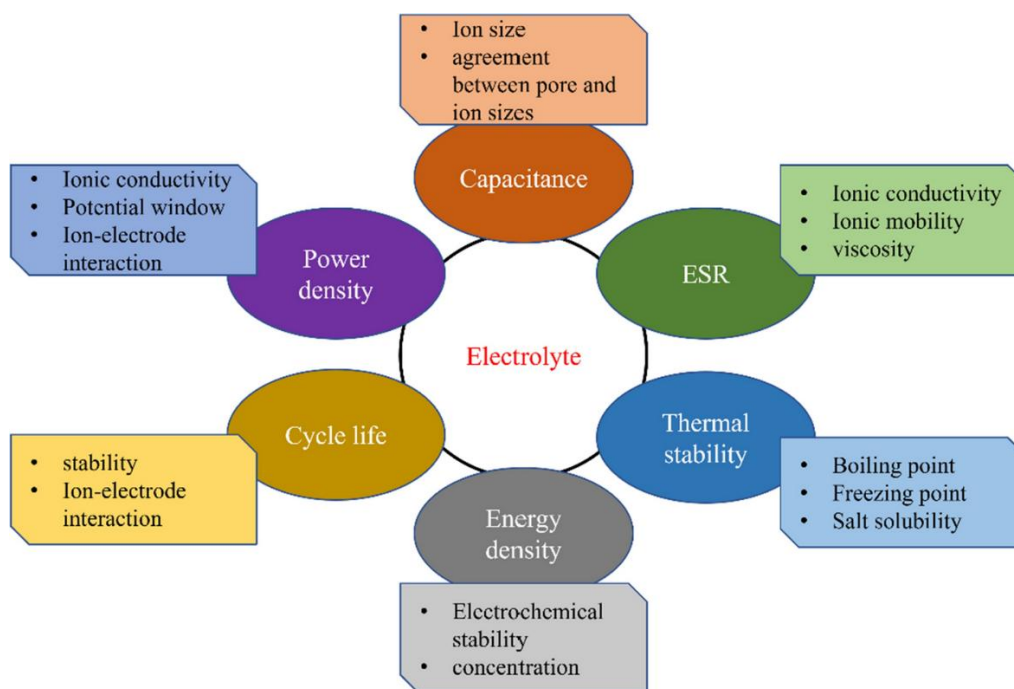
Figure 4.3 Factors affecting electrolyte properties [143]

Electrolytes used in supercapacitors are broadly classified into aqueous and organic types, each with distinct advantages and limitations. Aqueous electrolytes generally restrict cell voltage to about 1 V, due to water decomposition at 1.23 V. In contrast, organic electrolytes enable higher voltages, often exceeding 2.7 V [145]. However, organic electrolytes exhibit significantly higher specific resistance typically 20 to 50 times that of aqueous electrolytes—resulting in reduced power capability [146], and are more expensive. The conductivity of aqueous electrolytes, approximately 1 S cm^{-1}, is notably superior to that of organic counterparts [147]. Moreover, aqueous electrolytes generally outperform non-aqueous ones in conductivity due to their lower viscosity. Electrolytes can be ranked by their conductivity in the following order: H_2SO_4 > KOH > KCl > Na_2SO_4. The ionic size also significantly affects conductivity [143]. Although H_2SO_4 and KOH are widely employed as aqueous electrolytes in supercapacitor applications due to their superior ionic conductivity, their corrosive nature limits their cyclic stability

and makes them unsuitable for applications requiring higher operating voltages. On the other hand, neutral electrolytes exhibit a larger overpotential for hydrogen and oxygen evolution reactions and this characteristic provides a broader electrochemical stability potential window, enhancing their suitability for certain applications, in addition to a high conductivity and low viscosity [143,148]. Among neutral electrolytes, sodium sulfate (Na_2SO_4) is extensively used in aqueous supercapacitors due to its stability and compatibility with various electrode materials [145].

4.4 Modified chitosan as binder for aqueous electrochemical energy storage systems

As mentioned in Chapter 3.1 chitosan, reported in Figure 4.4, is a linear polysaccharide composed of randomly distributed β-(1 → 4)-linked D-glucosamine (deacetylated unit) and N-acetyl-D-glucosamine (acetylated unit). It is obtained from alkali deacetylation of chitin extracted from crustacean shells and some fungi and is already used in non-aqueous LIBs [149].
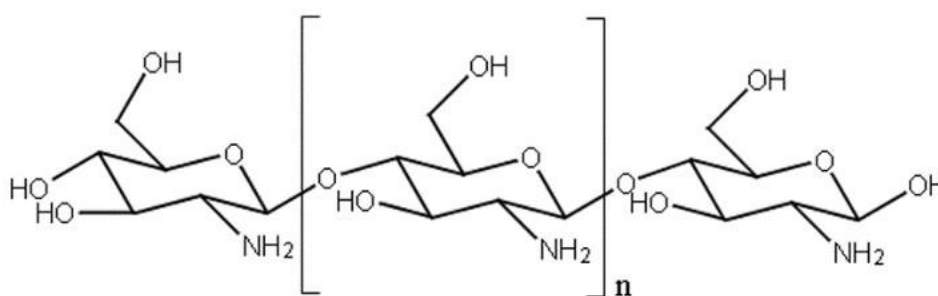

Figure 4.4 Chemical structure of chitosan

45

However, since it became soluble in aqueous acidic environments (pH <6.5), its use in aqueous systems have been limited only to Zn batteries. Chitosan features aminic (-NH$_2$) and alcoholic (-OH) groups grafted on the main polymer backbone. These groups might be used as coupling points for functionalization and crosslinking reactions, customizing the properties of binder according to the required application.

In this section, water-processable chitosan has been transformed in water-unsoluble binder by crosslinking, and the electrodeperformance in different aqueous electrolytes has been investigated. The physico-chemical characterization was performed through infrared spectroscopy (FT-IR), thermogravimetric analysis (TGA), scanning electron microscopy (SEM) and surface area measurement (BET, BJH and DFT models). Electrochemical behaviour of electrodes containing crosslinked chitosan were evaluated through cyclic voltammetries (CV), potentiostatic electrochemical impedance spectroscopy (PEIS) and galvanostatic charge and discharge cycles (GCD).

Chitosan (Sigma Aldrich, from shrimp shells practical grade, ≥ 75% deacetylated), acetic acid (Carlo Erba, RPE ≥ 99.5%), maleic anhydride (MA, Carlo Erba, RPE ≥ 98.5%), succinic acid (SA, 99.5 %, Sigma Aldrich), *N*-(3-Dimethylaminopropyl)-*N'*-ethylcarbodiimide hydrochloride (EDC, 98%, Sigma Aldrich), polyvinylidene fluoride (PVdF, Kynar, Arkema), polytetrafluoroethylene (PTFE, aqueous suspension, Dupont, 60 wt. %), Carbon black C-45 (CB, Imerys Graphite & Carbon), Picactif BP10 (PICA Co.), N-methyl pyrrolidone (NMP, Fluka, ≥99%), ethanol (Sigma Aldrich, absolute, ≥99.8 %) were used without further purification.

Potassium hydroxide (KOH, reagent grade, 90%, Sigma Aldrich), sodium sulphate decahydrate (Na$_2$SO$_4$ · 10H$_2$O, reagent grade, ≥99.0% Fluka), were the salts used for preparing the aqueous electrolytes, without any pretreatment and using MilliQ water.

4.5 Electrodes preparation with modified chitosan binder

Modified chitosan membranes were obtained by adding 54 mg chitosan powder in an appropriate amount of aqueous solution of acetic acid 1 vol.% and left under stirring for one hour at room temperature, until complete dissolution. Maleic anhydride was added to the viscous chitosan solution, in 1:2 molar ratio respect to chitosan, and left under stirring for 16 hours. The solution with modified chitosan was cast on a Teflon mould and left overnight at RT to allow solvent evaporation. The obtained film (38 μm thickness) has been rinsed with acetone and water to remove unreacted MA and acetic acid, respectively. A final drying of 12 hours at 80°C in oven was performed before thermogravimetric analysis (Q50 TA Instrument), where Argon was used as sample gas (60 mL/min) and balance gas (40 mL/min). Bruker Alpha spectrometer was used for Fourier transform infrared spectroscopy-attenuated total reflection (FTIR - ATR). SEM images were collected by a ZEISS EVO 50 instrument.

Activated carbon (AC) electrodes preparation with MA modified chitosan was performed as described in Figure .5, by mixing in a slurry suspension 80 wt.% activated carbon (Picactif BP10) 10 wt.% carbon black (CB) and 10 wt.% chitosan. Chitosan and MA (5.2 :1 w/w), have been poured in an aqueous solution containing 1 vol.% acetic acid and kept under stirring. After complete dissolution of the binder, active material and conductive additive were added and left under stirring overnight to homogenize the solid suspension. The slurry was roll-coated on a mylar sheet and dried at RT overnight. The electrode layer was detached from mylar substrate, and self-standing

electrodes have been punched (0.636 cm^2) and heat treated for 65°C for 12 hours under vacuum. The obtained electrodes (AC MA) had a thickness of 42 µm and a mass loading in the range of 2.5-3.0 mg cm^{-2}.
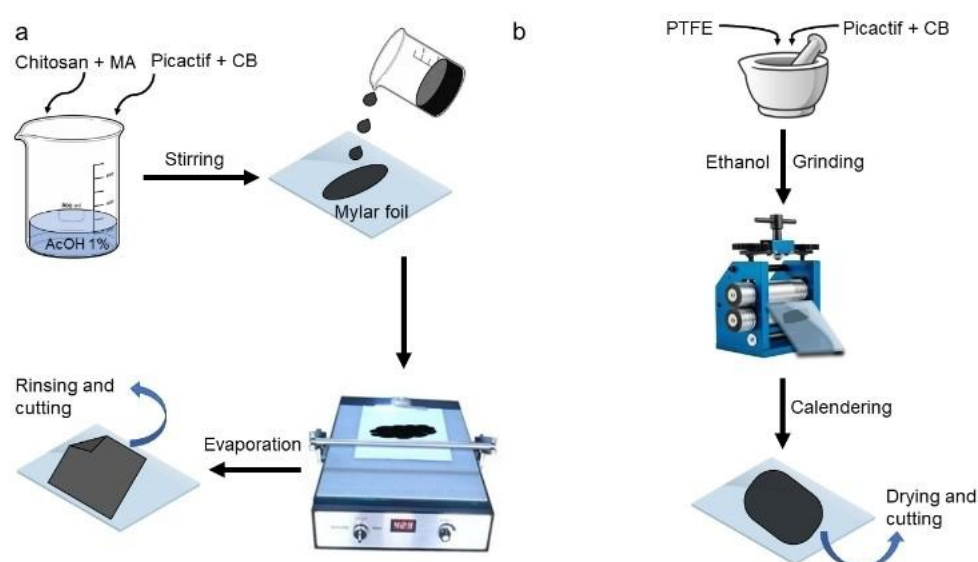
Figure 4.5 (a) Preparation of self-standing AC electrodes with modified chitosan, pure chitosan and PVdF binder and (b) preparation of self-standing AC electrodes with PTFE binder.

Electrodes with PVdF were prepared in NMP by mixing 80 wt.% AC, 10 wt.% CB, and 10 wt.% PVdF. For the electrode preparation, the same procedure described for electrodes with chitosan has been used, by substituting water with NMP, and the electrode layer was dried at RT for 72 h. The electrodes (AC PVdF) had a thickness of 54 µm and a mass loading of 3.6-3.9 mg cm^{-2}.

AC electrodes with PTFE were obtained by mixing in a mortar 90 wt.% of AC, 5 wt.% CB and 5 wt.% of PTFE aqueous suspension, and adding stepwise 350 µL of ethanol, until a uniform paste was formed. Electrode foil was laminated between mylar foils until a uniform thickness of 120 µm was obtained. Self-standing electrodes have been punched (0.785 cm^2) and dried at 120 °C under vacuum for 12 hours. These electrodes

(AC PTFE) had a mass loading of 11 mg cm^{-2} and therefore were used as non-limiting counter electrodes to perform CVs.

Crosslinked chitosan with succinic acid (SA) and *N*-(3-Dimethylaminopropyl)-*N'*-ethylcarbodiimide hydrochloride (EDC) electrodes has been prepared following the procedure as described in Figure 4.6. Crosslinked chitosan chains with succinic acid and EDC as a coupling agent has been the initial idea to ensure a water insoluble electrode with chitosan as a binder, that was developed just before the beginning of the doctoral program, and used as benchmark to compare the improvements with the modification with MA [150] AC electrodes were prepared by mixing 85 wt.% AC, 10 wt.% CB, and 5 wt.% of chitosan. SA and chitosan (1:5 w/w) have been dissolved under stirring in water. After the complete dissolution of the binder, active material and CB additive were added and left overnight under stirring. EDC was added and the solution was left under stirring for 12 h to allow crosslinking. The slurry was roll coated onto a mylar sheet. After drying at RT, the electrode sheet has been detached from the mylar layer, and self-standing electrodes (AC EDC) have been cut and heat treated at 120 °C for 12 h. The obtained electrodes had a mass loading in the range of 4.6 and 5.0 mg cm^{-2}.
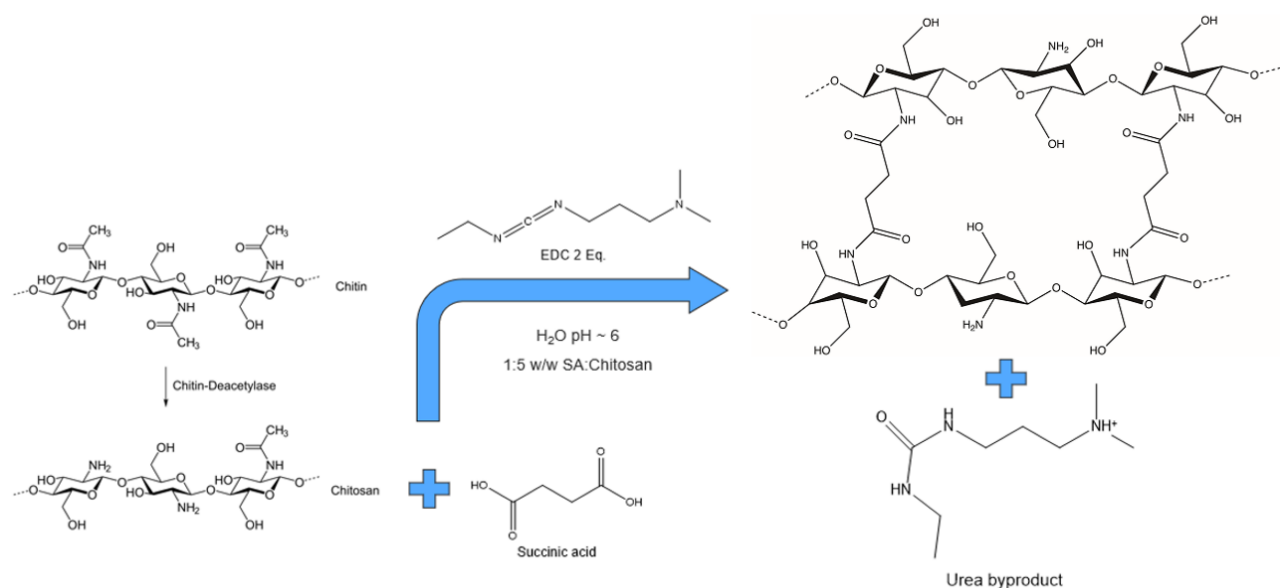
Figure 4.6 Preparation of self-standing AC electrodes featuring crosslinked chitosan with succinic acid and EDC as coupling agent [150]

Nitrogen adsorption isotherms at 77 K of the AC powder and of the electrodes prepared with chitosan and MA-modified chitosan as binders were collected using a Micromeritic ASAP 2020 porosimeter. The samples were dried for at least 24 h at 120 °C before testing. The electrode with chitosan were prepared with the same procedure described in the experimental part without adding the MA. For electrode recycling, Elmasonic S 15 H sonicator and REMI R-8D centrifuge was used. The electrochemical testing of self-standing AC electrodes was performed by using a potentiostat/galvanostat Biologic VSP.

PEIS experiments have been acquired in frequency range 100 kHz - 100 mHz, with a perturbation of amplitude 10 mV around OCV, recording 20 points per decade. The PEIS have been fit using equivalent circuits composed of resistors (R) and constant phase elements (Q). Instead of an ideal capacitor, the Q is used to account for nonideal capacitive behaviours originating from the rough and imperfect surface. The

impedance of the constant phase element is $Z_{CPE} = 1/[Q(i\omega)^\alpha]$ with Q expressed in F · $s^{-(1-\alpha)}$ (or $\Omega^{-1} s^\alpha$) and angular velocity $\omega = 2\pi v$. From the fitting results, the capacitance can be obtained as $C = (Q R^{1-\alpha})^{1/\alpha}$. Each process has its characteristic time constant τ = RC and, it appears in the impedance spectrum at a relative frequency of $v = 1/(2\pi\tau)$.

Impedance spectra were fitted by Boukamp's EqC software. T-shaped PTFE Bola cells (Bohlender GmbH) were used, using working and counter electrodes with an area of 0.636 cm^2, and a silver disk was used as a pseudo reference electrode. All the potentials were calculated vs. saturated calomel electrode (SCE).

CVs to verify the electrochemical stability window, have been performed after 4 hours of OCV to let the system equilibrates and the electrolytes permeate the electrodes, with a scanning rate of 20 mV s^{-1}, for 25 consecutive cycles in three electrodes mode, using a AC PTFE as counter electrode and Ag as reference electrode.

GCD cycles were carried, in three electrodes mode, with the working and counter electrodes made of AC with crosslinked chitosan and modified chitosan electrodes, AC EDC and AC MA respectively, applying 50 cycles at increasing current densities of 0.5, 1, 2 and 5 A g^{-1} respectively, to verify the response of the electrodes at different current densities. To observe the stability of AC chitosan electrodes, were performed 5000 cycles at 0.5 A g^{-1} with the same electrochemical setup.

4.5.1 Chitosan crosslinking

Chitosan exhibits poor solubility in water and in most organic solvents because of strong intermolecular and intramolecular hydrogen bonding interactions [17]. Chitosan is soluble at pH values < 6.5 due to the protonation of the -NH_2 groups of the

51

glucosamine units. For this reason, aqueous solutions of carboxylic acids dissolve chitosan more effectively [17, 18]. SA and chitosan powders were added in water, in 1:5 w/w, and left under stirring for a couple of hours at room temperature until complete dissolution. The solution appeared like a gelatine. For crosslinking the chitosan chains, 2 equivalents of EDC for 1 equivalent of succinic acid were added to the solution. At least two equivalents of a crosslinking agent are required to form chemical bonds between all the amino groups, in chitosan chain, and the two carboxylic terminations of succinic acid, according to the stoichiometry in Figure 5.

Chitosan crosslinked with SA and EDC as coupling agent proved to be a water-resistant binder for different electrode materials operating in aqueous electrolytes [150]. EDC is generally used, in biochemistry, to form amide bonds for the immobilization of large biomolecules. However, it is not a very health - friendly molecule, and for this reason a new crosslinking with SA was studied. Acetic acid was chosen as a viable proton donor able to dissolve chitosan but not able to form crosslinking between different polymer chain, as it was the case of SA. MA was selected as acetylating agent. The addition of MA to dissolved chitosan, led to a modification of the amino groups of chitosan to amides. According to the proposed reaction in Figure 4.7, following ring opening of MA, the lone pair at the nitrogen atom of amines in chitosan chain interacts with the carbonyl of MA leading to the formation of amide. MA can also react with - CH_2OH group with the release of a water molecule.
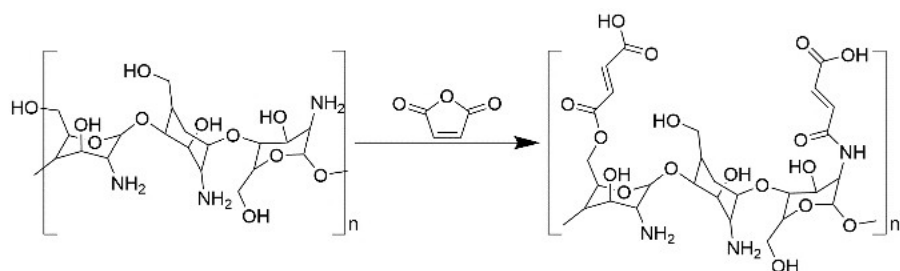
Figure 4.7 Scheme of chitosan modification with maleic anhydride

The obtained polymer results insoluble in water because of the increased amount of less polar moieties in the main chain, and electrodes prepared with this modified binder show high stability in water, as visible in Figure 4.8.
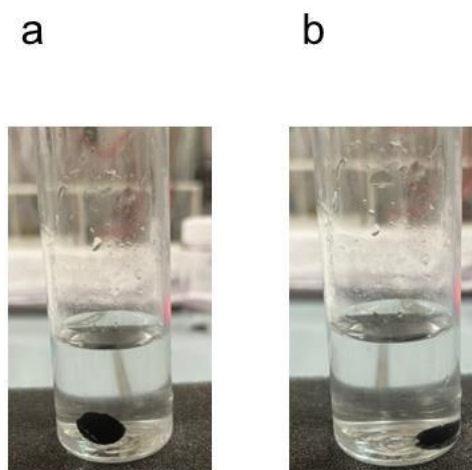
Figure 4.8 Solubility test: electrode with chitosan modified with maleic anhydride as binder (a) just immersed in water and (b) after one month of immersion in water

4.6 *Characterization of electrodes with modified chitosan binder*

In Figure 4.9 is represented the Fourier transform infrared spectroscopy-attenuated total reflection (FTIR-ATR) spectra of films of pure chitosan and of chitosan upon

reaction with MA (modified chitosan). There are no significant differences in the two spectra but in the region around 3400 cm^{-1}, corresponding to primary amine and alcohol stretching signals, which are nearly absent in the modified chitosan. Absorption in 1653 cm^{-1} and 1545 cm^{-1} are compatible with asymmetric N-H bending of amines and asymmetric stretching in amides respectively. The peaks around 1030 cm^{-1} corresponds to C=O stretching in acetamide. The other signals observed in the modified chitosan spectrum were similar to those of the native chitosan, especially looking at the intensity of the signals around 2800 cm^{-1} corresponding to aliphatic C-H stretching, demonstrating that modification with MA does not affect the polymer backbone.
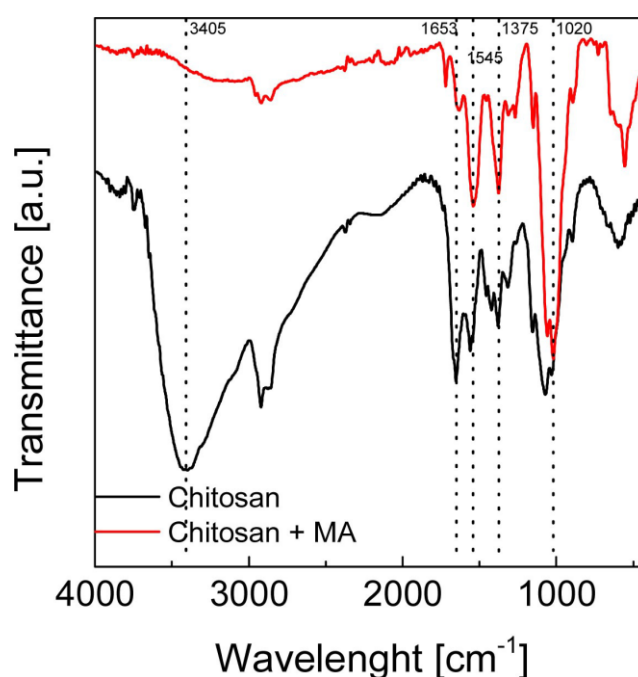
Figure 4.9 FTIR-ATR spectra of chitosan and modified chitosan with maleic anhydride, with 64 scans performed from 4000 to 400 cm^{-1}

Thermogravimetric analysis (TGA) curves for the chitosan and modified chitosan are reported in Figure 4.10. Although both samples were dried, modified chitosan

demonstrated a lower amount or residual water, as it could be seen from the lower mass decrease below 150°C. Compared to chitosan, the degradation of the modified polymer occurs in a wide interval of temperatures. The addition of MA causes a shift on the beginning of thermal degradation at lower temperatures, around 160°C, due to decomposition of high volatile fractions originated by side chains. The latter are primary degradation sites upon the polymer backbone. However, the degradation profile appears less steep compared to that of chitosan, because of the longer side chain formed after MA addition.
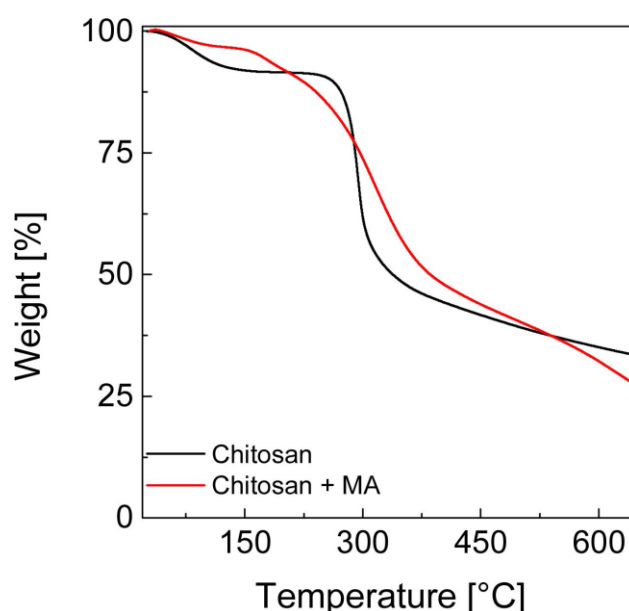
Figure 4.10 TGA curves of chitosan and modified chitosan with maleic anhydride, performed in Ar atmosphere, 10 °C min⁻¹ ramp up to 650 °C

The morphology of the free-standing AC MA electrodes, prepared as described in the experimental section, was evaluated through scanning electron microscopy (SEM). The images, reported in Figure 4.11, don't show any evident inhomogeneity or cracks.
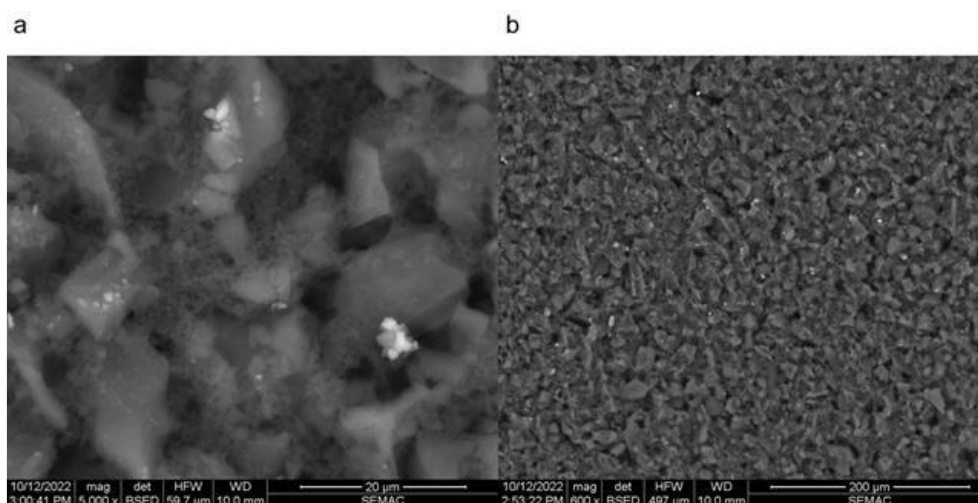
Figure 4.11 SEM images of AC MA electrodes at different magnifications

Porosimetric analysis of the carbon powder and of electrodes made with pure chitosan and AC MA electrodes, was carried out to compare the amount of the surface area blocked by the two binders. The isotherms of the three samples, shown in Figure 4.12a, evidence a high microporous contribution as well as a mesoporous one. Table 4.2 reports the surface area of AC powder and electrodes with different binders, estimated by BET, BJH and DFT models. The BET surface area is quite high for all samples, with an obvious decrease in passing from the powder to the electrodes. However, the BET area takes also into account micropores that could be less involved in the electrochemical process occurring at the electrode. BJH surface area, reported in Figure 4.12b, evaluated in the range of pore size from 1 to 400 nm, displays lower values, and even lower values resulted from DFT analysis in the range 1.5-234 nm. Surface area of electrodes with chitosan and MA-modified chitosan are not significantly different, and ca. 30% lower than that of AC powder.

a

b
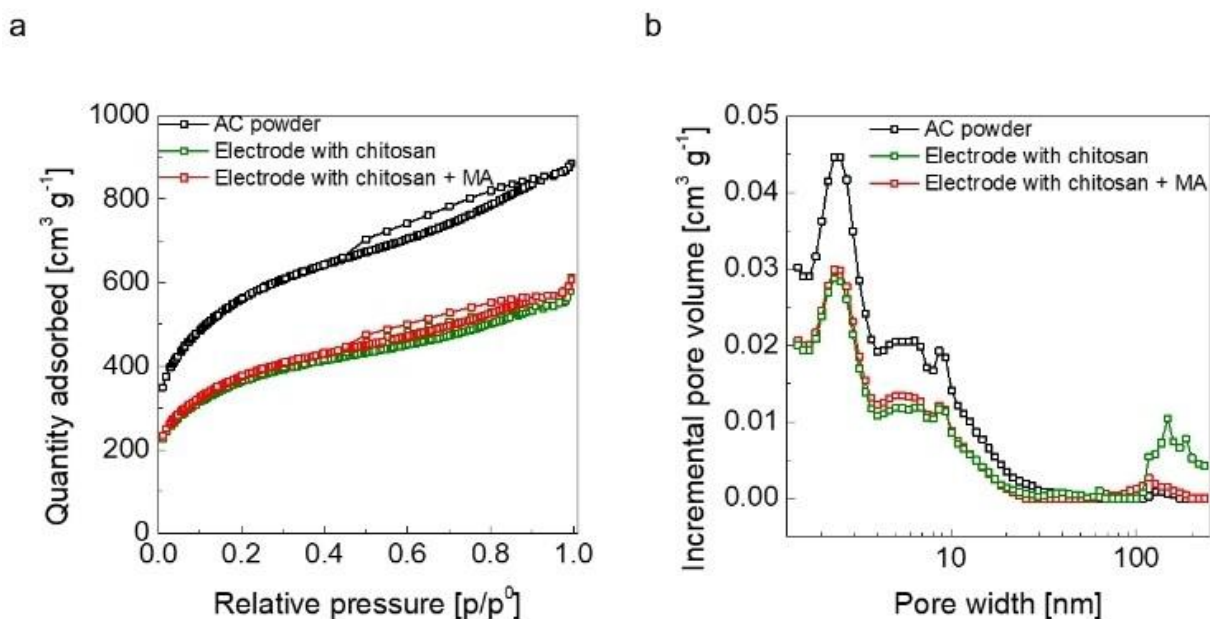
Figure 4.12 (a) Nitrogen adsorption-desorption isotherms of AC powder, electrode with chitosan binder, and electrode with MA-modified chitosan; (b) incremental pore volume vs. pore diameter size of AC powder, electrode with chitosan binder, and electrode with MA-modified chitosan binder

Surface area [m^2 g^{-1}]	AC powder	Electrode with chitosan	Electrode with chitosan + MA
BET	1972	1277	1316
BJT	920	579	619
DFT	510	330	350

Table 4.2 Surface area of AC powder and AC electrodes with different binders, estimated by BET, BJH and DFT models.

The electrochemical tests were performed in Na$_2$SO$_4$ 1.5 M aqueous solutions and, for comparison, in KOH 6 M, a typical aqueous electrolyte used in electrochemical double layer capacitors (EDLCs). The working and counter electrodes for impedance and galvanostatic charge and discharge measurements was AC MA and silver disk as reference, whereas in cyclic voltammetry tests AC PTFE were employed, to use a non-

limiting counter electrode to record only the contribution from the working electrode. Only for the ESW measurement, the used working electrode was stainless steel.

The CVs of these electrodes, reported in Figure 4.13, display a typical capacitive behaviour, with well-defined box shaped cycles. Electrode materials demonstrated stable cycles in Na_2SO_4 electrolyte in the range - 0.9 V to 0.7 V vs SCE (1.6 V), which is a good result for conventional aqueous electrolytes [151–153]. For comparison, the electrochemical window of KOH electrolyte was narrower, ca 1.0 V. In the CVs performed in Na_2SO_4, it is also visible a broad oxidation peaks around 0.21 V and reduction peaks 0.15 V are perceptible, indicating the occurrence of a faradaic reaction.

a

b
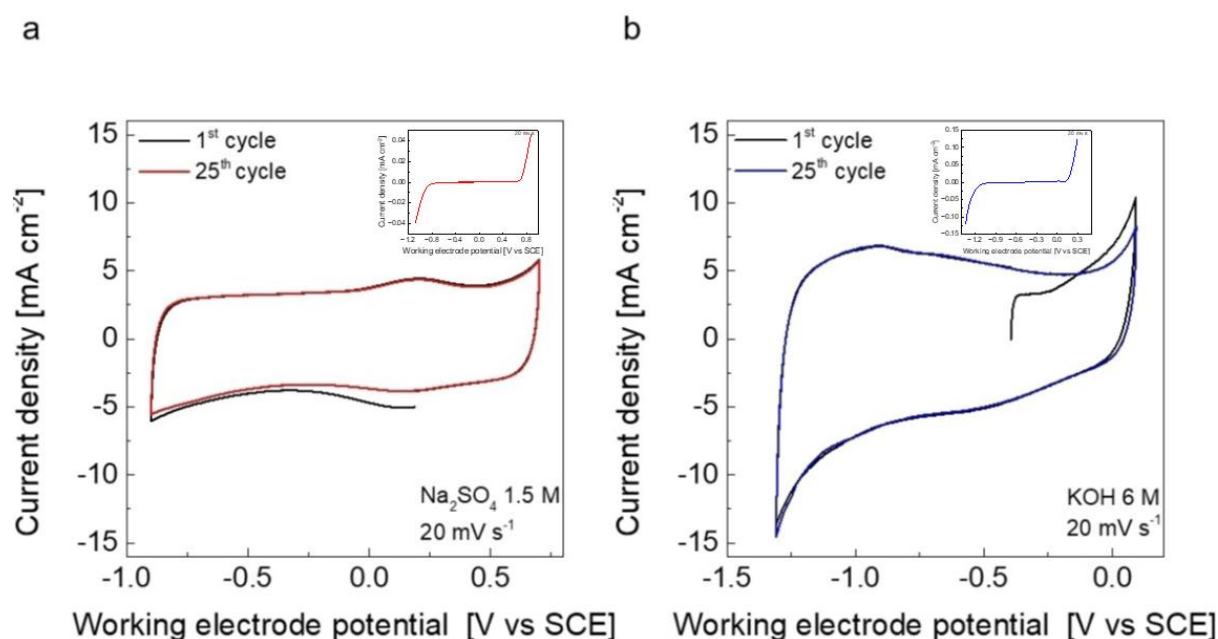
Figure 4.13 (a) CVs of AC electrodes with MA-modified chitosan binder at 20 mV s⁻¹ in Na₂SO₄ 1.5 M and (b) and in KOH 6 M, with the respective inset of electrochemical stability window of electrolytes, performed with SS//AC PTFE at 20 mV s⁻¹.

This peak could be attributed to redox processes taking place at the carbon electrode surface, involving oxygen containing groups e. g., alcohol and carboxylic acids, according

to equation (6) and (7) [154,155]:

$$R - C - OH \rightleftarrows R - CO + H^+ + e^- \tag{6}$$

$$R - COOH \rightleftarrows RCOO + H^+ + e^- \tag{7}$$
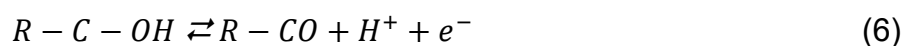
These functional groups are formed during the activation process of porous carbon, and therefore can be reversibly oxidized and reduced especially in acidic and neutral environment. The faradaic contribution to the total capacitance was estimated to be less than 4%. This amount was calculated, considering the baseline of the capacitive profile by integrating the area of the peaks.

Figure 4.14 shows the Nyquist plots for symmetrical cells with AC MA electrodes with Na_2SO_4 and KOH electrolytes, recorded in three-electrode mode after cell assembly (t_0) and after 50 cycles at 0.5 A g^{-1} (t_1). Fitting curves were obtained using the equivalent circuit $R_1(R_2/Q_2)Q_3$ displayed in Figure 4.15, where R_1 is the electrolyte resistance, R_2/Q_2 represent the resistance and the capacitance (as constant phase element, CPE) in parallel, related to the charge transfer of the faradaic process, and Q_3 is the CPE attributed to the double layer of a non-ideal capacitor, visible as a line with angles <90° with respect to X axis.

a

b
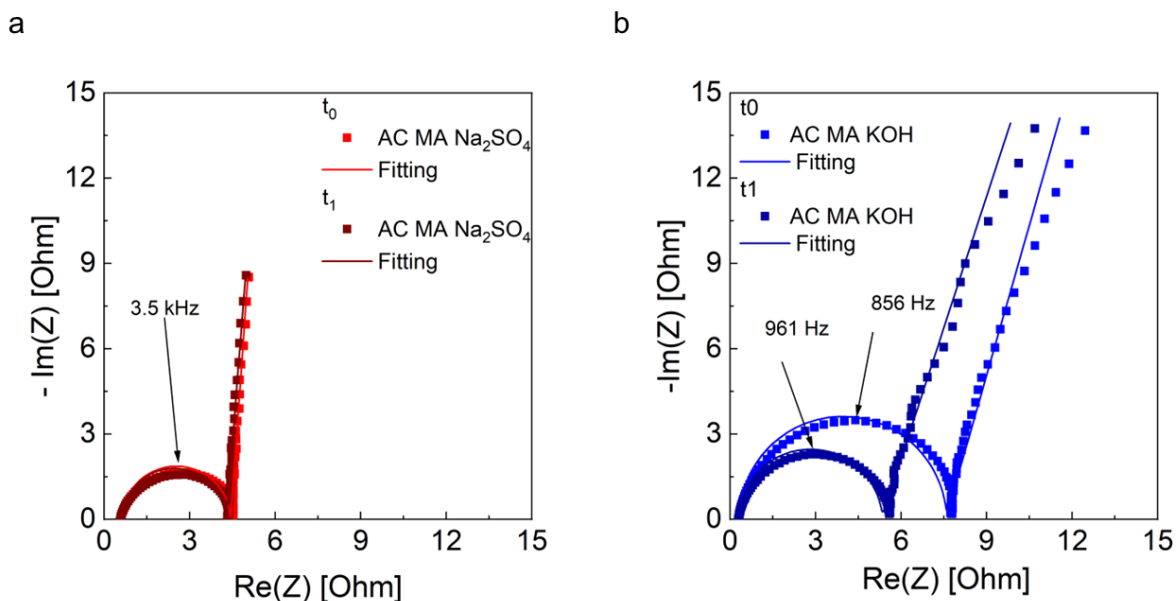
Figure 4.14 Nyquist plots of EIS spectra, using silver as reference electrode and fitting curves of AC electrodes (a) in Na_2SO_4 1.5 M and (b) KOH 6 M recorded after cell assembly (t_0) and after 50 cycles at 0.5 A g^{-1} (t_1). Frequency range 100 kHz-0.1 Hz, 20 points per decade, ±5 mV amplitude

It is possible to identify the electrolyte resistance (R_1) as the point at the highest frequency, the semicircle due to the charge transfer resistance and the related double layer capacitance, and an almost linear part ascribed to the non-ideal double layer capacitance of the electrode, with the intercept with the X-axis providing an indication of the total resistance of the electrode equivalent series resistance (ESR).
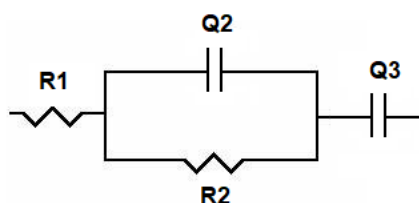
Figure 4.15 Equivalent circuit for the fitting of the Nyquist plots in Figure 4.14.

Table 4.3 lists the parameters of the equivalent circuit obtained from the fitting. The electrolyte resistance R_1 of the cell with Na_2SO_4 is higher than that of the cell with KOH, in agree with the conductivity values shown in Table 4.4. The AC MA electrode in Na_2SO_4 (Figure 4.16) shows smaller charge transfer resistance (R_2) than in KOH, which does not vary after 50 cycles. The impedance spectra were fitted, by Q_3 in the low frequency region. The straight lines with angles near 90° were ascribed to the double layer of a non-ideal capacitor. The Table also displays the data of ESR evaluated by EIS and GCD cycles at 0.5 mA cm^{-2}. The values of the ESR from the two techniques are in good agreement. The ESR value of the electrode in KOH is slightly higher, probably due to a noncomplete wetting of the electrode. The decrease of ESR value over cycling confirms our hypothesis. Resistances values obtained from our electrodes are good and comparable with other results reported in literature [149].

Electrolyte	Na_2SO_4 1.5 M	Error	KOH 6M	Error

Components		[%]		[%]
t_0				
R_1 (Ω)	0.64	4.5	0.32	8.4
R_2 (Ω)	3.8	2.1	7.2	4.1
Q_1 ($\Omega^{-1} \cdot s^\alpha$)	$1.1e^{-5}$	27.5	$2.1e^{-5}$	34.4
α	0.99	2.6	0.99	3.2
Q_2 ($\Omega^{-1} \cdot s^\alpha$)	0.18	4.9	0.10	10.6
α	0.96	3.3	0.82	8.2
ESR_{EIS} (Ω)	4.4	2.0	7.5	3.9
ESR_{GCD} (Ω)	4.5	2.6	7.6	3.8
t_1				
R_1 (Ω)	0.64	3.2	0.31	8.5
R_2 (Ω)	3.7	2.1	5.0	4.4
Q_1 ($\Omega^{-1} \cdot s^\alpha$)	$1.0e^{-5}$	28.8	$2.7e^{-5}$	38.9
α	0.99	2.6	0.99	3.7
Q_2 ($\Omega^{-1} \cdot s^\alpha$)	0.18	4.8	0.099	9.3
α	0.95	3.2	0.8	7.0
ESR_{EIS} (Ω)	4.2	2.1	5.3	2.7
ESR_{GCD} (Ω)	4.2	2.4	5.5	3.2

Table 4.2 Fitting parameters of the equivalent circuit components, and ESR values from EIS and from GCD, of AC MA electrodes in different electrolytes just after assembling (t_0) and after 50 cycles at 0.5 A g^{-1} (t_1)

It is worth mentioning that self-standing electrodes directly placed on the stainless-steel collector of the cell may suffer of poor contact, contrarily to the electrode in which the current collector provides a uniform contact between the electrode material and the cell terminal. Nevertheless, AC MA electrodes show lower overall resistance in Na_2SO_4 values compared to AC EDC electrode as could be seen in Figure 4.16.
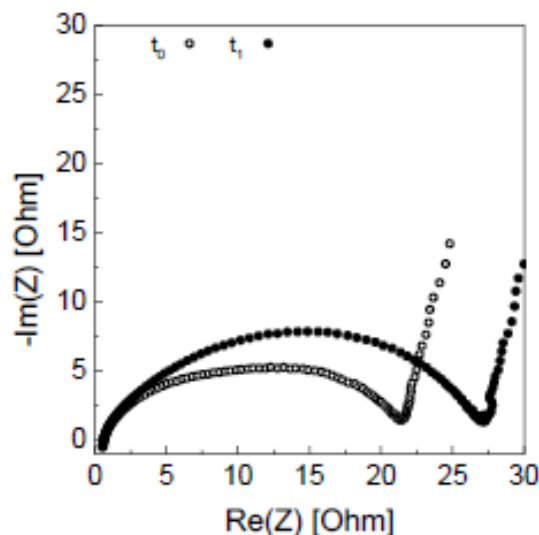
Figure 4.16 EIS spectra of AC EDC electrodes in Na$_2$SO$_4$ 1.5 M recorded after cell assembly (t$_0$, plain circles) and after 50 cycles at 0.5 A g^{-1} (t$_1$, full circles)

The electrochemical behaviour of AC MA electrodes was evaluated in Na$_2$SO$_4$ and KOH electrolytes by GCD at different current densities in three electrodes symmetrical cells. We performed the tests in triplicate, and the mean capacitance and capacitance retention are reported in the Table 4.5. In Figure 4.17 are reported the results of the best performing electrodes.

Current density Electrode	0.5 A g^{-1}	1 A g^{-1}	2 A g^{-1}	5 A g^{-1}
AC MA in Na$_2$SO$_4$	141 ± 9	122 ± 4	95 ± 5	69 ± 3
AC MA KOH	106 ± 8	82 ± 5	59 ± 3	40 ± 2
AC PVdF in Na$_2$SO$_4$	113 ± 4	94 ± 3	71 ± 4	29 ± 3

Table 4.3 Capacitance values with relative errors at different specific currents of AC MA and AC PVdF electrodes in Na$_2$SO$_4$ 1.5 M and in KOH 6 M.

Capacitance values, shown in Figure 4.17, are quite interesting for activated carbon electrodes operating in aqueous EDLCs [149], exhibiting initial capacitance values above

145 F g^{-1} and 110 F g^{-1} in Na$_2$SO$_4$ and KOH, respectively, at the lowest specific current. These values are significantly higher than those obtained with AC EDC electrodes, reported in Figure 4.18. Despite the better ionic conductivity of KOH, listed in Table 5, capacitance values obtained in Na$_2$SO$_4$ are higher at each specific current.

	Na$_2$SO$_4$ 1.5 M	KOH 6 M
Conductivity [mS cm^{-1}]	114.2	584.4

Table 4.4 Measured ionic conductivity of different electrolytes at 30° C

This is probably attributed to the electrostatic repulsion between OH$^-$ and the deprotonated oxygen containing groups, - COO$^-$ and - RO$^-$ on the activated carbon surface, that hinder the formation of the double layer [149].
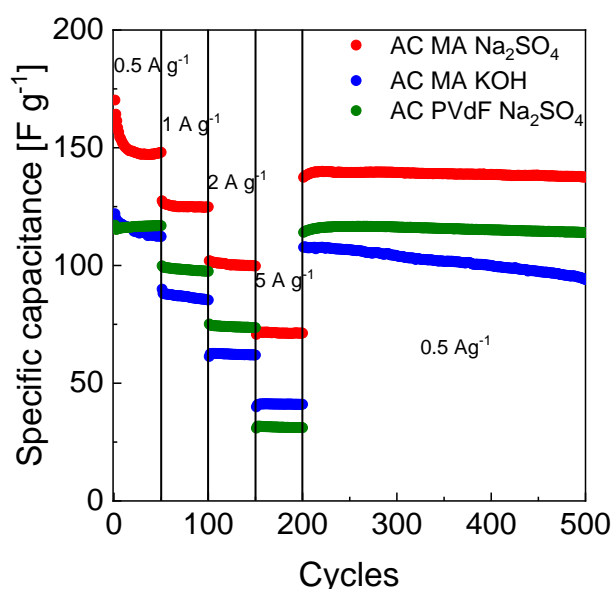
Figure 4.17 Specific capacitance values recorded at different specific currents of AC MA electrodes in Na$_2$SO$_4$ 1.5 M (red circles), in KOH 6 M (blue circles), and AC PVdF electrodes in Na$_2$SO$_4$ 1.5 M (green circles).

Figure 4.17 also reports the capacitance values of an AC PVdF electrode. Despite the good stability in aqueous electrolyte, the electrodes with PVdF exhibited lower specific capacitance than AC MA electrodes in the same electrolyte, Na_2SO_4 1.5 M. Lower values could be explained by the higher hydrophobic behaviour of PVdF binder that doesn't enable a good wetting of the microporosity of active material. After 200 cycles ad different current values, AC MA electrodes almost recovered the steady capacitance values at 0.5 A g^{-1} and remained stable for over 500 cycles in Na_2SO_4, while capacitance values in KOH suffered a steady decrease. This phenomenon may be attributed to the water reaction, given that the charge/ discharge cycles were carried out in the maximum voltage window of 1.2 V.

For comparison, Figure 4.18 reports the cycling performance of an AC EDC electrode in Na_2SO_4 1.5 M. As could be seen from the comparison, AC MA electrodes scored significantly higher capacitance values, at all specific currents, compared to AC EDC electrodes in the same electrolyte. The reason may be due to the fact that, unlike crosslinking with EDC, the modification of chitosan with MA does not hinder the mobility of ions within the porous electrode as well as making certain porous regions unreachable because of steric hindrance. This behaviour is in accordance also with the EIS spectra; where it could be noted that the charge transfer of AC MA appears less resistive compared to what is seen with AC EDC electrodes in Na_2SO_4 1.5 M. Electrodes that are more porous, permit a better mobility of the ions, and this will result in lower resistances value on the right-side branch, low frequencies, on the Nyquist plots.
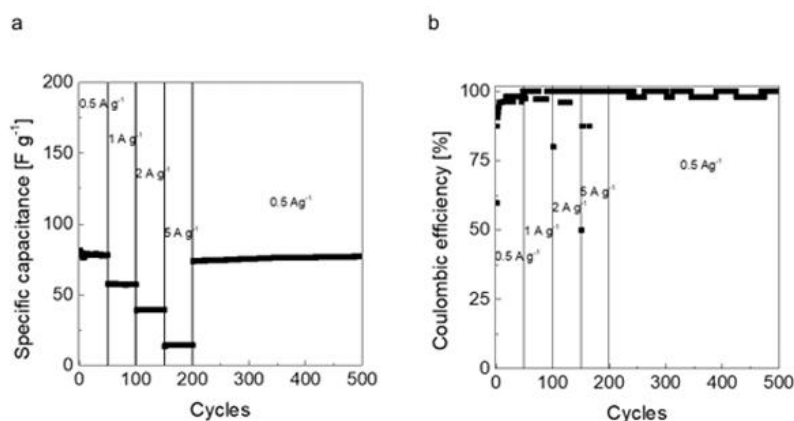
Figure 4.18 (a) Rate capability at different current densities of AC EDC chitosan binder in Na$_2$SO$_4$ 1.5M and (b) coulombic efficiency values

In the initial cycles, AC MA electrode in KOH shows higher efficiency values, reported in Figure 4.19, and reached values close to 99%. AC MA electrodes in Na$_2$SO$_4$, shows lower initial values that stabilize after fifty cycles reaching comparable values.

The differences in the coulombic efficiencies of the initial cycles are attributed to the different bulkiness of the SO$_4^{2-}$ anion with respect to OH$^-$. Sulphates ions attachment to the surface or penetration into the pores vary with surface impurities and may not remain the same after several charge-discharge cycles [149].
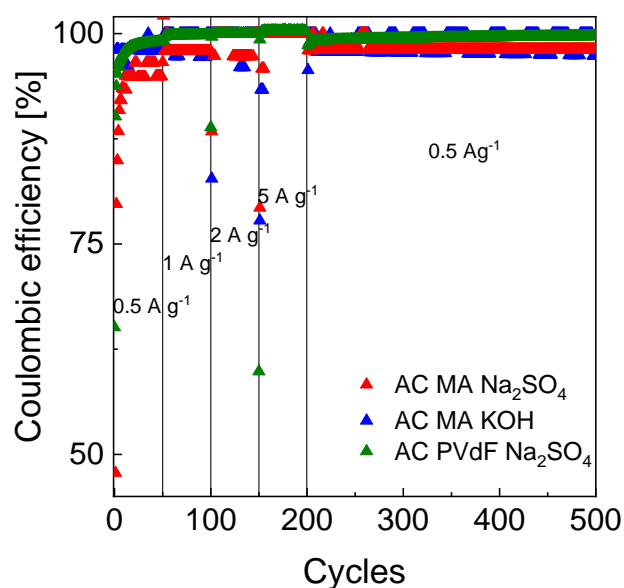
Figure 4.19 Coulombic efficiency values recorded at different specific currents for AC MA electrodes in Na$_2$SO$_4$ 1.5 M (red triangles), in KOH 6 M (blue triangles) and AC PVdF electrodes in Na$_2$SO$_4$ 1.5 M (green triangles).

The AC MA electrodes demonstrated to be stable in aqueous environment, capable of operating either at low and high specific current, as visible from the typical triangular profile of charge and discharge cycles in Figure 4.20. Nevertheless, charge and discharge profiles are not perfectly straight but appears slightly bended, because of the different double layer formation process, involving ions stored and released close to electrode surface, with less hindrance, and ions contained in the inner pore structure of the electrode.
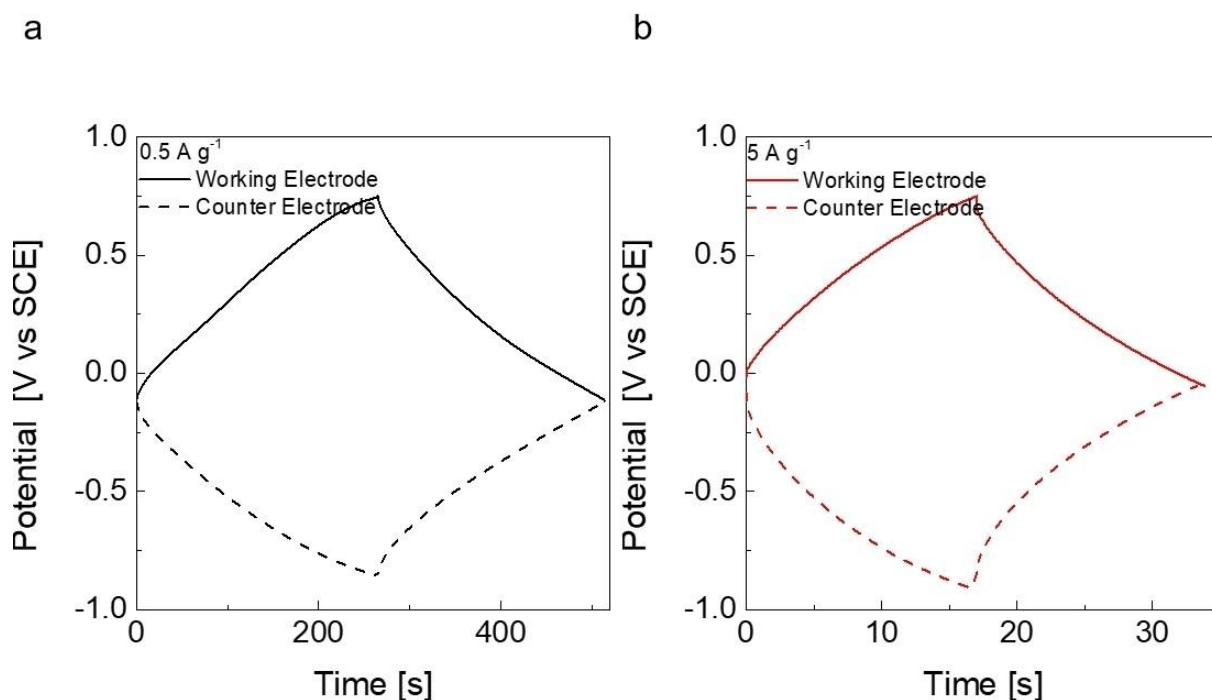
Figure 4.20 Potential profiles of the positive and negative AC MA electrodes during GCD cycles (a) in Na_2SO_4 1.5 M at 0.5 A g^{-1} (black line) and (b) 5 A g^{-1} (red line)

The electrochemical stability of the AC MA electrodes upon prolonged cycling at 0.5 A g^{-1} in Na_2SO_4 is shown in Figure 4.21. The tests were carried out in triplicate and the average values of specific capacitance and capacitance retention were approximately 141 ± 9 F g^{-1}, and 89 ± 4 % respectively. The reported results are those of the best performing electrodes. After the initial 700 cycles, electrodes demonstrated quite stable, reaching a final value of 93.4% capacitance retention after 5000 cycles.
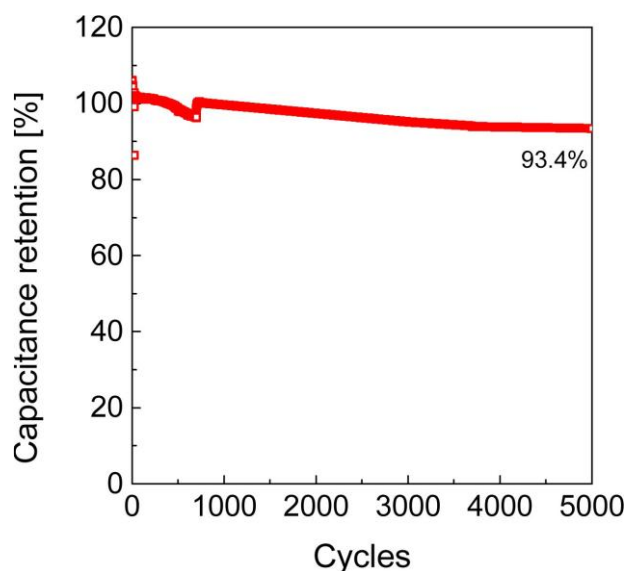
Figure 4.21 Capacitance retention of AC MA electrode in Na$_2$SO$_4$ 1.5 M over GCD cycles at 0.5 A g^{-1}

Finally, we evaluate the possibility to easily recover the electrode material, even if it is merely carbon, by dissolving the electrode in the same solution of 1 vol.% acetic acid used for chitosan dissolution during electrode preparation. After 16 hours of immersion in 10 mL of solution, the electrode was sonicated for 30 minutes at 40°C. The suspension of the electrode material (activated and conductive carbon), visible in Figure 4.22, was centrifuged at 5000 rpm for 5 minutes. The powder was then dried in oven at 60°C overnight and weighted. Nearly 70% of the carbonaceous materials has been recovered, demonstrating, in addition to the sustainability of this approach towards more sustainable electrode processing and batteries manufacturing, also its suitability in the frame of circular economy.
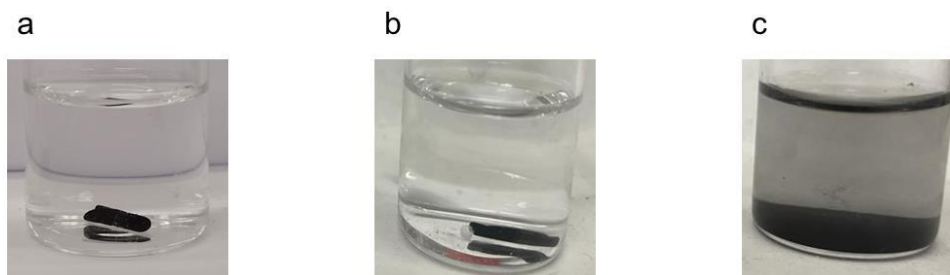
Figure 4.22 Different steps of recycling of AC MA electrodes: (a) immersion in 1% vol. solution of acetic acid, (b) after 16 hours and (C) after sonication.

4.7 Application and specification

As reported in this chapter, adopting binder made of biopolymers with an all-aqueous electrode process for aqueous based EESS, guarantees a significant step forward for a lower environmental impact of electrode preparation. Except for aqueous zinc ion batteries, currently water-processable binders from biopolymers are not viable for aqueous systems due to progressive dissolution into the aqueous medium. However, with some easy and simple chemical modification of the binder, it could be made water insoluble. Moreover, by choosing an appropriate binder that provides an adequate flexibility, it is also possible to obtain free-standing electrodes, avoiding the use of titanium or stainless-steel current collectors. Although demonstrating lower power and energy densities because of narrower electrochemical stability window compared to organic electrolytes-based systems, combining the aqueous electrode process, with aqueous electrolytes and absence of current collectors it seems possible to manufacture aqueous EESS with a reduced environmental impact as well as the cost, that could find applications where devices dimensions doesn't represent a strict requirement.

5 Batteries separator

Another possible strategy to increase the sustainability and recycling of LIBs materials could come from innovative separators originated from the adoption of novel types of polymers or polymeric mixture. This chapter investigates the suitability of possible membranes used as separator for LIBs, obtained from polymers less harmful to the environment, compared to the current state of art. They can be originated from renewable polymer sources, or even being biodegradable once the battery life cycle comes to an end, with manufacturing techniques that make use of aqueous processes.

An alternative and smart deposition technique to manufacture polymeric film as LIBs separator, will be introduced and explored in the following sections. The experimental work presented in Chapter 5.4 is focused on the morphological effect of different casting parameters on the final membrane, and the electrochemical performance of the obtained film. A polymeric membrane obtained by electrospinning at the Department of Civil, Chemical, Environmental, and Materials Engineering, in the framework of a collaborative study among the Universities of Trento and Bologna, previously used for bio-medical applications, was investigated to verify its viability as separator for LIBs.

5.1 Separator function

In Chapter 2.3.3 was described the importance of a porous membrane for LIBs operating with liquid electrolytes. The separator, situated between the anode and cathode, does not participate directly in electrochemical reactions. However, its structure and properties could affect the cell performance. Its primary function is to

prevent physical contact between electrodes, dividing the anode and cathode while also acting as an electrolyte reservoir, facilitating the mass transport of ions and avoiding lack of electrolyte. Modern separators must meet additional requirements, particularly for applications in electric vehicles and energy storage stations, where high thermal and mechanical stability, along with excellent electrolyte wettability, are essential [156].

To prevent physical contact between the electrodes, the separator must be resistant upon various factors including, but not limited to, impurities contaminants originated during manufacturing, chemical environment throughout the cell's life cycle, lithium dendrite growth during cycling, compression and mechanical stress from cell assembly and operation, and thermal shrinkage that could lead ultimately to short circuits [157,158]. Table 5.1 summarizes the general requirements that should be considered while selecting the appropriate candidate as a separator.

Parameter	Requirement
Chemical and electrochemical stabilities	Stable for a long period of time
Wettability	Wet out quickly and completely
Mechanical property	>1000 kg·cm^{-1} (98.06 MPa)
Thickness	20-25 μm
Pore size	<1 μm
Porosity	40-60%
Permeability (Gurley)	<0.025 s·μm^{-1}
Dimensional stability	No curl up and lay flat
Thermal stability	<5% shrinkage after 60 min at 90 °C

Table 5.1 General requirements for separators used in LIBs

An ideal separator would exhibit zero ionic resistance; however, in practice, low ionic resistance can be achieved through high porosity. Typically, conventional polyolefin separators have a porosity ranging from 30% to 55% [159]. Originally developed for primary LIBs applications, the processes used to create pores in commercially available polyethylene or polypropylene separators involve the precise stretching of an extruded thin film, with or without the use of additives [159,160].

Thick separators (>50 µm) reduce areal power density, for this reason most commercial batteries utilize thin (<20 µm) polyolefin microporous separators. These separators offer several benefits, including good mechanical strength, excellent chemical stability, low cost, and effective thermal shutdown properties [161]. Dual-layer poly(ethylene)/poly(propylene) (PE/PP) and trilayer (PP/PE/PP) separators offer enhanced safety compared to single-layer separators. Currently multilayer PE/PP separator, visible in Figure 5.1, produced through a combination of multilayer coextrusion and thermally induced phase separation, are the most diffuse membranes employed for LIBs; demonstrating high thermal stability, thanks to PP layers and effective shutdown capability across a broad temperature range, due to the low melting PE [162,163].

Figure 5.1 Schematic of a commercial trilayer poly(ethylene)/poly(propylene)/poly(ethylene) (PE/PP/PE) separator

However, functionalization of separator offers the possibility to meet the requirements of end-users and LIB chemistries, tailoring the properties through interactions built with the electrolyte and/or the electrodes [162], for example inhibiting dendrite growth once the dendrites reach separator surface, helping to promote the creation of a stable SEI or even obtaining anti-shrinkage properties [164–166].

5.2   Industrial LIB assembling and separator manufacturing

During my doctoral studies I've also had the opportunity to spend a short stay into Manz Italy s.r.l. company and see the industrial processes involved in battery manufacturing and, specifically, the lamination process of electrodes and separators. Here is a short overview of common industrial separator production processes and cell assembly.

Even if the separator market is dominated by polyolefin membranes, nowadays they're facing technological limitations in wettability, porosity, shrinkage, and meltdown resistance. Given that battery reliability and safety are critical and closely tied to the properties of separator materials, there is a growing demand to enhanced separators without sacrificing performance or increasing cost. This has reignited global research and development efforts, both in academia and industry, towards innovation and improved separator technologies [167].

Wet and dry processes are the primary technologies used for large-scale manufacturing of commercially available microporous separators, producing rolls up to 1800 m in length. Both methods involve two fundamental steps: an extrusion step to produce a thin film and a stretching step to develop the microporous structure. The dry method generates oriented micropores with slit-like characteristics, while the wet

process forms interconnected, non-oriented spherical or elliptical pores. The schematics of these two processes are represented in Figure 5.2. These processes became the most employed, especially the wet process, with a market share around 80% of the commercial separators, thanks to [167]:

- o Versatility: could be adopted for a wide range of polymers (both semi-crystalline and amorphous) even with heavy weighted polymers.
- o Continuous process: until the raw polymers are fed into the extruder, the manufacturing process never stops
- o Flexibility: the structure and porosity of the separators can be influenced by various factors, including solution composition, quenching temperature, stretching rate, and the solvent evaporation or removal during the solidification processes.

However, solvent extraction and recovery represent the drawbacks of this membrane deposition production techniques, with a considerable environmental as well as cost impact due to the employment and evaporation of alkanes solvent use during extrusion.
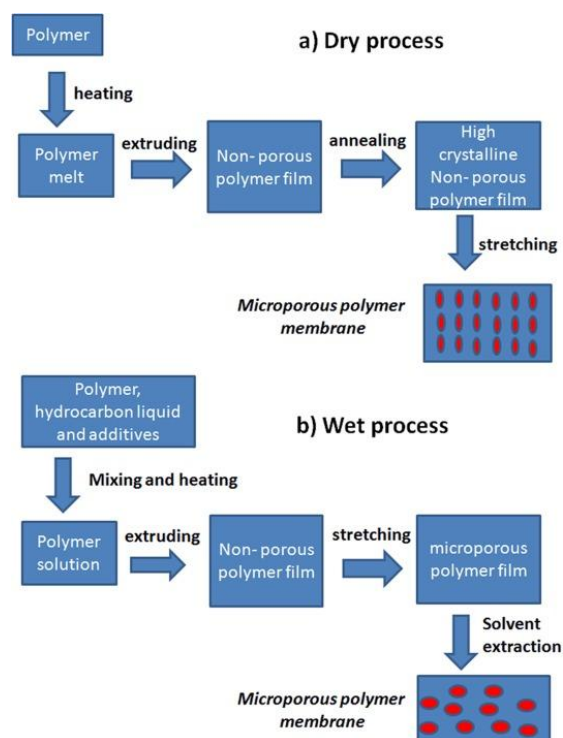
Figure 5.2 General procedures for producing microporous separators: a) dry process, b) wet process [167]

Once the separators are properly formed, dried and cooled off, typically on a flexible plastic substrate made of polyester (Mylar), they are transferred to a dry room, where they are combined with already prepared and dried electrodes for cell production, through different assembling processes: Z-folding, stacking and winding (or roll-to-roll) processes.

The Z-folding process involves feeding the separator continuously in a zigzag folding pattern while inserting sheet electrodes at specific points. This method introduces compressive forces and bending stress to the separator. The level of stress experienced depends on the design of the folding mechanism that creates the Z-fold pattern. During battery operation, volume strain further contributes to compressive forces, impacting the separator's structural integrity [168].

The stacking process involves the alternating layering of electrode and separator sheets on top of each another. Unlike Z-folding, this method applies only a compressive stress to the materials, with no bending stress involved. However, during battery operation, volume strain can introduce additional compressive forces [168].

In cylindrical and prismatic winding processes, the electrode and separator materials are attached to a winding core and continuously wrapped around it. The minimum bending radius in these processes corresponds to the thickness of the electrodes. At the conclusion of the winding process, the winding core may either remain as part of the battery or function as a permanent component of the winding structure [168].

Although the winding process has been developed for a relatively long time, with mature technology, low cost and high yield for cylindrical and prismatic batteries production, this process allows only for manufacturing of lithium batteries with regular shapes. In the winding process the coated electrodes are bent and deformed with an angle or helix of winding is usually within the range of 25-85 ° to the axis of rotation (C-angle), while in the stacked and especially Z-folding processes the lamination of electrodes-separator component provides a better contact and prevents failures, with the possibility to form special-shaped batteries with higher flexibility. Key aspects between the two production processes involving lamination or winding are highlighted in Table 5.2.

	Lamination with Stacking/Z-folding	Winding
Energy density	The space utilization rate is higher as visible in the figure:	There is a C angle that lower the utilization rate as shown:

Stable structure	The internal structure is unified, and the charge and discharge are consistent	The existence of C angle leads to uneven internal rate of charge and discharge
Safety	The stress distribution is more consistent which can keep the interface smooth and have higher stability	The bends are prone to potential problems such as diaphragm stretching, material loss and burrs
Cycle life	Low internal resistance, reducing battery heating during fast charging, improve battery stability extending serving cycle	Rolled electrodes are easier to deform later, shortening the serving cycle life of the cell
Productivity	Production rate is typically slower due to the additional steps. Usually, the rate is about 6-8 pouch cells per minute	The process is faster, and the production rate is about 12-13 pouch cells per minute
Technology maturity	Lots of parameters to optimize and higher complexity of the equipment	Fewer components and parameters to be adjusted that are already well known

Table 5.2 Comparison between laminating and winding processes characteristics

The electrodes and separator are then winded or stacked layer by layer ready to be laminated, to form the cell's internal structure. Alignment between the three components: anode, cathode and separator prior to lamination is critical for the future life cycle and performances, alternatively the cell or even the module could underwent into short circuit, when the separator doesn't cover all the surface between the two electrodes, and loss of performance in the case the electrodes aren't properly facing

themselves hence hampering the diffusion of ions, not allowing a uniform intercalation/insertion and, in the case of coin cells type cells, it could also lead even to undesired lithium plating on the metal case bottom during formation cycles [169].

5.2.1   Lamination process

In the lamination process, schematized in Figure 5.3, the separator is laminated onto the electrode, forming a material and physical connection between their interfaces. This bond is created by the thermal softening of an adhesive agent, typically located on the separator's surface, and the application of pressure to the electrode-separator composite. Generally, a line load is applied using a rotating pair of rollers or a revolving metal belt. The required thermal energy can be applied simultaneously with the force, such as through temperature-controlled rollers, or separately in a preheating zone. Both the electrodes and separators can be fed into the lamination process as continuous web material or as discrete pieces. A combination of web-based feeding for the separator and feeding of cut-to-size electrodes is also possible [170].

For the homogeneous, reproducible, and non-destructive application of a continuous separator web onto a discrete electrode, six parameters are critical, two of them prior to lamination while the others are directly related to the process:

o   Web tension is adjusted using a tension control dancing system, as employed in the established Z-fold process. The active dancer system, which is freely parameterizable and features position and torque control, is particularly effective for this purpose, adjusting web tension of the separator prior to folding process. Additionally, the web edge position is monitored by an optical measuring unit and corrected as needed using a rotatable deflection roller.

- Deposition accuracy is controlled through an optical measuring unit and adjusted via a rotatable deflection roller. Precise placement of the electrodes is achieved through a handling system, ensuring proper overlap of individual sheets in the resulting cell stack. Insufficient overlap can cause significant losses in the electrochemical performance of the battery cell, like issues observed in stacking electrode without lamination, i.e. winding process.

  During the lamination process, material feed rate, roll gap, contact pressure on the laminate, and process temperature are crucial in determining the properties of the resulting laminates. These parameters can be monitored and controlled using established sensor technologies.

- The material feed rate is determined by the rotational speed of the rollers and is monitored using rotary encoders. Ensuring slip-free operation between the rollers is essential to prevent wrinkling or damage to the separator. To avoid slippage, industrial systems often employ a coupled drive mechanism via a belt drive, ensuring precise synchronization.

- The roll gap is mechanically adjusted and limited by mechanical stops, allowing active opening and closing based on the materials used. Typically, a static roll gap is not fixed; instead, the opening width adapts dynamically through force control during operation. When using rubberized or soft rolls, active control is often unnecessary as the roll material naturally accommodates the electrode edges entering the gap. However, when hardened rolls are used, the potential for electrode edge damage increases, necessitating active gap control to prevent damage.

- The contact pressure applied by the rolls affects the adhesion of the electrodes to the separator and must be carefully managed to prevent damage. This pressure is typically generated using pneumatic or hydraulic systems and is measured either indirectly via the pressure values of the medium or directly using load cells integrated into the rolls.

- A specific process temperature is required to soften the binder without causing irreversible decomposition. The temperature in preheating zones and rollers is monitored with integrated contact sensors that have short response times, while the surface temperature of the laminate is measured using non-contact pyrometers. However, measuring the temperature at the contact area between the separator and electrode remains challenging, as direct measurement is not feasible. This limitation complicates the control and regulation of this parameter based on direct feedback.

Together, these parameters work in tandem to ensure the quality and results of the laminated product, requiring precise control and careful calibration during the lamination process.
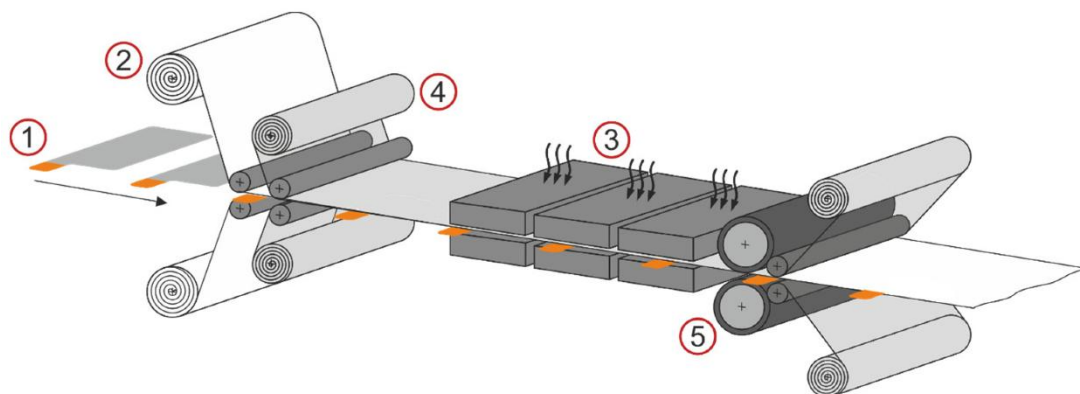
Figure 5.3 Schematic representation of the lamination process with discrete electrode feed (1), web-bound separator feed (2) and a separate preheating zone (3) in front of the lamination rollers (5). A protective film (4) covers the electrodes and separator during lamination [170]

5.3   *Membrane deposition techniques*

Separators can be categorized into three main types: microporous, nonwoven mats and composite. Gel-polymer electrolyte is another category of materials that can be also viewed as separator. These categories will be explored in detail in the following section. Various manufacturing techniques are employed in their production, including the already mentioned dry and wet processing, solution casting, phase inversion and electrospinning. However, for large-scale commercial microporous separators, the primary manufacturing methods are the wet and dry processes. Additionally, the phase inversion method is commonly used for microporous separator production, while nonwoven mats are fabricated using techniques mainly electrospinning processes [158,167,171].

5.3.1 Solution casting

The solution casting method is one of the most widely used techniques for preparing separators for lithium-based batteries at lab-scale because of its simplicity and feasibility. In this method, a polymer and desired additives are dissolved in a single solvent or in mixed solvents up to reach a stable and homogeneous solution. This solution is then evenly coated onto a substrate, typically a glass or steel plate depending on the interactions between polymer and substrate, using a doctor blade. After coating, the solution is dried, according to the polymer thermal properties at a desired temperature. Once dried, the resulting microporous film is peeled off from the substrate [171]. In Figure 5.4 are represented the typical step of solution casting process. The morphology and porosity of the separator is influenced by several variables such

as the solubility of the polymers, the temperature and rate of solvent evaporation, and the presence of non-solvents in the system. Additionally, the thickness of these separators can be easily adjusted by modifying the gap depth of the doctor blade, as visible in Figure 5.5b. However, non-uniform pore size and distribution can occur due to varying evaporation rates within the solution, which may negatively impact the mechanical strength of the separator and electrochemical performances [171,172].
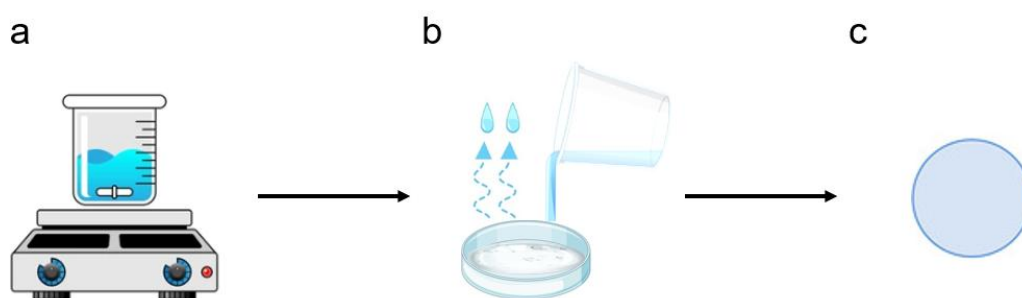
Figure 5.4 Solvent casting method scheme (a) polymer are dissolvent under stirring and then (b) poured into an appropriate substrate and let the excess of solvent evaporate and (c) finally the peeled membrane is obtained

5.3.2 Phase inversion

The phase inversion method has been already widely employed for creating porous structures. This deposition technique allows for pore formation without the need for stretching, therefor reducing thermal shrinkage and product defects commonly associated with the stretching process. Typically, a polymer solution is at first dissolved in an appropriate solvent and then, once completely dissolved, it is casted to form a thin film and subsequently immersed in a coagulation bath containing a non-solvent, in which the polymer is not soluble. The phase inversion process is schematized in Figure 5.5. The miscibility of the solvent and non-solvent triggers an exchange that creates a thermodynamically metastable or unstable system, resulting in the development of a porous structure. Consequently, the properties and miscibility of the

solvent and non-solvent play a critical role in determining the morphology and porosity of the final membrane [167,171,173].
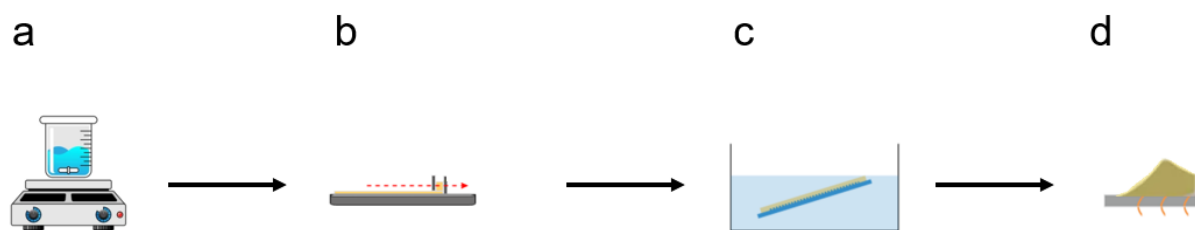
Figure 5.5 Pathway to obtain membranes from phase inversion process. At first (a) polymer is dissolved in an appropriate solvent and after complete dissolution (b) are roll casted on a substrate with a desired thickness. Then, (c) the substrate with the casted polymer is immersed in the coagulation bath containing the antisolvent and finally after drying (d) the polymer membrane is removed from the substrate

5.3.3 Electrospinning

Nonwoven mat separators are fibrous mats created by bonding randomly oriented fibers through chemical, thermal, or mechanical methods. Both natural and synthetic materials are utilized to produce the fibres used in nonwoven separators. However, nonwoven separators produced using wet- and dry-laid methods typically exhibit excessively large pore sizes (20-50 µm) and increased thickness (100-200 µm). While these characteristics help prevent short circuits, they come at the cost of reduced battery energy [174,175].

To address these limitations, electrospinning technology has been developed as a more advanced method for producing thin nanofiber separators. This technique enables the creation of fibres with diameters at the sub-micrometer or nanometer scale, offering significant potential for applications in lithium-ion batteries [167].

Electrospinning is a straightforward and versatile technique for producing thin, continuous polymeric fibers with diameters at the sub-micrometer or nanometer scale.

84

Electrospun mats are significantly thinner than those created using other mat-forming processes.

A typical electrospinning setup, represented in Figure 5.6, includes a high-voltage power supply, a syringe, a spinning nozzle, and a grounded collector. An electric potential is applied between the polymer solution in the syringe and the metallic collector. When the electric field overcomes the surface tension of the polymer solution droplet at the nozzle tip, a charged liquid jet is ejected, depositing nanofibers onto the grounded collector to form the nonwoven structure. The mat morphology is influenced by factors such as the solvent evaporation rate, polymer concentration, the distance between the nozzle tip and the collector, and the applied voltage [167,176,177].
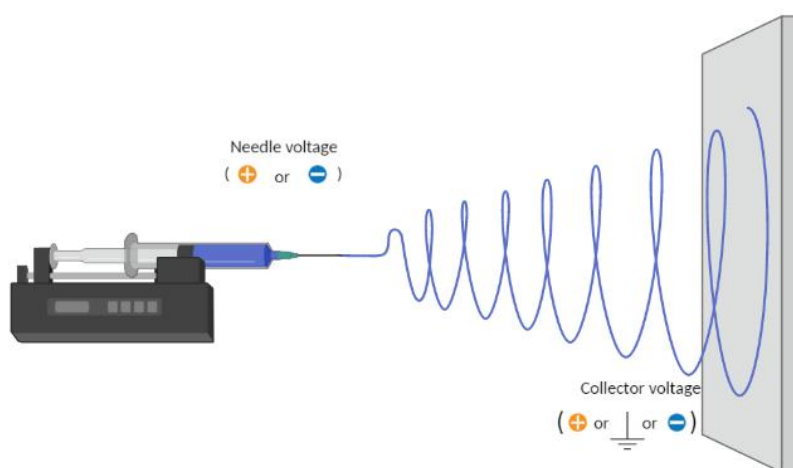
Figure 5.6 Mechanism of electrospinning system and deposition

Electrospun nonwoven mats exhibit higher porosity, increased pore sizes, and greater permeability compared to conventional nonwoven mats. The mechanical strength of separators produced through electrospinning remains inferior to that of commercially available separators. Nonetheless, in recent years, efforts have been made to scale

up the production of electrospun separators, but low production capacity and high manufacturing costs remain a challenge for the wider adoption of this technique [171,178].

In Figure 5.7 are summarized the main characteristics and differences between the main separator preparation techniques.
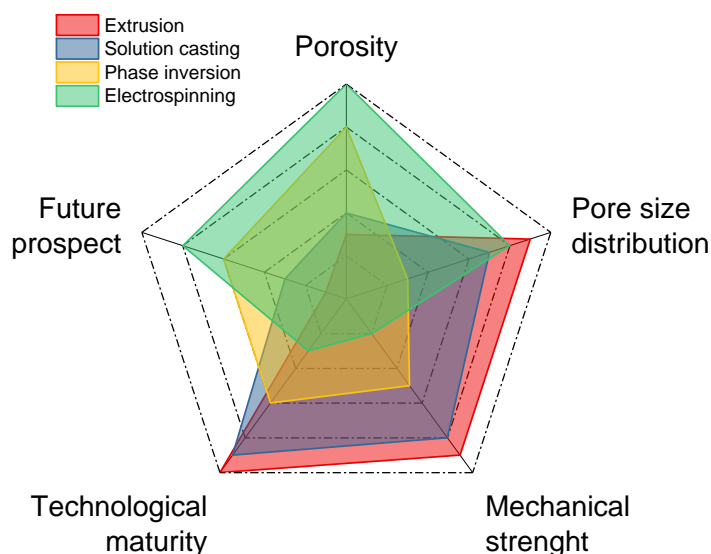
Figure 5.7 A summary of different separator preparation methods

5.4 *All-aqueous phase inversion process for biopolymer-based separator*

Keeping in mind the overall theme about sustainability for LIBs, in this section it was evaluated the use of total aqueous process to obtain membranes by phase inversion. The choice of phase inversion process and the use of aqueous solution for both solvent and anti-solvent was twofold: in addition to the aforementioned sustainability purposes, also the potential industrial feasibility of the whole process is taken into account.

Phase inversion deposition is a technique that could be implemented in cell assembly line that works in continuous and the use of coagulation bath made of water reduces the environmental and human health risks as well as the costs during both the coagulation and the drying processes.

Vinyl alcohol-co-ethylene (EVOH) was the polymer selected to be used as separator for LIBs, since to our present knowledge it has only been studied as membrane for LIBs trough electrospinning process using hazardous organic solvents [179–182].

EVOH is a versatile copolymer made of ethylene and vinyl alcohol. The structure is shown in Figure 5.8. These materials are highly crystalline and are produced with various levels of ethylene content, ranging from 30 to 50 % molar (20 to 40 % wt.) of ethylene content. The presence of -OH groups in the structure results in strong intermolecular hydrogen interactions, and it is also reported that EVOH is partially biodegradable depending on the content of ethylene monomer. EVOH is commonly used as an internal layer in multilayer food packaging films, blow-molded rigid containers, and automobile gasoline tanks, serving a variety of purposes. Industrially it is manufactured using standard dry and wet melt processing methods [183–186].
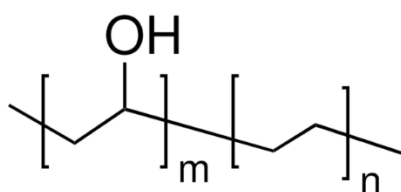
Figure 5.8 Chemical structure of poly(vinyl alcohol-co-ethylene) (EVOH)

In this section the feasibility of all aqueous phase inversion process was evaluated to obtain membranes made of EVOH for the use as separator for LIBs. The physical - chemical characterization was performed through infrared spectroscopy (FT-IR),

thermogravimetric analysis (TGA), differential scanning calorimetry (DSC), solvent uptake measurements, Gurley porosimetry and scanning electron microscopy (SEM). Electrochemical behaviour of cells containing EVOH separator were evaluated through cyclic voltammetries (CV), potentiostatic electrochemical impedance spectroscopy (PEIS) and galvanostatic charge and discharge cycles (GCD).

The materials for preparing the separators have been the following: poly(vinyl alcohol-*co*-ethylene) (EVOH, Sigma Aldrich, 32% molar content of ethylene), Chitosan (Sigma Aldrich, from shrimp shells practical grade, ≥ 75% deacetylated), acetic acid (Carlo Erba, RPE ≥ 99.5%),ethanol (Sigma Aldrich, absolute, ≥99.8 %), 2-propanol (Sigma Aldrich, ≥99.9 %HPLC) polyethylene glycol dimethyl ether 500 (PEGDME 500, Fluka, for synthesis).

For phase inversion process, the polymer solutions were roll coated on a Mylar® EB11 polyester film (25 µm thickness, Tekra) using a coater MC-20 (Mini coater, Hohsen).

Electrochemical Swagelok and BOLA cells with two and three electrodes have been assembled in a glovebox (Mbraun Labmaster SP) in inert argon atmosphere ($O_2 < 0.1$ ppm and $H_2O < 0.1$ ppm) using stainless steel (Swagelok, Swagelok Company) and PTFE Bola cells (Bohlender GmbH) with EVOH and Celgard® 2325 (25 µm Trilayer Microporous Membrane (PP/PE/PP)) membranes which were pre-dried and deaerated in an oven (B-585 Kugelrohr, BÜCHI) at 60 °C under vacuum for 16 h. For lithium symmetrical cell, lithium metal ribbon (Sigma Aldrich, 0.75 mm thick, 99,9%) was used as counter and working electrode while lithium iron phosphate (LFP, NEI Corporation, Active Material Loading: 7.3 mg cm^{-2}) was chosen as cathode for full cells and for LFP symmetric cells. For lamination test, LFP and graphite (NEI Corporation, 6.5 mg cm^{-2})

were the electrodes used to create the composite. Lithium metal was used as well as reference electrode.

The electrochemical tests have been performed with using PTFE BOLA cells connected to BioLogic VSP potentiostat/galvanostat. Potentiostatic electrochemical impedance spectroscopy (PEIS), experiments have been acquired in frequency range 200 kHz - 100 mHz, with a 10 mV perturbation amplitude around OCV, recording 20 points per decade, and using stainless steel as counter and working electrodes.

Impedance spectra to calculate MacMullin number have been fitted using EC-Lab software using linear interpolation of the first 10 points at the higher frequencies, in two electrodes mode. The intercept with the X axis represents the resistance of the membrane together with electrolyte. To get the resistivity, the resistance value has been multiplied by the area and divided by the thickness of the membrane. Lastly to get rid of the electrolyte contribution, and obtain the MacMullin number, the resistivity value was divided by the resistivity of the electrolyte.

SEM images were collected using Leica Cambridge Stereoscan 360 microscope with an accelerating voltage of 20 kV. Thermogravimetric analysis was carried out with a Q50 TA Instrument, with a heating rate of 10 °C min^{-1}, under Argon atmosphere from RT up to 600°C. Differential scanning calorimetry was carried out using a DSC Q100 TA Instrument calorimeter. Samples were subjected to three heating scans from -90 to 200 °C with a heating ramp of 10 °C min^{-1}.

To verify the electrochemical stability window, CVs have been performed after 4 hours at OCV to let the system equilibrates and the electrolytes permeate the separator. An AC PTFE electrode like those used as CE in Chapter 4.5 was used as WE in three-

electrode configuration cell, with lithium as CE and RE, and 25 cycles were performed at 20 mV s^{-1}.

GCD cycles were carried out, in two-electrode mode for lithium symmetrical cells, with the working and counter electrodes made of lithium metal electrodes, applying 10 cycles at 0.125 mA cm^{-2}, 10 cycles at 0.250 mA cm^{-2}, 100 cycles at 0.500 mA cm^{-2}, and then again at 0.125 mA cm^{-2} to verify the resistance of the EVOH separator to lithium dendrites.

For LFP symmetrical cell, GCD cycles were carried out in three-electrode mode, with the working and counter electrodes made of LFP, performing 3 initial cycles at C/10 for conditioning the materials and then prolonged cycles at C/2, to verify the stability of the cells at different current densities and prolonged cycling.

5.4.1 EVOH/chitosan separator preparation

EVOH is primarily soluble in DMSO and low molecular weight alcohols. Notably, it has been observed that EVOH dissolves at temperatures above approximately 65°C in a 70/30% v/v 2-propanol/water solution (commonly known as rubbing alcohol). These solutions remain stable for several hours at room temperature before the EVOH begins to precipitate [187]. Solutions of EVOH in 2-propanol/water, with concentrations up to 15% w/v, were prepared by heating the required amounts of polymer and solvent to 80°C. Complete dissolution of the polymer generally occurred within 3 hours under these conditions. However, once immersed in the coagulation bath, the deposited membrane scattered immediately. This problem was related to the low viscosity of the solution, despite the high polymer concentration, and increasing the EVOH concentration was leading to longer dissolution times. In order to increase viscosity,

we decided to use of a polymer mixture for the solution that will perform the phase inversion.

Chitosan was selected as polymer to form a blend with EVOH. The reason behind the choice of chitosan was multiple. Chitosan not only form jelly like solution when solubilized, but forms flexible films, too. In addition, it increases the renewable content in the final membrane and, as reported in literature, EVOH biodegradation improves when forms blend with an increased content of cellulose derivatives or polypropylene carbonate [186,188,189]. To solubilize chitosan, 2-propanol represented an unsuitable solvent even in mixture with slightly acidic water, and therefore water/acetic acid 1:1 w/w% was identified as the new appropriate solution to dissolve both chitosan and EVOH.

EVOH/chitosan membrane has been prepared using EVOH and chitosan in 90:10 %wt. respectively, with a 13 % m/v concentration of total dispersed polymers in water/acetic acid solution. As a late effort to improve flexibility, polyethylene glycol dimethyl ether (PEGDME) was introduced in 10 %wt. as a plasticizer, after complete dissolution of both chitosan and EVOH polymers. Initially, chitosan was added and left under stirring at RT in the water/acetic acid solution, until complete dissolution, usually occurring within 1 hour. Then, EVOH polymer has been added to the solution and heated up to 80°C under stirring. After complete dissolution of EVOH, the viscous solution was poured over a Mylar film, and roll coated with the mini coater to obtain a uniform polymer deposition. The bar was set at a height of 175 μm. A lower height delivers polymer films very thin and flexible, that might be difficult to be detached once dried, while a higher height produces thicker membranes that detaches easily, with the expense of being too brittle.

The phase inversion was then carried out on the EVOH/chitosan polymeric mixture deposited on the substrate by immerging in a coagulation bath composed by RT de-ionized water and water/ethanol in 8:2 %wt., over a vibrating plate that could facilitate the solvent extraction,and with different immersion times (10 and 2 minutes) to analyse through SEM images the effect of antisolvent composition and immersion times on membranes morphology and thicknesses.

EVOH/chitosan membranes were dried in oven at 60 °C for 2 hours to let the antisolvent evaporate and peeled off from Mylar substrate. Two membranes obtained from the two different antisolvent solutions are shown in Figure 5.9.

Disks with an area of 0.785 cm^2 have been punched out of the membrane and dried under vacuum at 60 °C for 16 hours prior to physical-chemical and electrochemical characterization.

a   b
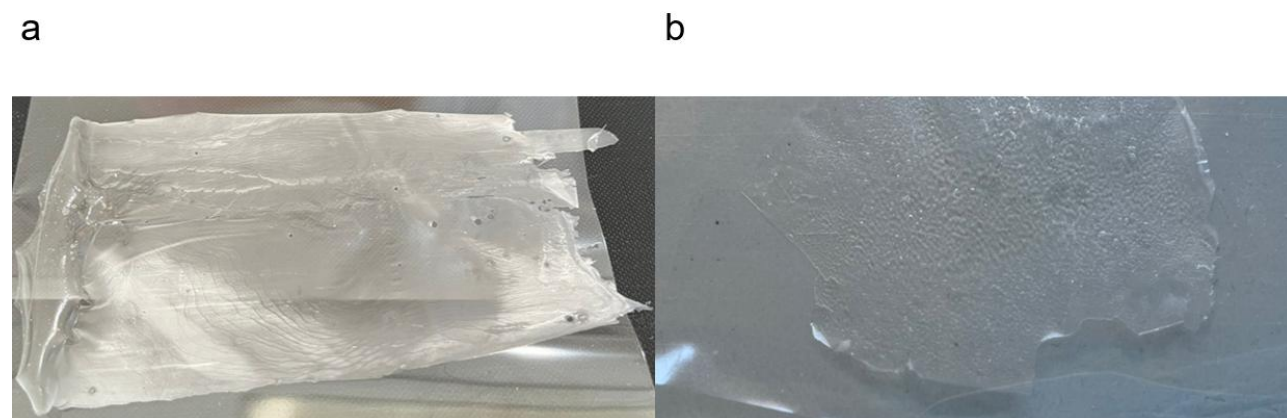
Figure 5.9 EVOH/chitosan separator obtained from phase inversion using (a) water coagulation bath and (b) water/ethanol 80:20 % wt. coagulation bath

5.5 EVOH/chitosan membrane characterization

SEM images of the membranes inverted in water and water/ethanol for different times are in Figure 5.10. It could be seen that both time and antisolvent composition play a key role for the membrane morphology and porosity. As could be seen in Figure 5.10a, after 10 minutes of immersion, the obtained membranes appear completely different. The one immersed in water presents at a non-homogeneous surface, alternating flat and smooth regions to others where pores with a diameter of about 20 μm could be identified. Looking more in details at the higher magnification (Figure 5.10b), a regular and diffuse homogeneous porous structure could be seen, with pore sizes around 500 - 1000 nm.

The surface irregularities come from the non-uniform phase inversion process probably due to regions in which the polymer composition might contain more of one polymer species than the other, where the solvent in which the polymer is soluble is extracted and substituted depending on the exchange rate. However, when membrane pores form rapidly upon immersion in the nonsolvent bath, the process is termed instantaneous demixing. Instead, when pore formation occurs only after a significant amount of time allowing more nonsolvent to penetrate the film it is referred to as delayed demixing. Instantaneous demixing produces membranes with a relatively porous skin layer and large pores in the sub-layer. In contrast, delayed demixing results in membranes with a denser skin layer and no macrovoids. Consequently, membranes formed through delayed demixing typically exhibit lower porosities but increased mechanical properties [190,191]. On the other hand, keeping a constant phase inversion time of 10 minutes, the membrane immersed in water/ethanol shows the complete absence of pore structure both at lower and higher magnification, as visible in Figure 5.10c. Eventually we couldn't reach 15000 X because this sample was starting to

electrostatically charge and being burnt by the electron beam; as could be seen in Figure 5.10d, the highest recorded magnification was at 5000 X. The complete absence of porosity on this sample is due to the demixing and miscibility between ethanol and water of the antisolvent bath. Due to the presence of ethanol in the antisolvent bath, its interaction with the polymer solution prevents entering the thermodynamic metastable region between solvent, nonsolvent, and polymer composition; as a result, the polymer chains can rearrange themselves and form a smooth surface without generating pores [190,191]. Since the absence of any porous structure of this membrane, the water/ethanol mixture for the coagulation bath was discarded and only water was used as antisolvent.

To verify the effect of time upon morphology and porosity, SEM images of membrane immersed for 2 minutes were recorded. In accordance with the above observations, it could be seen that at lower magnification Figure 5.10e, the surface of membrane appears more uniform and without the presence of macroscopic pores. Looking at 15000 X, the surface exhibits a microporous structure, although less evident compared to the sample immersed for 10 minutes, containing pores with a diameter around 1 μm and smaller pores of hundreds of nanometres.
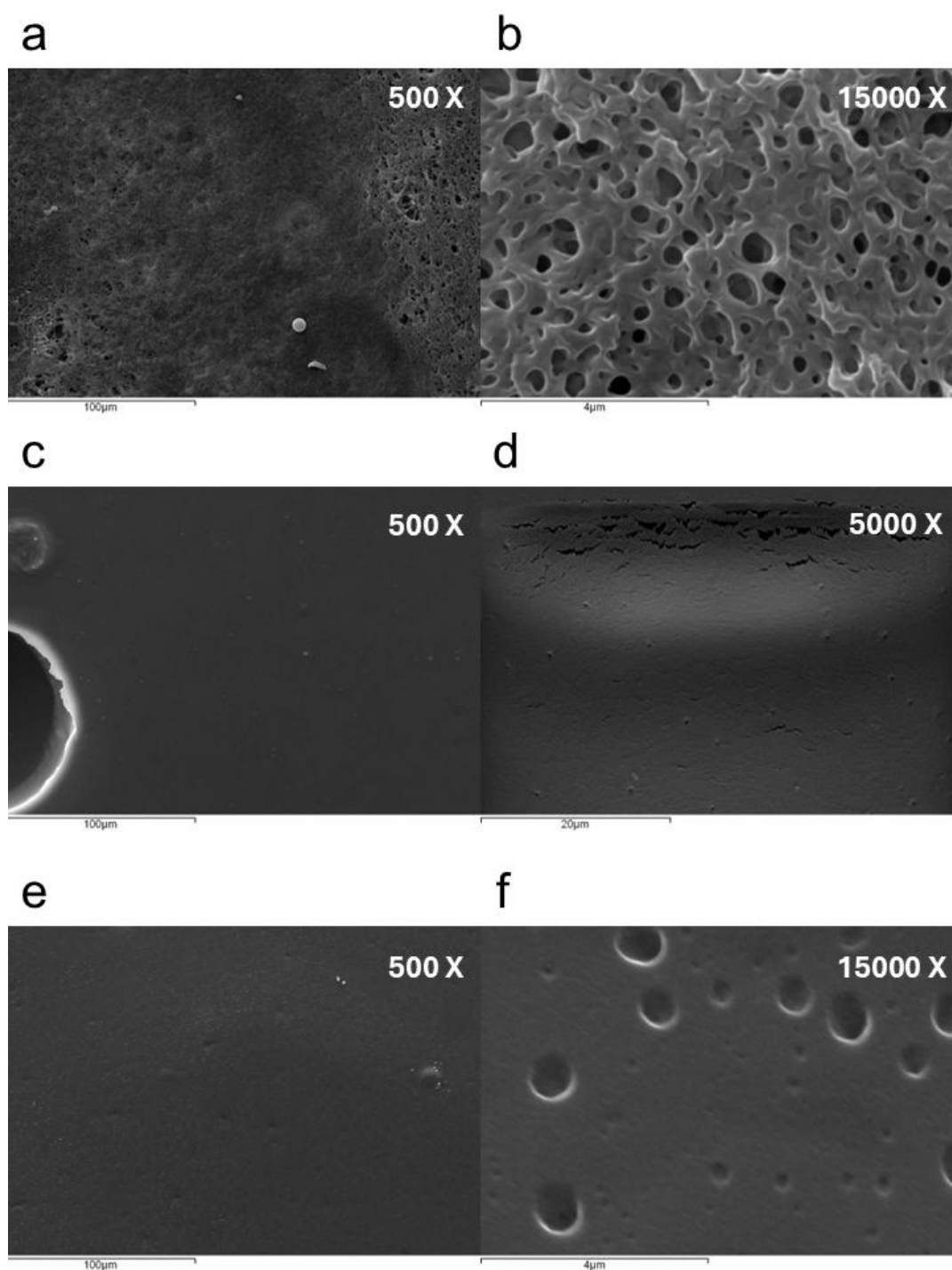
94

Figure 5.10 SEM images of EVOH/Chitosan membranes immersed in the coagulation bath for 10 minutes in water (a, b) or water/ethanol 8:2 % wt. (c, d) and for 2 minutes in water (e, f)

However, given that we wanted to use this membrane as separator for LIBs, increased porosity compared to commercial extruded membrane, could be beneficial for cell

working and for this reason following this preliminary screening, EVOH/chitosan membrane immersed in water for 10 minutes was further investigated.

SEM images have been recorded also for EVOH/chitosan membranes immersed in water and water/ethanol for 10 minutes to appreciate the morphological difference with pristine samples (Figure 5.10) and membranes after lamination between LFP and graphite electrodes and subsequent de-lamination, as reported in Figure 5.11.

Separator samples have been cut with an area of 1.5 cm^2 while the electrodes, LFP and graphite, were of 1 cm^2. The components have been precisely aligned and laminated at 1500 psi cm^2 at 60 and 80 °C to verify if at temperatures above glass transition (T_g) the membrane surface would undergone through significant changes. The assembly have been delaminated after 30 minutes of soaking in isopropanol as standard industrial procedure. As visible in Figure 5.11a, c, the de-laminated samples obtained from phase inversion in water show a comparable porosity and pore size as the membrane visible in figure 5.10a, however after the lamination process the morphology seems different to the pristine sample both at 60 °C and 80 °C. This may be since, following delamination, the first membrane layer is removed, thus exposing the internal structure of the separator. The internal structure of the separator has a higher porosity, generated by solvent extraction during phase inversion; whereas the surface, due to the presence of the antisolvent which makes the solubility regime of the polymer blend thermodynamically unstable, tends to form a more homogeneous and cohesive structure. Since at 80 °C the polymer is above T_g, it could be more sensitive to high pressures and be more easily malleable, hence at 60 °C, below T_g, these high pressures might lead to cracks or breaking point, as visible in Figure 5.11a [192].

This difference is not visible in the laminated samples obtained from soaking in water/ethanol coagulation bath, Figures 5.11c, d. The morphology of the laminated membrane both at 60 and 80 °C shows no evident differences and as expected, there could be seen here as well the absence of any kind of porous structure.
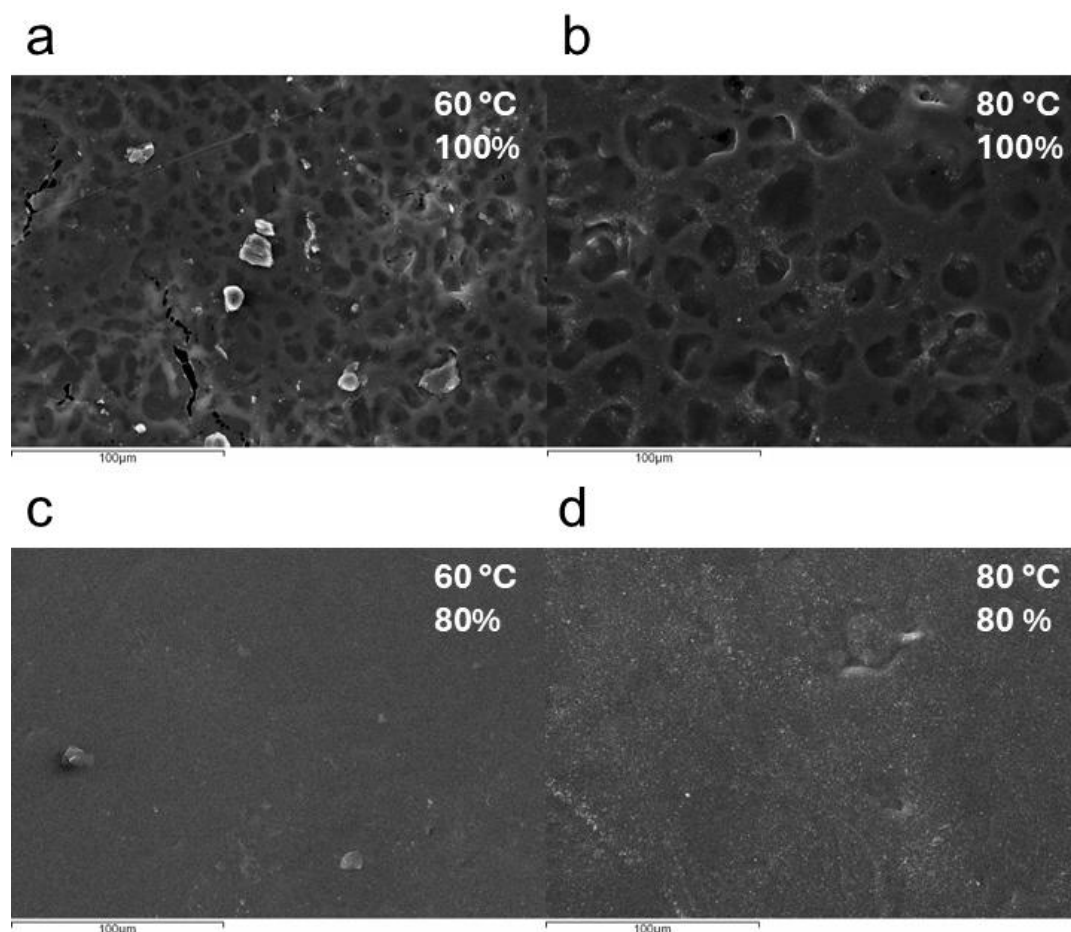
Figure 5.11 SEM images of EVOH/chitosan membranes immersed in the coagulation bath for 10 minutes in water (a, b) or water/ethanol 8:2 % wt. (c, d) and laminated at 60 °C (a, c) and 80 °C (b, d)

Despite soaking in isopropanol and washing, some pieces of electrodes are visible on the surface of membranes.

TGA curves for the chitosan, EVOH and EVOH/chitosan are shown in Figure 5.12. Although all samples were dried, chitosan demonstrated a low amount of residual

water, as it could be seen from the low mass decrease below 150°C, compared to EVOH and the copolymer. The blend with EVOH and chitosan shows a degradation that is the sum of both the components: the water content compared to bare chitosan is negligible and the degradation starts a little bit anticipated compared to EVOH but thanks to chitosan moieties the slope of the main weight loss is less pronounced. Above 450 °C, the recorded profiles of the blend and the pure chitosan are comparable because all the EVOH fraction degraded.
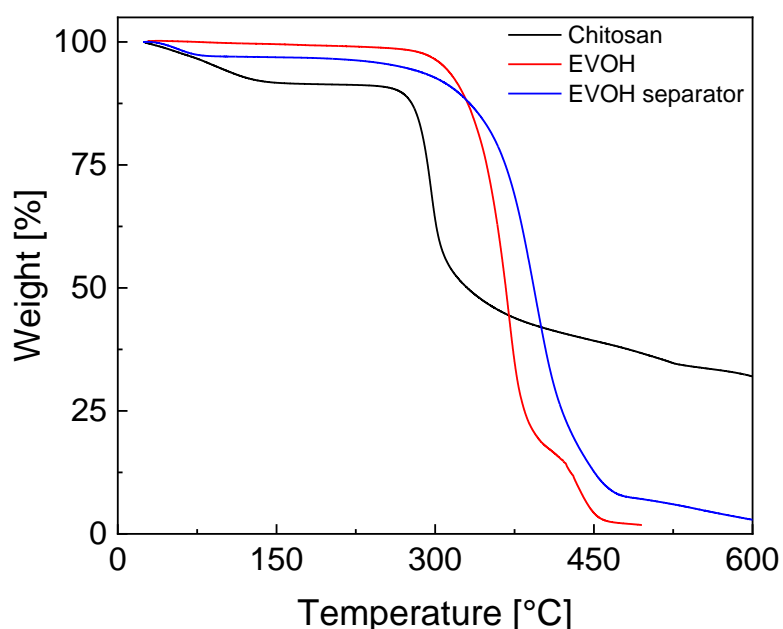
Figure 5.12 TGA curves of chitosan (black line), EVOH (red line) and EVOH/chitosan (blue line) membranes in Ar atmosphere, 10 °C min⁻¹ ramp up to 600 °C

DSC curves for EVOH/chitosan membranes are plotted in Figure 5.13. The temperature range was selected from -90 °C to 200 °C, where the maximum temperature was selected to limit possible degradation, by considering that chitosan thermal degradation starts around 220 °C [193]. During the first heat scan (black line) the

T_g is not easily identifiable because of the broad endothermic peak centred at 90 °C that is due to the evaporation of the residual water adsorbed by the aminic groups of chitosan [194].

At 170 °C, another endothermic peak, which is associated to the melting of crystalline domains of the EVOH in the polymer blend, could be seen. During the cooling ramp of the 1st scan, the corresponding endothermic peak due to the formation of crystalline domains of EVOH occurs at 145 °C. It could be noted that the area of the crystallization is considerable higher than the area of the melting peak during the first scan. This indicates that the EVOH polymer is mostly an amorphous polymer [195,196].
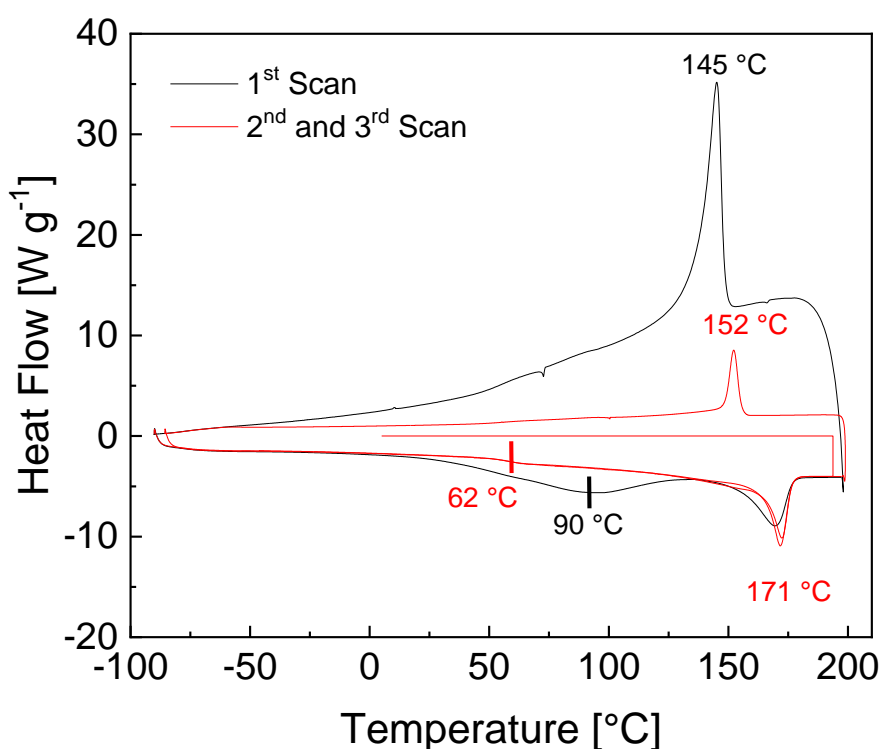
Figure 5.13 DSC curves of EVOH/chitosan membrane, performed in N₂ atmosphere, 10 °C min⁻¹ from -90 °C to 200 °C

During the second and third scans, the shape of the crystallization and melting appear more symmetrical and with the same heating flow. It could be seen clearly the T_g at 62 °C and no subsequent water loss.

Electrolyte uptake and porosity measurements represents important information for the characterization of membranes, especially in the context of applications like batteries, and other EESS. These parameters provide essential insights into the membrane's performance, particularly its ability to transport ions and maintain stability during operation.

The electrolyte wetting behaviour of the separators were observed as displayed in Figure 5.14 following the procedure describe in literature [197,198]. Two separator disks of have been soaked for 24 hours in two different media, LP30 electrolyte and water, and closed inside a coin cell case. After 24 hours the coin cells were opened, and the disks were gently dried with paper tissue to remove the excess of solvent on the surface preserving the absorbed electrolyte and weighted to measure the weight difference between dry and wet membranes. These tests have been performed in quintuplicate to account also for average error. The results are listed in Table 5.3. Uptakes were calculated according to the formula (13) [199]:

$$Electrolyte\ uptake\ (\%): \frac{W_{wet} - W_{dry}}{W_{dry}}\% \tag{13}$$

Membrane \ Solvent	LP 30	Water
Celgard	96 ± 5 %	24 ± 9 %
EVOH/Chitosan	580 ± 40 %	521 ± 72 %

Table 5.3 Electrolyte uptake of Celgard and EVOH/chitosan membranes, determined after 24 hours of soaking

Compared to Celgard, EVOH/Chitosan membrane absorption is significantly greater. This is due to the increased porous structure of the membrane obtained through phase inversion.
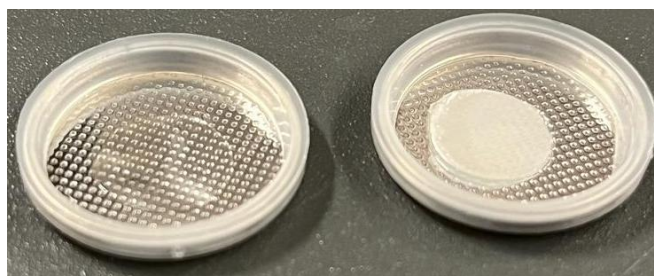
Figure 5.14 Disks of EVOH/Chitosan (left) and Celgard (right) after 24 hours of soaking

Higher uptakes from the separator means that the separator could act as a reservoir for the electroactive species, providing ions in case of locally depletion on the electrode surfaces and preventing mass transport issue that could ultimately lead to increased overpotentials of the redox processes [200,201]. However, the higher the uptake, the more electrolyte is required to fill and soak completely the system, leading to increased costs and lowered the specific energy of the device, because of the highest amount of electrolyte required.

As an example, taken into account a cell composed of commercial tapes of LFP and graphite as cathodic and anodic material respectively, the variation of specific energy between a cell that features Celgard 2300 as separator and another with EVOH/chitosan membrane could be estimated as follows:

LFP		Graphite
	Mass Loading	
7.3	mg/cm^2	6.5
	Areal capacity	
1.24	mAh/cm^2	2.4

	Specific capacity [mAh/g]	
170		372
	1.1 N/P Ratio considering 1cm^2 of area of LFP [mAh]	
1.24		1.36
	Active mass [mg]	
7.30		3.66
	Total coating mass [mg]	
8.30		4.00
	Area [cm^2]	
1		0.56
	Current collector	
Aluminium		Copper
	Density [g/cm^3]	
2.7		8.96
	Thickness [cm]	
0.0016		0.001
	Collector weight [mg]	
4.32		5.02
	Partial [mg]	
12.62		9.02
	LFP + Graphite weight [mg]	
21.64		21.64
Celgard 2300	Separator weight for 1 cm^2	EVOH/Chitosan
1.8	[mg]	0.92
	Uptake [w/w %]	
90		580
	Total weight of membrane + electrolyte [mg]	
3.42		6.25
	Cell total weight	
Celgard 2300		EVOH/Chitosan
25.06	mg	27.89
0.000025	[kg]	0.000028

	Nominal Voltage (LFP//Graphite cell) [V]	
3.2		3.2
	Capacity [Ah]	
0.0012		0.0012
	Energy [Wh]	
0.0040		0.0040
	Specific energy [Wh/kg]	
159.62		143.42
	Difference [%]	
		-10.2

To minimize the specific energy difference between polyolephinic and EVOH/chitosan membranes, that in our case was calculate to be around ~10%; the membrane should possess an uptake of electrolyte lower than ~270%. Still, even if 270% of electrolyte uptake represents the break – even point of the energy density comparison, higher quantities of electrolytes are involved for the cell assembly. By further reducing the uptake value, higher energy density as well as lower costs can be obtained together.

Porosity measurements have been performed with the standard Gurley porosimeter. To determine porosity, Gurley porosimeter measures the amount of air that is flowing across the membrane, and the Gurley number (GN) is the time in seconds it takes for 100 cc of air to pass through 1 square inches of membrane when a constant pressure of 1.213 kPa is applied. The porosimeter is schematized in Figure 5.15. The lower is the value the more porous is the membrane. Results are reported in Table 5.4, where the GN is given in Gu s, adjusted considering 100 cc of air flowing across samples of 1.0 square inch of material.

	GN [Gu s]
Celgard	304.7

EVOH/Chitosan (inverted in water/ethanol)	1162.5
EVOH/Chitosan (inverted in water)	11.8

Table 5.4 Gurley porosity values of Celgard and EVOH/chitosan membranes

In accordance with the observation of the SEM images, the different membranes of EVOH/chitosan obtained using a coagulation bath of water or water/ethanol exhibit different porosity values. The highly porous membrane obtained from immersion in water exhibit interestingly good porosity values. Better porosity could contribute to lower internal resistances [202]. On the other hand, EVOH/chitosan membrane obtained from water/ethanol 8:2 % wt. that appeared like a smooth and plain film, exhibits GN values 100 times higher and three times higher than the EVOH/chitosan membrane obtained from water bath and Celgard, respectively, indicating that its use as membrane for LIBs is not suitable.
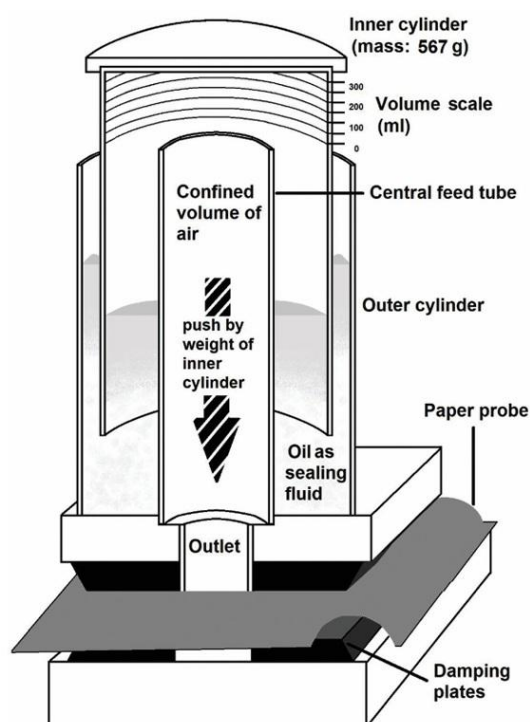
Figure 5.15 Scheme of Gurley porosimeter as an experimental method to inspect the air permeability of membranes [203]

The contribution of the membrane to cell resistance was evaluated using the dimensionless MacMullin parameter (N_M), determined through EIS measurements as outlined in the experimental section [204]. Figure 5.16 displays the EIS spectra of EVOH/chitosan separators, while Table 5.5 lists the N_M values for pristine Celgard and modified membranes soaked in LP30 electrolytes.

Separator	Area [cm^2]	Thickness [cm]	Resistivity ρ [Ω cm]	LP30 resistivity ρ_0 [Ω cm]	N_M ρ / ρ_0
Celgard		2.4×10^{-3}	1400		17
	0.785			82.5	
EVOH/chitosan		1.2×10^{-3}	612 - 1240		7

Table 5.5 Resistivity of the electrolyte-soaked separators (ρ), LP30 resistivity (ρ_0) and MacMullin number (N_M)

EVOH/chitosan separator shows N_M values considerably lower than Celgard membranes. Presumably, lower N_M is due to increased porosity and pore size that facilitates the movement of lithium ions back and forth.

Figure 5.16 (a) EIS spectrum (20 points/decade) of the stainless-steel symmetrical cell with EVOH/Chitosan separator soaked in LP30, with the magnification (b) and fitting of the high frequency region (200 - 50 kHz)

Given that N_M values are divided by the electrolyte resistivity it should be relatively independent of the electrolyte. However less viscous electrolytes enhance wettability which seemingly reduces the impact of separator tortuosity, as N_M is also determined by the ratio of the squared tortuosity to the porosity [204].
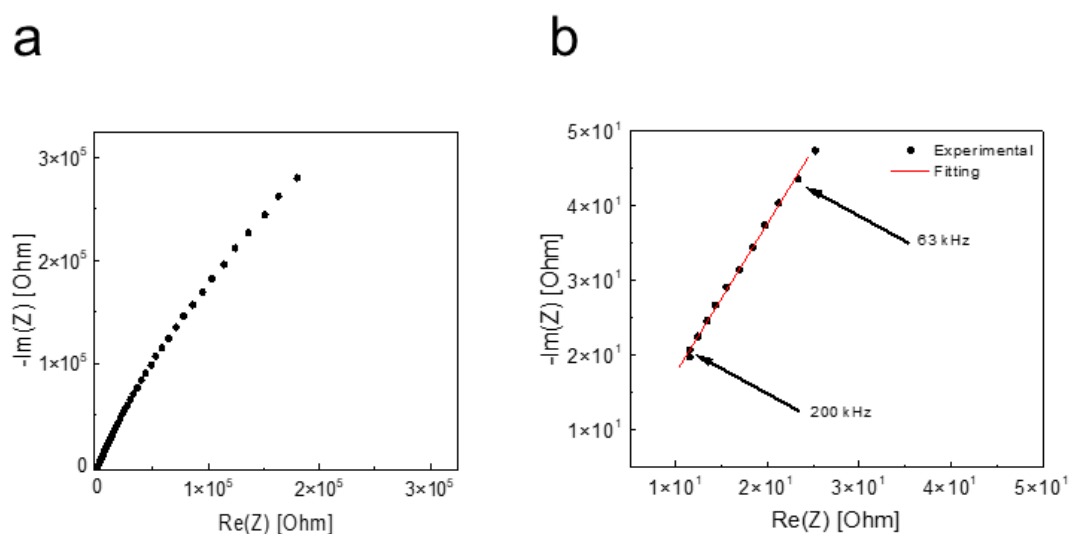
Cyclic voltammetry was employed to investigate the electrochemical stability window of the EVOH/chitosan and Celgard separator. Figure 5.17 presents the CVs recorded at a scan rate of 1 mV s^{-1} over the voltage range of 0.1 - 5 V in LP30 electrolyte, by opening the potential values, every 3 consecutive cycles, to better evaluate the phenomena that could occur with the use of the membranes. The reduction process begins approximately at 1.5 V in all systems, with the observed reduction current likely corresponding to the decomposition of the electrolyte [205,206]. However, the reduction processes seem to begin a bit earlier and with higher currents, with the EVOH/chitosan membrane, it can reasonably be attributed to interactions between -OH groups contained on the surface, the electrolyte and the stainless-steel surface of the collectors. These interactions might explain also the difference of the capacitive current values between the cycles towards low potential values and the high potential values region. In oxidation no peaks could be observed, although it could be seen the oxidation of LP30 electrolyte at potential values starting above 4.8 V vs Li. Upon cycling, no increase of the current density values could be observed for both the samples.
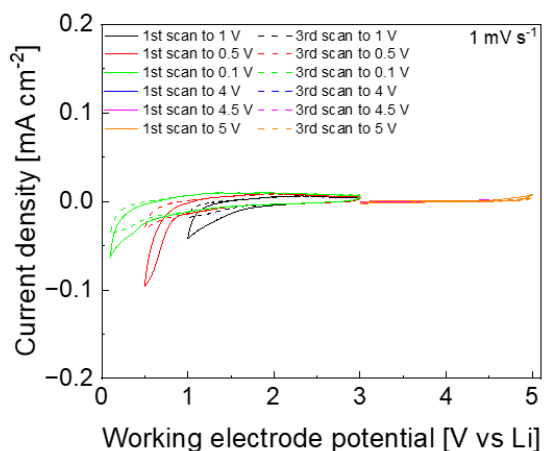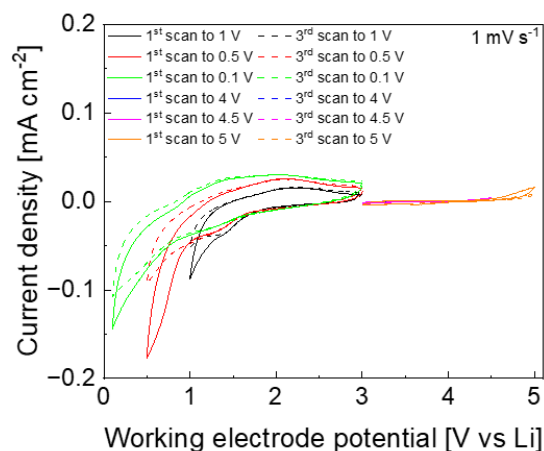
Figure 5.17 (a) CVs at 20 mV s⁻¹ of Celgard and (b) EVOH/chitosan separator, recorded recorded in three electrodes mode using stainless steel and lithium as working and counter and reference electrodes respectively in LP30 electrolyte with a scanning rate of 1 mVs⁻¹.

Figure 5.18 illustrates the GCD cycles of lithium symmetric cells in LP30. The cell containing Celgard separator, Figure 5.18a, demonstrates great stability at all the current densities with overpotentials of lithium plating and stripping below 100 mV even at 0.5 mA cm⁻². In contrast, looking at the profiles obtained with EVOH/chitosan membranes, it appears that lithium plating and stripping is more resistive both at 0.125 and 0.250 mA cm⁻². The higher resistivity upon deposition and stripping might arise probably from the lower flexibility of this membrane, compared to Celgard, that results in a worst contact with the electrodes. In addition, despite the increased porous structure of EVOH/chitosan membranes, increased overvoltages upon lithium plating/stripping may be caused by an insufficient pore connectivity that leads to uneven lithium concentration gradient across the separator, eventually accelerating localized lithium growth [207].

After 30 hours reaching the current density of 0.500 mA cm^{-2} the cell underwent rapidly, towards a series of short circuits due to lithium dendrites penetration in the separator. Lower N_M for EVOH/chitosan separator is mainly due to the superior porosity, the presence of pores with a diameter of several micrometres allows for a lower endurance upon dendrite perforation.

a

b
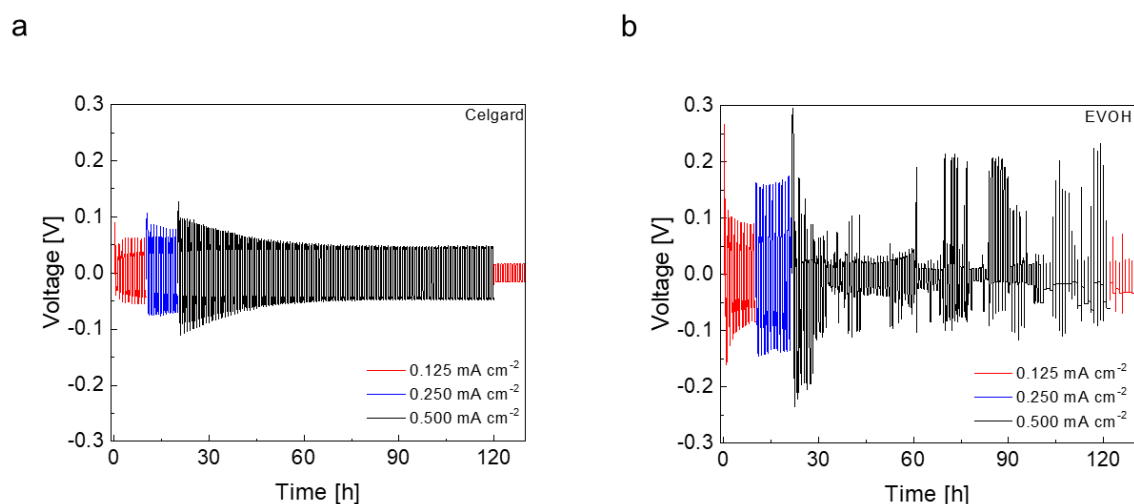
Figure 5.18 Deposition and stripping cycles of lithium symmetric cells in LP30 electrolyte with (a) Celgard and (b) EVOH/chitosan separator at 0.125 mA cm^{-2} (red), 0.250 mA cm^{-2} (blue) and 0.500 mA cm^{-2} (black).

The deposition/stripping overpotential profile of a single electrode typically reveals an initial deposition process characterized by a peak, which arises due to the high kinetic barrier for lithium nucleation on the smooth metal surface with its native passivation layer. By Ohm's law, the overpotential depends on the applied current, the higher the current flowing through lithium electrode, the higher the overpotential for the processes will result. In subsequent cycles, the intensity of this peak diminishes, reflecting the reduced resistance associated with the lithium that sustained deposition/stripping cycles. Following the nucleation peak, the overpotential decreases, indicating more favourable lithium deposition as the incomplete passivation layer exposes fresh lithium,

encouraging preferential deposition on these sites. On the other hand, the initial stripping process primarily occurs on the previously deposited lithium, which features a higher surface area and/or an underdeveloped SEI. This partial redissolution of lithium contributes to the erosion of dendrites and the formation of electrically isolated lithium [205].

When all freshly deposited lithium is either fully dissolved or physically disconnected from the electrode, the stripping process is forced to move to the remaining older lithium, resulting in a progressive increase in overpotential. This growth reflects the increasing difficulty in stripping lithium, with the peak overpotential corresponding to the bulk lithium [205].

All these phenomena collectively define the potential profile of a lithium electrode during deposition/stripping cycles. In a two-electrode cell, the voltage profile reflects the combined contributions of the simultaneous processes occurring at both the working and counter electrodes. In Figure 5.19 the deposition/stripping of selected cycles for lithium symmetrical cells with both separator samples are reported. The simultaneous occurrence of the nucleation peak current on the counter electrode and the stripping from the smooth metal surface with its native passivation layer on the working electrode results in a voltage profile exhibiting a distinctive double-peak shape, especially noticeable at higher current densities [205]. During deposition, the nucleation peak becomes prominent due to the varying dependency of deposition overpotentials on the current density, as modelled by Barton et al. in 1962 [208]. Although the overpotentials are higher with the cell featuring EVOH/chitosan membrane, the double shaped peak is visible for both the systems. Moreover, a high stripping current density results in less uniform stripping, accelerating the removal of older lithium deposits

(second peak). Prolonged cycling at lower current densities promotes the formation of a porous and low-density surface.

However, at 0.5 mA cm^{-2} the EVOH/chitosan membrane were not able to withstand the dendrite evolution and growth, and underwent to short circuit, as testified by the presence of spikes and the potential fall close to 0 V. After 100 cycles, as could be seen in the cell with Celgard separator, the overpotential stabilizes as the deposition and stripping processes are confined to the porous regions of the electrodes. A smooth and flat lithium surface means uniform lithium deposition, where only the freshly deposited lithium is stripped. Under these conditions, the overvoltage remains constant, as the stripping occurs on a surface with uniform resistance properties.
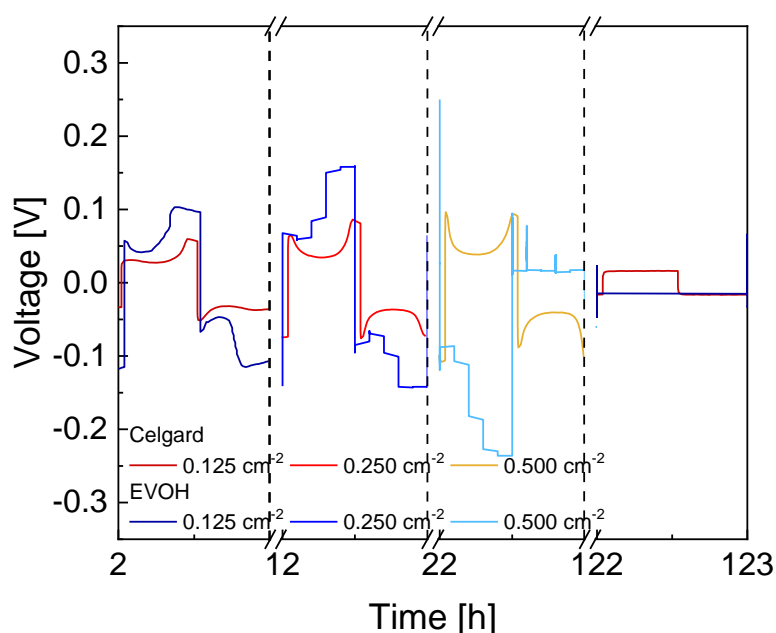
Figure 5.19 Selected overvoltage profiles of lithium deposition/stripping of lithium symmetric cells in LP30 with Celgard (shades of red) and EVOH/celgard (shades of blue) at 0.125 mA cm^{-2}, 0.250 mA cm^{-2} and 0.500 mA cm^{-2}.

To overcome dendrite formation issues, GCD of symmetrical cells with LFP electrodes have been performed. Prior to cycling, since cells have been assembled in three-electrode mode, one LFP electrodes have been completely delithiated, using as CE the lithium metal electrode located on the reference side and applying a C/10 galvanostatic charge. Once the LFP was completely delithiated (FP) the cell was restored with the FP as CE, the pristine LFP as WE and Li metal as RE. The tests were carried out by constant current charge and discharge between 2.5 and 4.0 V vs Li. Three initial cycles at C/10 were performed followed by prolonged cycles at C/2. Figure 5.20 exhibit the charge/discharge profiles of LFP electrode, having an active mass loading of 6.5 mg cm^{-2}, at a rate of C/2. The electrodes deliver a discharge capacity of ~150 mAh g^{-1} with both separators, which is a good value in agreement with practical capacities reported in literature [209]. The cell with EVOH/chitosan separator shows a slightly higher increased overvoltage, ~ 0.1 V potential between charge and discharge plateaux, with respect to the cell with Celgard separator. However, the specific discharge capacity of the LFP with EVOH/chitosan separator, is 150 mAh g^{-1}, almost equal and comparable to the one obtained with the commercial Celgard membrane, demonstrating the good compatibility of this membrane with an insertion electrode compared to lithium metal electrode.
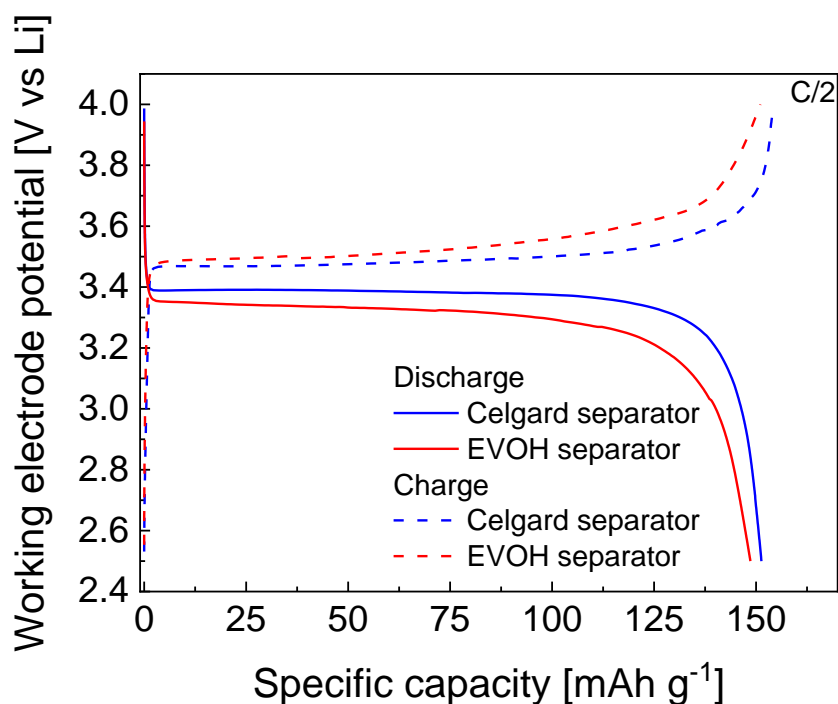
Figure 5.20 Cycle charge/discharge profile of LiFePO₄ electrodes in LFP//LP symmetrical cell, at a c-rate of C/2 in LP30 electrolyte with Celgard (blue lines) and EVOH/Chitosan (red lines) separators

The capacity retention and coulombic efficiency of the cells with Celgard and EVOH/chitosan membranes are shown in Figure 5.21. The cell with Celgard separator, after showing lower values of specific capacity especially at C/10 and at the initial C/2 cycles, progressively improved upon reaching values around 120 mAh g^{-1} after 120 cycles. The cell with EVOH/chitosan membrane displays an initially low specific capacity, probably due to contact and wetting issues between the electrodes and separator. However, the cell progressively regained capacity, and after 45 cycles stabilized to values around 145 mAh g^{-1}. However, after 100 cycles the cell with EVOH/chitosan separator begun to lose capacity, still maintaining above values observed with Celgard, because of the unbalancing between the electrodes.

Coulombic efficiency values, have been particularly good and kept constant close to 100% since the initial cycles in the system with Celgard separator and, after the initial cycles for the cell with EVOH/chitosan membrane with values between 95 and 99%, values close to 100% were obtained.
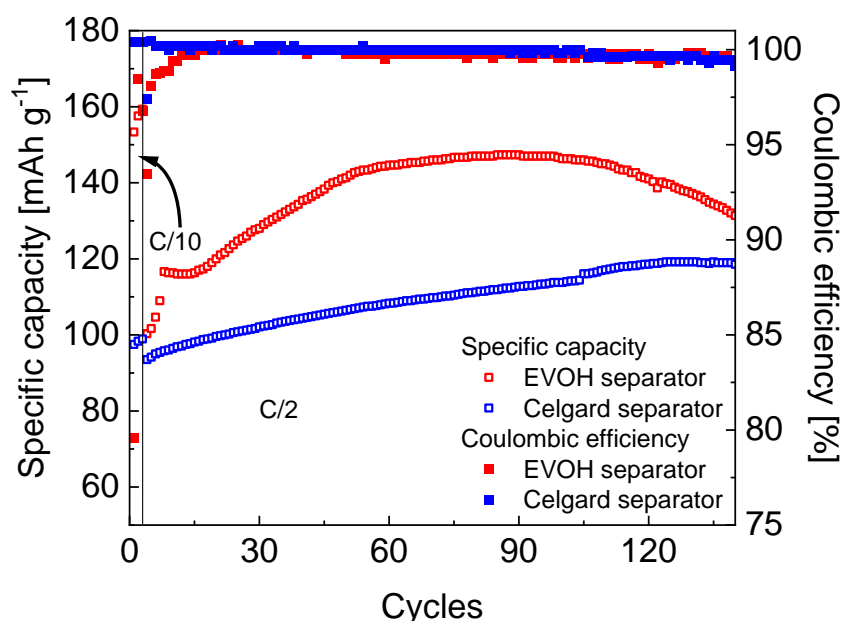
Figure 5.21 Capacity retention (void squares) and coulombic efficiency (full squares) data of LFP cells in LP30 electrolyte over testing at C/2, after three formation cycles at C/10 C-rate with EVOH/chitosan (red) and Celgard (blue) separators

Lastly, to address the brittleness issues of EVOH/chitosan membranes, which affect their ease of handling and, most importantly, their mechanical strength and resistance to dendrite penetration; it was studied the use of PEGDME as plasticizer for the EVOH/chitosan separator. It was selected PEGDME, given that its use as plasticizer for membrane and polymer electrolytes is well known and, to see if the addition was beneficial for the electrochemical stability with lithium metal anode [210,211]. The membrane was prepared following the same procedure as described previously in

Chapter 5.4.1, with the exception of the composition, that instead of 10% wt. chitosan, the same amount was replaced by the PEGDME plasticizer.

Figure 5.22 represents the deposition/stripping of lithium symmetrical cell in LP30 with EVOH/PEGDME separator at 0.125 and 0.250 mA cm^{-2}, avoiding the higher current density of 0.5 mA cm^{-2} to simply verify the stability over prolonged cycling without stressing excessively the system. From Figure 5.22, we could observe current densities with overpotentials of lithium plating and stripping below 100 mV starting from the first cycles at 0.125 mA cm^{-2}. Increasing the current density at 0.250 mA cm^{-2}, the overvoltage of plating and stripping appear slightly less resistive, below 150 mV, compared to what observed with EVOH/chitosan separator and maintains a regular trend, without showing spikes or other signs of instability. This might be due to the better contact with the electrodes, thanks to the increased flexibility of the separator. Upon prolonged cycling at 0.125 mA cm^{-2}, the cell with EVOH/PEGDME exhibit a better stability compared to what seen with the membrane without plasticizer, displaying deposition/stripping overvoltage below 100 mV.

However, the low overvoltage with a rectangular shape, occurring between 77 and 85 hours of cycling, indicate the presence of partially short-circuited regions [212]. This might arise to dendrites formation and evolution that tends to create local soft short circuits.. Nevertheless, after some cycles the cell, seems to regain stability, getting out from the short circuit condition, showing overvoltage resistances that appear to return to the initial levels.
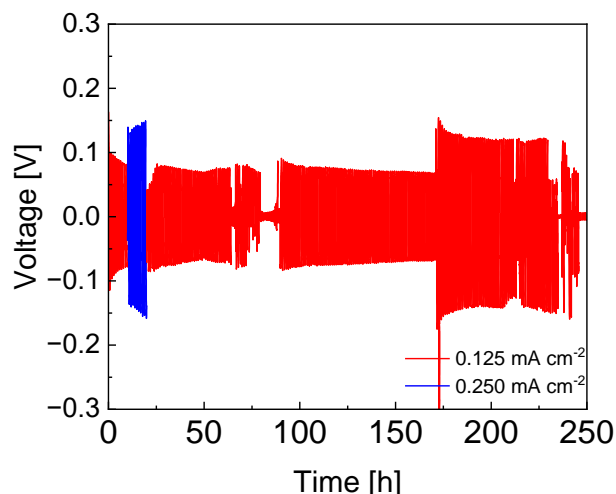
Figure 5.22 Deposition and stripping cycles of lithium symmetric cells in LP30 electrolyte with EVOH/PEGDME separator at 0.125 mA cm^{-2} (red) and 0.250 mA cm^{-2} (blue)

5.6 *PBF electrospun membranes*

During my doctoral program I had the opportunity to collaborate with the groups of Prof. Nadia Lotti (University of Bologna, Department of Civil, Chemical, Environmental, and Materials Engineering) and Prof. Andrea Dorigato, Dr. Giulia Fredi and Dr. Sofia Santi (University of Trento, Department of Department of Industrial Engineering) about the characterization of high-molecular-weight poly(butylene 2,5-furanoate) (PBF), shown in Figure 5.23, that up to now has been used for bio-medical applications. University of Trento made the electrospinning process and provided us the membranes for the electrochemical characterization to evaluate the feasibility of this polymer as separator for LIBs.

Furanic compounds represents a class of monomer that gained significant attention from both academic and industrial communities. Among the furanic compounds, 2,5-furandicarboxylic acid holds significant potential as a sustainable monomer for synthesizing polyesters, offering a green alternative to key petroleum-based thermoplastic polymers such as poly(ethylene terephthalate) (PET) and poly(butylene

terephthalate) (PBT) [213–215]. To our knowledge this is the first time this polymer has been used for battery related applications.
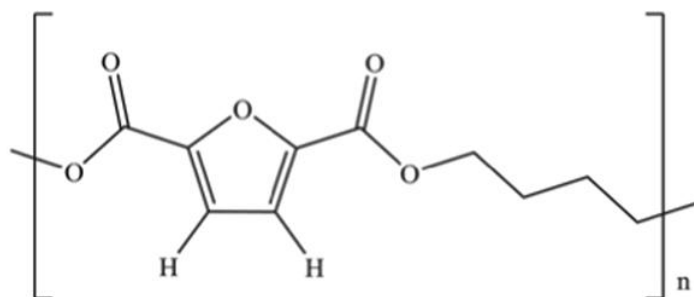
Figure 5.23 Chemical structure of poly(butylene 2,5-furanoate)

Two different electrospun mats of PBF were characterized: one pristine PBF (PBF-N), and the treated under vacuum at RT for 72 hours after electrospinning (PBF-T).

The electrospinning setup, as schematized in Figure 5.6, was confined in a poly(methylmethacrylate) (PMMA) chamber with monitored temperature and humidity. The electrostatic forces were generated by applying an electrical field using a DC voltage source of 24 kV and setting a distance of 15 cm between the nozzle tip and a flat aluminum foil, utilized as a collector. The spinning rates were regulated using a syringe pump that flows out the solution from the metallic nozzle, which had a diameter of 0.9 mm. The production of mats with a homogeneous thickness of ~ 20 µm is promoted by a sliding system that moves the syringe pump from left to right at a speed of 20 mm/s. PBF mats with good microstructural quality were obtained under the optimized processing conditions described in [215].

SEM was used to investigate the morphology differences between PBF-N and PBF-T, visible in Figure 5.24. Both samples show the typical morphology of non-wowen membranes, with randomly oriented polymer fibres, and pores with dimension of 1-3

micrometres. After thermal treatment, PBF-T fibres appear bigger and thicker as if they underwent coalescence. Nonetheless, the sample preserved the same randomly distributed porosity alongside with pore dimension that slightly increased within a diameter of five micrometres, following the treatment.
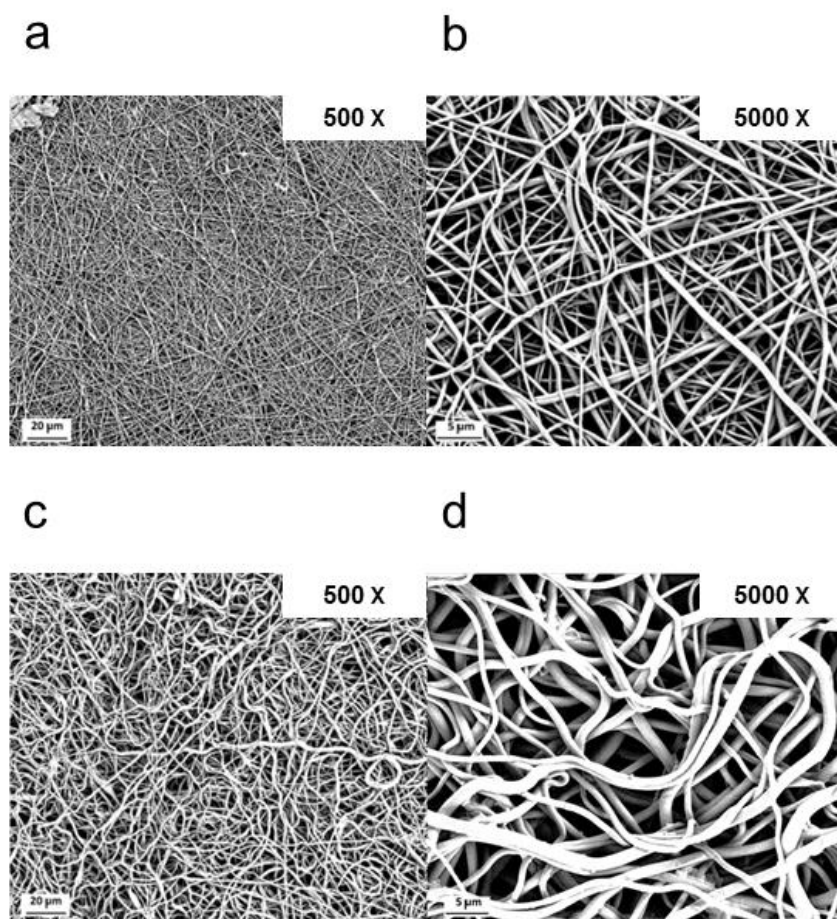
Figure 5.24 SEM images of electrospun PBF membranes before (a, b) and after heat treatment of 40 °C for 5 hours (c, d)

Subsequently, solvent uptake measurements were performed with PBF samples to evaluate the retention after 24 hours of soaking in LP30, following the same procedure described for EVOH/chitosan membranes. The electrolyte uptake results are shown in Table 5.6.

Membrane ╲ Solvent	LP 30
PBF-N	531 ± 23 %
PBF-T	658 ± 34 %

Table 5.6 Electrolyte uptake of PBF membranes, determined after 24 hours of soaking

Values of 531 ± 23 % and 658 ± 34 % respectively for treated and non-treated PBF, were obtained. These numbers are in line with the typical values reported in literature for electrospun membranes. Usually, desired values for an ideal membrane are around 150 % of uptake, in which the membrane acts as a reservoir of electrolyte, providing and compensating possibles electrolyte consumption maintaining adequate ionic conductivity [216,217].

PEIS were performed, according to same methodology and setup described for EVOH/chitosan separator, to evaluate N_M parameter. Figure 5.25 shows the EIS spectra of PBF separators and Table 5.7 displays the obtained value and the reference value of Celgard soaked with LP30 electrolyte.

Separator	Area [cm^2]	Thickness [cm]	Resistivity ρ [Ω cm]	LP30 resistivity ρ_0 [Ω cm]	N_M ρ / ρ_0
Celgard		2.4×10^{-3}	1400		17
PBF-N	0.785	2.2×10^{-3}	253.3	82.5	3
PBF-T		2.0×10^{-3}	863.5		11

Table 5.7 Resistivity of the electrolyte-soaked separators (ρ), LP30 resistivity (ρ$_0$) and MacMullin number (N$_M$)

As expected, the values obtained with PBF membranes, especially with the non-treated membrane, are lower compared to the one reported of Celgard. This lower value arises from the fact that electrospun membranes feature pores with higher diameter and a decreased tortuosity that promotes ionic mobility and lower ionic resistivity compared to nonwoven membranes.

a

b
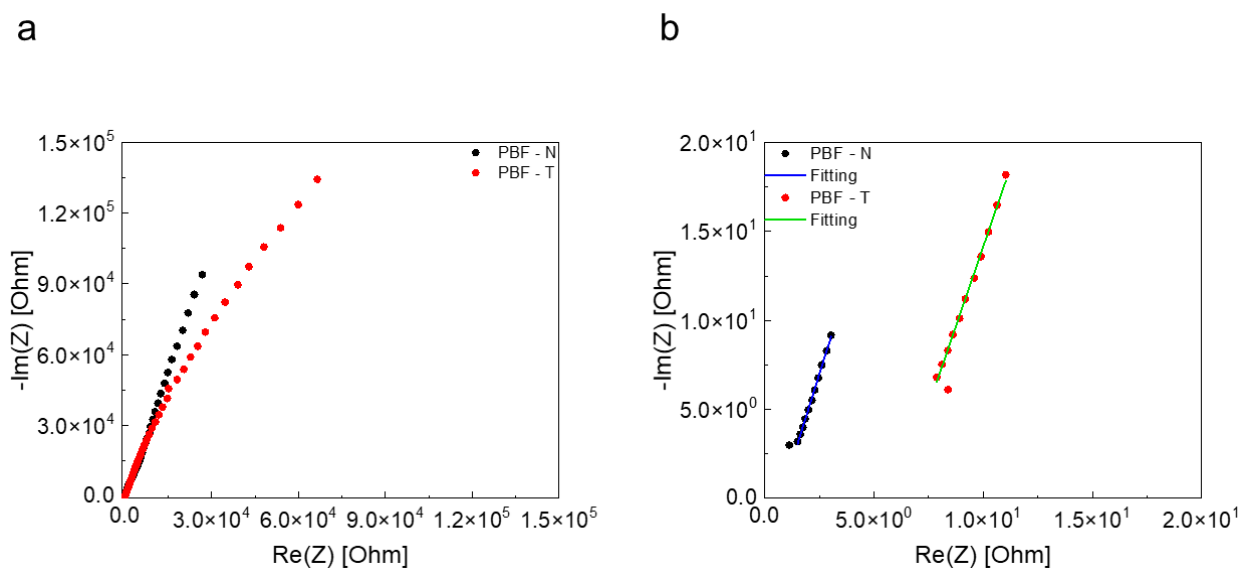
Figure 5.25 (a) PEIS spectrum (20 points/decade) of the stainless-steel symmetrical cell with with PBF - N (black dots) and PBF - T (red dots) separator soaked in LP30, with the magnification (b) and fitting of the high frequency region (200 - 50 kHz)

Despite PBF-N membranes showed a better conductivity compared to PBF-T, traces of solvent from electrospinning process originated some problems following electrochemical stability window evaluation of the PBF-N samples. For this reason, the stability evaluation upon cycling was evaluated only for PBF-T separator through GCD cycles with the same setup and layout used for cell with EVOH/chitosan membranes. The LFP/FP cell with Li metal RE (obtained with the procedure described in chapter 5.5), was tested at constant current with charge and discharge cycles between 2.5 and 4.0 V.

Three cycles at C/10 were performed, followed by prolonged cycles at C/2. The charge and discharge profiles at different C-rates are displayed in Figure 5.26.

Charge and discharge profiles appears symmetrical at both C-rates, with a visible increase of the potential because of the polarisation of electrode, up to 3.8 V, due to the initial de- lithiation of LFP electrode. The latter during the first cycle at C/2, disappeared and the charge profile appears flatter and uniform. As expected, the potential difference between charge and discharge plateaux varies slightly moving from C/10 to C/2 and reaches almost 0.2 V at C/2.
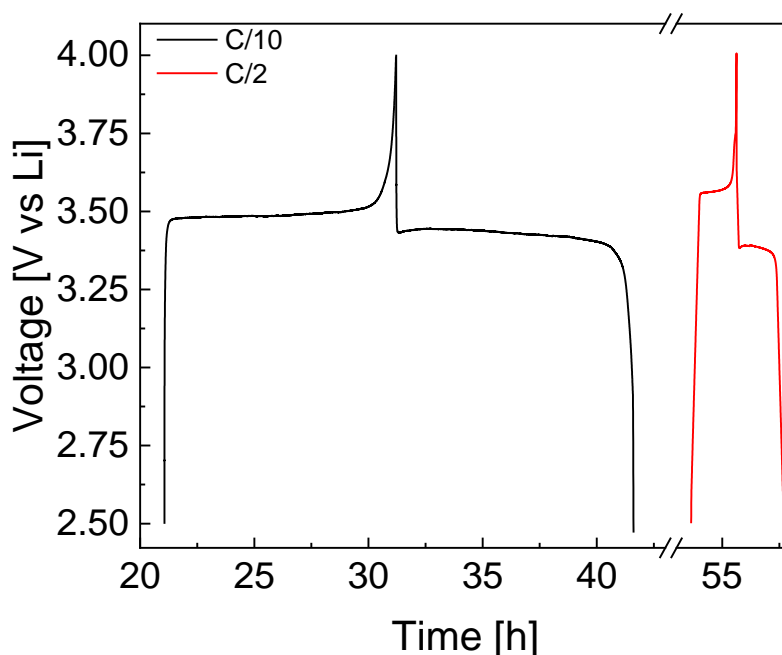
Figure 5.26 Potential vs time profiles of LPF electrode with PBF-T separator soaked in LP30 during GCD cycles at C/10 (black line) and C/2 (red line) c-rates

The specific capacity values and coulombic efficiency values of the cell with PBF-T, are shown in Figure 5.27. They are quite low during the initial cycles both at C/10 and extending also to the initial C/2 cycles, equal to 120 mAh g^{-1}, similar to what observed

in the system with EVOH/chitosan, due to wettability and initial poor contact between the active material and the other electrodes components [218]. However, the system behaviour improves upon cycling, and after 100 cycles a specific capacity of 136 mAh g^{-1} is achieved, which is quite interesting since these are values not far from what was obtained in other studies involving LFP electrodes coupled with commercial separator [219].
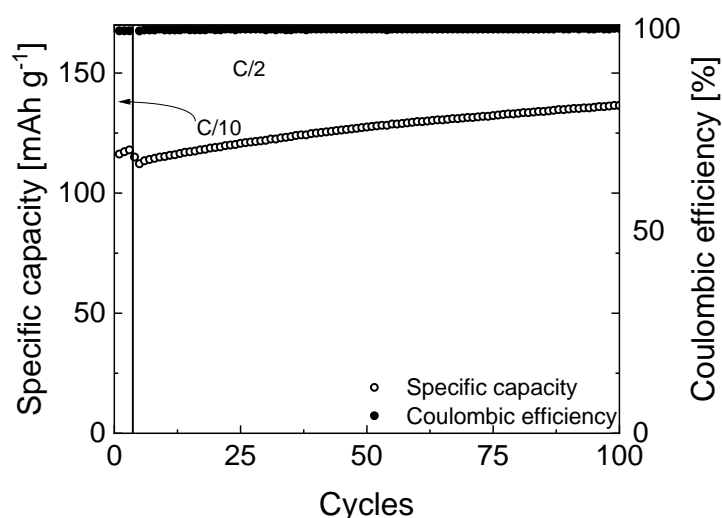
Figure 5.27 Capacity retention (void dots) and coulombic efficiency (full dots) data of LFP electrode in LFP/LP symmetrical cell with PBF-T separator soaked with LP30 electrolyte over testing at C/10 and C/2

5.7   Applications and specifications

As reported in this chapter, adopting new types of polymers and deposition techniques could guarantee better porosity and comparable electrochemical stability with insertion electrodes featuring less environmental impact as well. Separator greatly influence life cycle of the cell, affecting mass transport that ultimately could lead to uneven lithium plating, with cell presenting lithium metal anodes, and unbalancing issues in the case of insertion electrodes.

Polyolefinic membranes are widely use and manufacturing process are well developed, therefore there isn't much space for further developments. Nevertheless, the improvement of mass transport especially for high currents charge and discharge cycling, and of the carbon footprint of battery manufacturing, is urgent and might be addressed with the use of novel polymer originated from renewable sources or from biodegradable polymers. If the use of biopolymers comes in addition to the use of aqueous processing this would represent an added value not only for the environment and human health but also to lower the costs.

While electrospinning proved to be a valuable technique for obtaining porous membranes, even with new kind of biopolymers, currently is not a technique that find application at industrial scale for continuous manufacturing processes, despite much research have been done. Phase inversion process might represent the optimal point for developing separator for LIBs with tailored porosity and representing a deposition technique that could be part of a continuous production process for LIBs assembly.

6 Polymer electrolyte

In this final chapter, a novel polymer electrolyte, made partially by cellulose to improve the sustainability as well as the safety of lithium metal batteries, was investigated. This research was carried out during the Ph.D secondment at CIC Energigune in Polymer Electrolyte group under the supervision of Dr. Maria Martinez, Dr. Devaraj Shanmukaraj and the advisory of Prof. Michel Armand. Following the experience matured with the study of polymers, initially as binder for electrodes and subsequently to obtain novel separator for LIBs, the natural following step was to introduce biopolymers for the synthesis and manufacturing of polymer electrolyte (PE) for lithium metal batteries.

In this chapter, a new synthesis and functionalization was performed to introduce cellulose as a component for PE with the aim to reduce the number of conventional polymers such as the polyethylene oxide (PEO). The experimental work presented in chapter 6.4 is focused on the synthesis of functionalized lithiated cellulose and electrochemical characterization of the obtained membrane to assess the stability with lithium metal anodes.

6.1   *Polymer electrolytes for Li metal batteries*

In chapter 3.1, the importance of PEs introduction for LIBs has been already introduced. PEs started to be conceptualized during the early 70's though they have been proposed as PE for LIBs in 1978 by M. Armand [220], and it was until the early 2000s that polymer electrolyte-based LIBs have been commercialized by Sony Corporation [221]. PEs can serve as both an electrolyte and a separator simultaneously,

combining the ionic conductivity of liquid with the mechanical properties of solid materials, effectively performing a dual function: electrolyte and separator role at the same time, as depicted in Figure 6.1. Conventional organic liquid electrolytes provide superior ionic conductivity, enabling faster ion transport and improved charge/discharge rates in batteries, but they often lack stability and safety. In contrast, PEs, typically solid polymers added with suitable salts, offer enhanced stability and safety, although at the cost of lower ionic conductivity compared to their liquid counterparts [222].
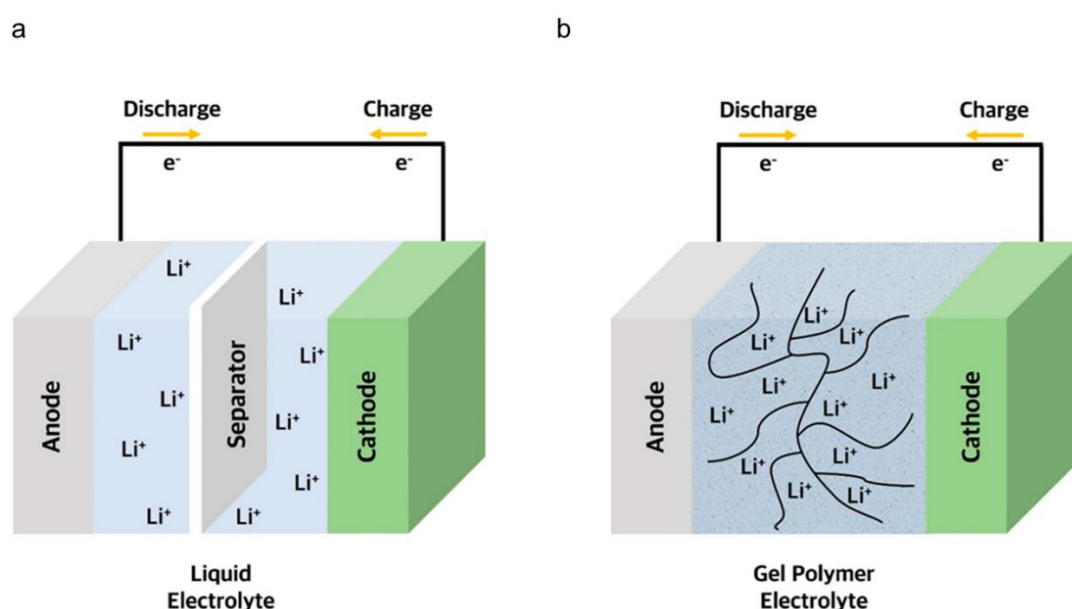
Figure 6.1 Schematic diagram of a cell using (a)) liquid electrolyte and (b) polymer electrolyte [223]

Solid electrolytes provide superior safety and thermal stability compared to liquid electrolytes because they suppress more effectively lithium dendrite growth, making easier the use of lithium metal anodes. However, their development must address the limited ionic conductivity and poor electrode wettability. Table 6.1 summarizes the main characteristics of the two different electrolyte types. To meet commercial demands, PEs must exhibit high ionic conductivity, appropriate mechanical properties, and

exceptional interfacial stability with electrodes [224–226]. A flexible and soft material is essential to adapt to volume changes during charging and discharging cycles. In polymer electrolytes, ionic conduction occurs near the T_g, with the relatively low conductivity being offset by the material's adaptable form, size, and flexibility.

	Liquid electrolyte	Polymer electrolyte
Conductivity	High	Low
Electrochemical stability window	Wide (up to 5 V)	Limited towards high potentials (up to 4.2 V)
Resistance	Low	High interface resistance
Stability	High reactive with lithium metal anode and high voltage cathodes	Stable upon cycling and with lithium metal anode
Safety	Fire risk, especially with lithium metal anode	Flammability is suppressed

Table 6.1 Many characteristics of the liquid and polymer electrolytes

The preparation of PEs relies on the delocalized charge of the anion, based on the lattice energy of the associated salt. These electrolytes are formed by dissolving lithium-based salts in a high molecular weight polymer host, such as PEO, creating dual ionic conductors. However, the simultaneous movement of both cations and anions can cause concentration polarization, negatively affecting battery performance. To solve this issue, a single-ion conductor either a cation or an anion can be used as the charge carrier [221,227].

6.1.1 Types of polymer electrolytes

Conventional PEs are typically fabricated by incorporating lithium salts into a polymer matrix, forming a dual-ion system where both lithium ions and anions are mobile. However, the mobility of lithium ions is often hindered by its strong interactions with the polymer matrix, leading to a transference number for Li^+ below 0.5. This low transference number reflects the high contribution of anions to ionic conductivity [228].

In general, relatively small anions are preferentially selected in PEs to enhance ion diffusion kinetics during cycling, such as PF_6^-, BF_4^- and FSI^- [229]. Anions, being non-reactive in the electrochemical processes, accumulate near the electrode/electrolyte interface, creating a concentration gradient. This phenomenon results in significant cell polarization, manifesting as voltage drops and increased resistance. Over time, these effects contribute to severe performance degradation, limiting the efficiency and lifespan of the cell [230].

Single-ion PEs have gained significant attention to overcome the challenges inherent in dual-ion PEs, particularly the formation of an anion concentration gradient during cycling. The most common strategy involves immobilizing the anion onto the polymer backbone as part of the polymer side chain. This approach enhances the electrolyte's performance by fixing the anionic charge, hence limiting anion migration and preventing the formation of concentration gradients during operation, which facilitate uniform lithium deposition on the metal surface along the electric field direction. Lithium ions become the primary charge transport carrier, thereby increasing the lithium transference number close to unity [231,232].

However, despite their significant advantages, single-ion PEs also exhibit shortcomings that hinders their practical implementation. Among these, the most

critical limitation is their inherently low ionic conductivity, originated from the strong binding interactions between the immobilized anions and lithium ions [231].

6.1.2 Principles of working

The fundamental mechanism of ionic conduction in polymer electrolytes involves the formation of covalent interactions between the polymer backbone and ionizing groups. Initially, the polymer's electron donor component binds to the cationic part of the dopant salt, facilitating ion separation. This interaction triggers an ionic hopping mechanism, schematized in Figure 6.2, enabling ionic conductivity. Cation–polymer interactions are generally strong, and the mean free path for ion hopping is relatively large compared to inorganic electrolytes. These two factors pose challenges that must be addressed to achieve high ionic conductivity through the ion hopping mechanism. Ion hopping, as described by Arrhenius's theory, establishes a relationship (8) between temperature and ion migration, expressed mathematically as:

$$\sigma = \sigma_0 e^{-\frac{E_a}{kT}} \tag{8}$$

where E_a is the activation energy, k is the Boltzmann constant, and T is the absolute temperature; the activation energy can be determined from the slope of a linear plot of $\log \sigma$ versus $1/T$ [233]. In PEs, ion hopping often occurs in conjunction with processes like relaxation, breathing, and/or the segmental motion of polymer chains. Studies have shown that polymer segment and ion motion can cooperate, facilitating the transport of Li$^+$ ions along the polymer chains. Eventually, the ions "hop" from one chain to another, enhancing ionic conductivity [234–236].

Notably, it has been demonstrated that a statically ordered crystalline structure exhibited lower ionic conductivity compared to its amorphous counterpart [237]. This phenomenon arises because, in crystalline regions, lithium-ion transport does not rely on the segmental motion of the polymer chains. Instead, it depends on ion hopping through well-defined spiral channels within the crystalline matrix. This mechanism contrasts with the amorphous regions, where segmental polymer motion significantly influences ion transport, often resulting in lower conductivity.
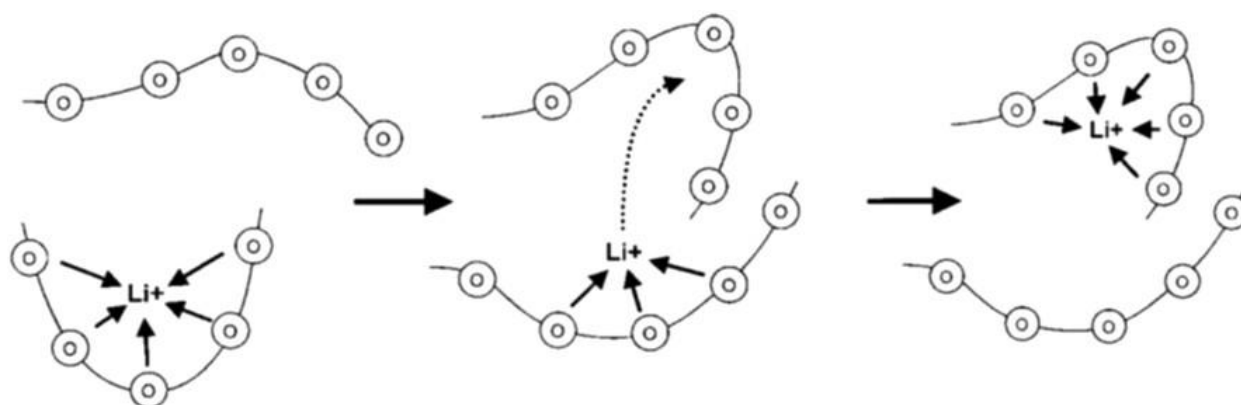
Figure 6.2 Li+ ion transport mechanism in polyethylene oxide-based electrolyte [238]

Room temperature conductivity is still a factor for PEs, and to get sufficient conductivity usually working temperatures in the range of 50 – 90 °C are required, depending on the nature of the polymer and dissolved salt system.

Despite various host polymers have been explored, such as poly(acrylonitrile), poly(propylene carbonate), poly(propylene oxide), poly(methyl methacrylate), and poly(maleic anhydride styrene) for polymer electrolyte preparation, high molecular weight PEO-based electrolytes are considered as the most promising candidates for

the polymer matrix. This preference originates from their exceptional solvation capacity and efficient ion transport mechanism [225].

High molecular weight PEO demonstrates a remarkable ability to dissolve lithium salts, forming a uniform, conductive medium within the polymer matrix. This high solvation capacity ensures effective lithium-ion back and forth movement between the anode and cathode during charging and discharging. Additionally, PEO-based polymer electrolytes exhibit a superior ion transport mechanism, further enhancing their performance in lithium-ion batteries [239].

6.2 Polymer electrolytes

PEs are composed exclusively of polymer matrices and lithium salts, omitting liquid solvents as plasticizers additive. They can be fabricated through methods such as solvent casting, hot molding, or extrusion [240,241]. To qualify for use as PEs, the polymer matrix must meet several critical criteria such as appropriate molecular weight and flexible main polymer backbone, that enhance mechanical strength and reduce the energy barrier for bond rotation, enabling segmental motion and enhancing ionic conductivity. In addition, cation solvation dynamics and high dielectric constant of the polymer matrix help to effectively solvate cations, ensuring salt solubility, allowing hopping between coordination sites. PEs offer several advantages that make them highly suitable for advanced energy storage systems:

- o Mechanical Flexibility to easily adapt to different form factors, supporting applications from thin-film batteries.

o   PEs could operate across a wide temperature range, ensuring safety and performance in various conditions.

o   Unlike traditional liquid electrolytes, PEs reduce fire, or explosion risks due to their inherently non-flammable nature.

o   Their chemical structure and heavy molecular weight prevent degradation and eliminates the risk of leakage, therefore enhancing overall safety.

These properties make PEs particularly appealing for next-generation energy storage solutions, including solid-state batteries and flexible electronics; in addition, their flexibility allows for large scale battery production through currently developed and adjusted roll-to-roll manufacturing processes, where the PE could be seamlessly pasted between the electrode layers [242].

6.3   Polymer electrolytes backbone

Although various host polymers, have been explored for use in polymeric electrolytes, high molecular weight PEO-based polymer electrolytes stand out as the most promising options for the polymer matrix. In Table 6.2 are listed the properties of the most common polymeric host materials. High molecular weight PEO exhibits a unique ability to dissolve lithium salts, forming a uniform and conductive medium within the polymer matrix. This superior solvation capacity enables effective ion transport, facilitating the seamless movement of lithium ions between the anode and cathode during charging and discharging cycles [225,239]. However, the ionic conductivity of PEO-based PEs heavily depends on the polymer matrix's ability to solvate lithium salts and the ratio of crystalline phase to amorphous phase. Since the PEO chain is mostly

crystalline below 65 °C, PEO-based PEs typically exhibit low ionic conductivities in the range of 10^{-8} to 10^{-7} S cm^{-1} at room temperature. This limited ionic conductivity significantly restricts the practical application of PEO-based PEs.

Polymer	Repeating Unit	T_g [°C]	T_m [°C]
PEO	-(CH$_2$CH$_2$O)$_n$-	− 64	65
PVDF-HFP	-[(CH$_2$-CF$_2$)-(CF$_2$-CF-(CF$_3$)]$_n$-	− 90	135
PAN	-(CH$_2$-CH(-CN))$_n$-	125	317
PMMA	-(CH$_2$C(-CH$_3$)(-COOCH$_3$))$_n$-	105	Amorphous

Table 6.2 Glass transition temperature (T_g) and melting temperature (T_m) of polymer materials

6.3.1   Bio-component for polymer electrolytes

Other synthetic polymers, such as poly(propylene oxide) (PPO), poly(vinyl alcohol) (PVA), and poly(vinyl chloride) (PVC), have also been utilized in developing PEs materials, demonstrating roles comparable to PEO in electrolyte systems. However, they have shown as well, high crystallinity and, hence, low ionic conductivity as in the case of PEO membranes [243]. Enhancements in amorphous properties and ionic conductivity have been achieved by incorporating fillers, plasticizers, and by forming polymer blends. However, these synthetic polymers face significant drawbacks, including high costs, toxicity, and non-biodegradability due to their derivation from petrochemical raw materials. Consequently, recent advancements have been focused on environmentally friendly, non-toxic, biodegradable polymers such as cellulose derivatives, starch, chitosan, gelatine, and alginate [244–249]. Polysaccharides drew

significant attention in recent years and have been extensively studied for their potential application as substitutes or alternatives to conventional synthetic polymers as reported in the previous chapters. Each of these biopolymers offers distinct functional properties. For instance, lignin exhibits high oxidative stability, cellulose acetate is water-insoluble and demonstrates excellent film-forming capability, and carrageenan is compatible with salts, making it an ideal candidate for PEs formation. Additionally, natural polymer proteins such as gelatine, soy protein, and silk protein have attracted significant research interest for electrolyte applications. Their chemical and physical characteristics are influenced by the type of amino acid block present (glycine, serine or alanine) and their position and arrangement along the polypeptide chain. Depending on the desired properties, bio-polymer offer wide range of choice to further enhancing their potential for innovative energy storage solutions [250].

Given these interesting properties and considering the purpose of increasing the renewable content of PEs, ethyl cellulose (EC) was selected as co-host, to realize a composite PEs merging EC with a polyether amine diamine–poly(oxyethylene–*co*–oxypropylene), commonly known as Jeffamine®. Their structure is represented in Figure 6.3. Jeffamine® is a polyether polymer, very close to PEO, differing by the moieties at the end of the polymer chains. While PEO chains terminate with -OH groups, Jeffamine® presents -NH$_2$ end groups. However, Jeffamine® presents a significantly less crystalline structure compared to PEO, thus potentially increasing the ionic conductivity [251]. Though, the lower crystallinity degree comes at the cost of lower mechanical resistance [252].
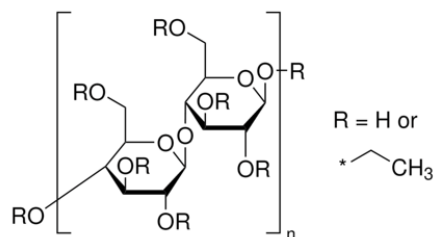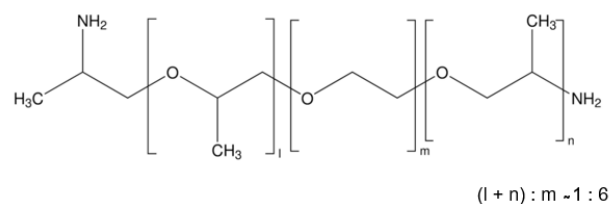
Figure 6.3 Chemical structure of (a) ethyl cellulose (EC) and (b) Jeffamine®

The mixing of EC with Jeffamine®, allowed the realization of a thin and flexible PE, wherein the brittleness and mechanical stiffness due to crystalline nature and strong intermolecular interactions of EC were counterbalanced by the highly viscous texture of the Jeffamine®.

The materials for obtaining the PE have been the following: Jeffamine® M-2070 (Huntsman, $M_w \sim 2000$), ethyl cellulose (EC, Acros Organics, 49 % w/w ethoxyl basis), lithium hydride (Sigma Aldrich, powder ≥95%), fluorosulfonyl isocyanate (FSO$_2$NCO, Provisco 98%), lithium iron phosphate (LFP, Alees), conductive carbon (C-65, Timcal), tetrahydrofuran (THF, Thermo Fischer, anhydrous ≥99.9%), acetonitrile (ACN, Thermo Fischer, anhydrous ≥99.9%), ethanol (EtOH, Scharlab, HPLC grade ≥99.9%), toluene (Scharlab, ACS grade ≥99 %). From now on Jeffamine® is indicated as Jeffamine.

Fourier transform infrared spectra were recorded with a VERTEX 70 Bruker instrument in a range of 400–4000 cm^{-1} with 256 scans and a resolution of 4 cm^{-1}. Differential scanning calorimetry was carried out using a DSC 2500 Discovery Series calorimeter. Samples were subjected to three heating scans from -80 to 200 °C with a heating ramp of 5 °C min^{-1}.

Electrochemical tests have been performed using CR2032 coin cells, assembled in a glovebox (Mbraun Labmaster Eco) in inert argon atmosphere (O_2 < 0.1 ppm and H_2O < 0.1 ppm), using stainless steel, lithium iron phosphate (LFP, active loading 4.5 mg cm^{-2}) and lithium metal disk (MTI Corp., 16 ⌀ mm, 0.6 mm thickness) as electrodes. To determine electrochemical stability window, asymmetrical coin cell have been assembled using stainless steel as working electrode and lithium metal counter electrode. Symmetrical coin cells with stainless steel electrodes have been used to determine the ionic conductivity, while symmetrical cells featuring lithium metal electrodes have been assembled to determine lithium transference number and plating/stripping stability upon prolonged cycling. Galvanostatic charge and discharge (GCD) stability was also evaluated assembling complete cells with lithium metal and LFP electrodes. PEs samples and LFP cathodes have been dried under vacuum at 60 °C prior to cell assembly.

Prior to the begin of every electrochemical measurement, 6 hours of OCV at the temperature of 70 °C have been set to allow for the PE to equilibrate and to establish a good contact with the electrodes surface.

Ionic conductivity measurements have been performed at different temperatures, from 30 °C to 80 °C, leaving the cell resting to conditionate at each temperature for 1 hour. Conductivity values have been obtained from charge transfer resistances by potentiostatic electrochemical impedance spectroscopy (PEIS), applying 10 mV of perturbation, recording 20 points per decade in the frequency range 1 MHz – 100 mHz.

CVs to verify the PE membrane electrochemical stability window, have been performed with a scanning rate of 20 mV s^{-1}, for 10 consecutive cycles in three electrodes mode, at 70 °C.

GCD cycles were carried out, with the working and counter electrodes made of lithium metal electrodes, applying 5 cycles 10 µA cm^{-2} and then prolonged cycles at 50 µA cm^{-2} for two hours each stripping/deposition, to verify the resistance of the PE to lithium dendrites.

GCD cycles of lithium / LFP cells were carried, in three electrodes mode, performing 5 initial cycles at C/20 to condition the materials and then prolonged cycles at C/10, to verify the stability of the cells at different current densities and prolonged cycling. All GCD measurements were performed at a constant temperature of 70 °C.

6.4 Jeffamine/EC-Li electrolyte preparation

Cellulose functionalization was carried out according to the procedure developed in-house by Boaretto et al. [253] and represented in Figure 6.4. EC was initially lithiated using LiH. In a typical procedure, pre-dried EC was dissolved in anhydrous THF and added dropwise using a dropping funnel to a three-neck round-bottom flask containing 3 equivalents of LiH suspended as well in THF. The reaction was performed under an argon atmosphere, over an ice bath, and then stirred at room temperature overnight. To remove excess LiH, EtOH was added, causing the lithiated EC to precipitate. The precipitate was redissolved, and solvents were removed using a rotary evaporator. The resulting white powder was transferred to a Schlenk line under argon and dried at 70 °C under vacuum overnight.

The lithiated ethyl cellulose (EC-Li) was dispersed in anhydrous acetonitrile within a round-bottom flask equipped with a septum and stopcock for the functionalization with 3 equivalents of fluorosulfonyl isocyanate (FSO_2NCO). FSO_2NCO was added dropwise to the suspension under argon atmosphere, gradually dissolving the polymer. The mixture was stirred overnight at room temperature to ensure complete reaction. The functionalized EC-Li was then precipitated by pouring the solution into cold toluene, followed by filtration. The resulting product was dried under vacuum at 70 °C overnight, yielding approximately 90% of the theoretical value.
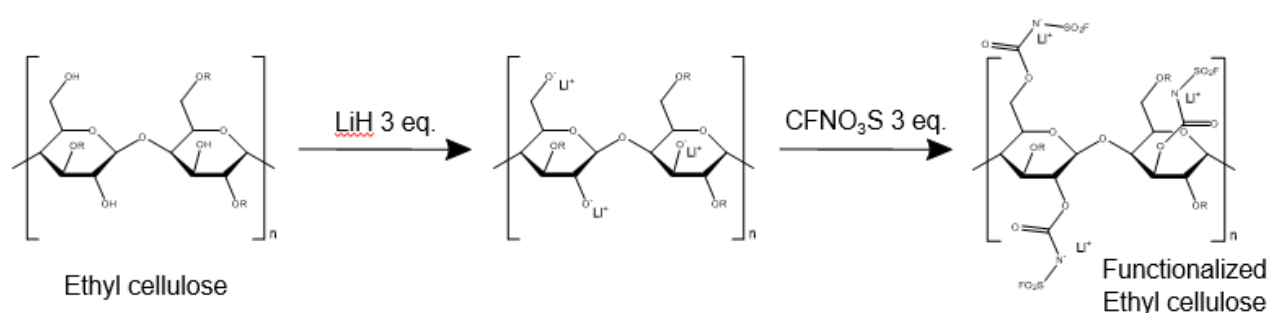
Figure 6.4 Synthesis procedure of lithiated and functionalized ethyl cellulose

The electrolyte was prepared by mixing Jeffamine and EC-Li in acetonitrile, followed by solvent casting the polymer solution in a Teflon mold. The excess of ACN was removed by heating at 70°C overnight. Lastly, Jeffamine/EC-Li membrane has been peeled off from the mold and hot pressed at 60 °C until reaching the thickness of 100 μm.

Three different Jeffamine:EC-Li ratios have been tested (60:40, 50:50 and 40:60 wt:wt), to find the optimal proportions in terms of mechanical characteristics, as could be seen on the obtained membranes with different ratios displayed in Figure 6.5. The PE made with the 60:40 wt:wt ratio, visible in Figure 6.5c, was unable to form a uniform

membrane and appeared as a sticky jellyish gelatine. A film was obtained only after hot pressing the recovered material.
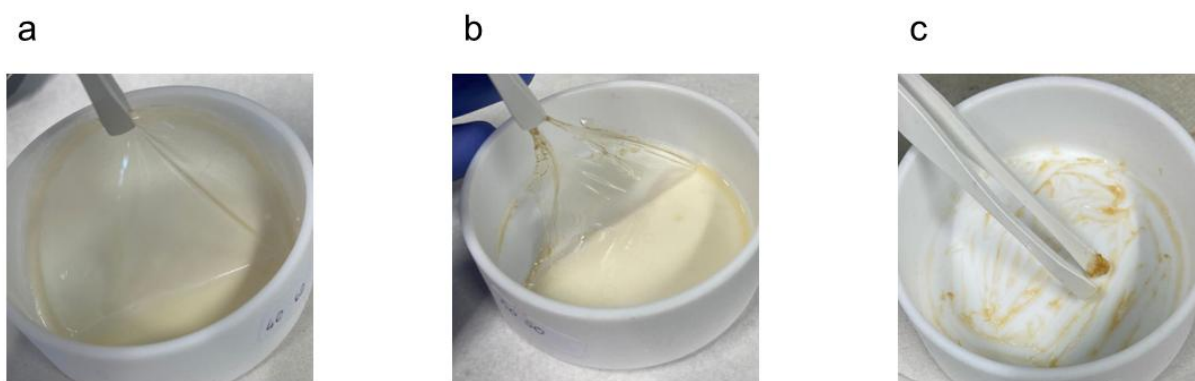
Figure 6.5 Polymer electrolytes made of Jeffamine/ECLi in three different weight ratios: (a) 40:60, (b) 50:50 and (c) 60:40 respectively

6.5   Jeffamine/EC-Li electrolyte characterization

The three PEs with different ratios have been physical-chemically characterized with FTIR spectroscopy and DSC thermal analysis.

FTIR spectra, recorded with 64 scans from 500 to 4000 cm^{-1}, of pristine EC powder and Jeffamine/EC-Li membrane are reported in Figure 6.6. With the exception of the different relative intensity of absorption between peaks of the 60:40 Jeffamine/EC-Li membrane and the other two, due to the increased amount Jeffamine, the spectra are similar. This confirms that the structure of EC-Li is not affected by the mixing with Jeffamine. However, the Jeffamine/EC-Li membrane spectrum shows additional signals resulting from S–N stretching at 768 cm^{-1}, S–F stretching at 868 cm^{-1}, symmetric and asymmetric SO_2 stretching at 1201 and 1337 cm^{-1}, respectively, and carbamate C=O stretching band at 1660 cm^{-1} compared to the EC powder.
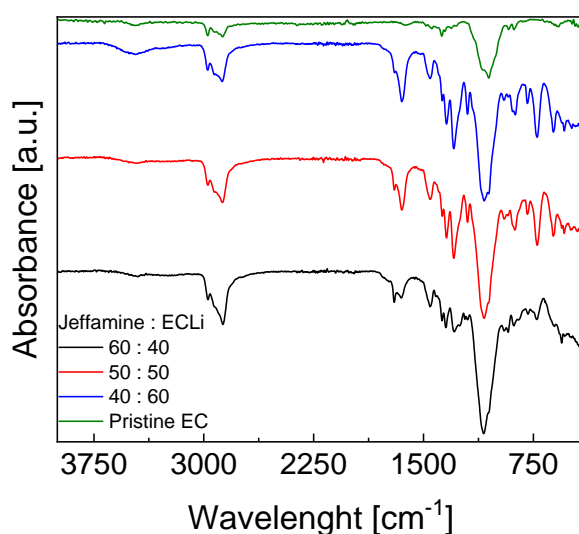
Figure 6.6 FTIR spectra of pristine ethyl cellulose (green line) and Jeffamine/EC-Li PE at different composition: 60:40 (black line), 50:50 (red line) and 40:60 (blue line) respectively

Figure 6.7 shows the DSC thermograms performed with a heating ramp of 5 °C min^{-1} from -80 °C to 100 °C. The sample with the highest amount Jeffamine exhibits the lowest T_g, around -40 °C. This is in line considering that Jeffamine T_g is around – 66 °C [254], while pure EC T_g is 130 °C [255]. On the other hand, the samples containing 50:50 and 40:60 of Jeffamine/EC-Li show a much smaller difference between the T_gs, which are -15 °C and -5 °C, respectively. This might be ascribed to the fact that once Jeffamine is present in a certain composition range it promotes the formation of amorphous regions in the PE, affecting glass transition temperature more effectively than EC.
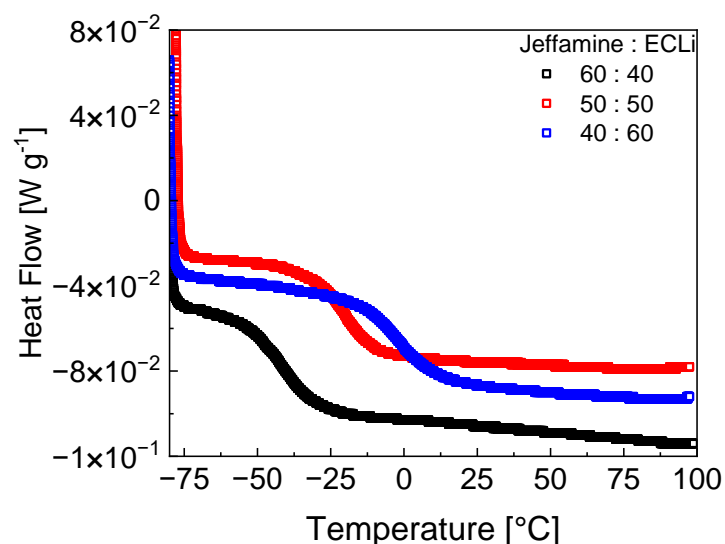
Figure 6.7 DSC curves of Jefammine/EC-Li in different wt. % ratios: 60:40 (black dots), 50:50 (red dots) and 40:60 (blue dots) with a ramp of 5 °C min^{-1} from -80 °C to 100 °C

Beyond physical-chemical characterization, the Jeffamine/EC-Li PEs with the three different compositions have been electrochemically investigated to evaluate which composition exhibited the better electrochemical properties.

Ionic conductivity measurements from RT to 80 °C have been performed to evaluate the temperature dependency of the three PE compositions. Results are shown in Figure 6.8. It could be seen that despite the higher content of EC-Li, i.e. the higher content of lithium polysalt, the Jeffamine/EC-Li 60:40 showed the lowest ionic conductivity, especially at RT, with a difference of about 2.5 orders of magnitude with respect to the other two compositions. This might be due to the higher crystalline content that hinders the lithium mobility despite the higher concentration. The other two PEs possess the same value at RT, $4 \cdot 10^{-6}$ S cm^{-1}, but the PE with the ratio of 50:50, marked higher values as the temperature increases, eventually reaching $3 \cdot 10^{-3}$ and

5.9·10⁻⁴ S cm⁻¹ at 70 °C and 80 °C, respectively. These values are comparable with ionic conductivity of common PEs made with a blended polysalt [253,256–258].
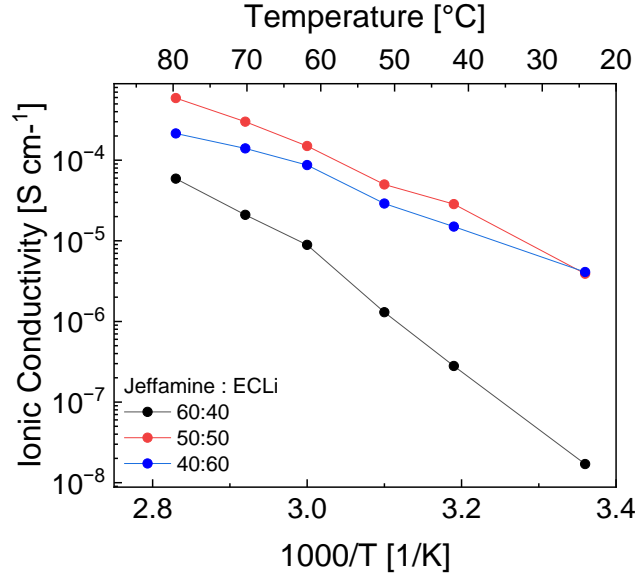
Figure 6.8 Ionic conductivity of Jeffamine/EC-Li PE with different weight ratio, measured between 25 °C and 80 °C

Lithium ion transference number (t^+) was determined by using the Bruce Vincent method [259] and the results are in Table 6.3. The lithium-ion transference number was evaluated at 70 °C through combined alternated current PEIS analysis with the direct current (DC) polarization method in a symmetrical Li//Li cell containing the PE. During the experiment, a DC voltage of 10 mV was applied until the current stabilized. PEIS spectra were collected before and after DC polarization across a frequency range of $10^6 - 10^{-1}$ Hz, using a voltage AC amplitude of 10 mV. The Li⁺ transference number was calculated using the Bruce and Vincent equation (15):

$$t^+ = \frac{I_S(\Delta V - I_0 R_i^0)}{I_0(\Delta V - I_S R_i^S)}$$

(15)

where I_0 and I_S are the initial and steady-state currents, respectively, R_i^0 and R_i^S represent the initial and final interfacial resistances between the lithium metal electrode and the electrolyte and ΔV is the applied constant DC voltage.

This method considers both the change in current and the interfacial resistance before and after DC polarization to obtain the transference number.

t^+ was determined to be 0.71 with the Jeffamine/EC-Li 50:50 sample that is a quite high value with respect to typical values obtained for dual ion conductor PEs (<0.6) [260]. Polymeric single-ion conductors have been designed with the aim to enhance the lithium t^+. These polyelectrolytes feature anions covalently bonded to the polymer backbone, making the counter lithium ions the only charge species able to move. Unlike conventional polymer electrolytes, single-ion conductors achieve lithium t^+ values approaching unity. However, this improvement is accompanied by a significant decrease in ionic conductivity, typically falling below 10^{-6} – 10^{-7} S cm^{-1} at RT. Incorporating liquid plasticizers, room-temperature ionic liquids, or inorganic particles has been demonstrated as an effective approach to enhance ionic conductivity, by inhibiting the polymer crystallization and decreasing the T_g, at the cost of lowering lithium t^+, forming interactions with the polymeric matrix thus, hindering the segmental movemements. [260,261].

The other two samples showed t^+ lower, around 0.6, because in the sample with 60 % wt. of EC-Li excessive amount of polysalt could acts as a weak sort of cross-linker, with the formation of ionic clusters and ionic pairs. These formations impede the mobility of polymer chains, reducing the ionic conductivity and the cation transference number. For the 40 % wt. of EC-Li sample, the excessive amount of Jeffamine didn't allow for a good mechanical integrity and membrane forming [256].

Composition (Jeffamine/ECLi)	Transference number [t^+]
40:60	0.57
50:50	0.71
60:40	0.63

Table 6.3 Lithium transference numbers (t^+) for Jeffamine/EC-Li PEs with different weight ratio

Considering the ease of handling, the ionic conductivity and lithium t^+, only the sample Jeffamine/EC-Li with 50:50 % wt. was electrochemically characterized.

Cyclic voltammetry was used to investigate the electrochemical stability window of the Jeffamine/EC-Li PE. Figure 6.9 presents the CVs recorded at a scan rate of 0.1 mV s^{-1} of two cells in the voltage range of – 0.5 and 1.5 V and 3 and 5 V for 10 cycles each, at 70 °C.

A stable lithium plating/stripping behavior was observed with Jeffamine/EC-Li PE upon cycling near 0 V. However, compared with the initial cycle, the plating and stripping becomes more resistive, as shown by the oxidation peak that broadens and moves slightly towards more positive voltages and the deposition starts at lower potentials.
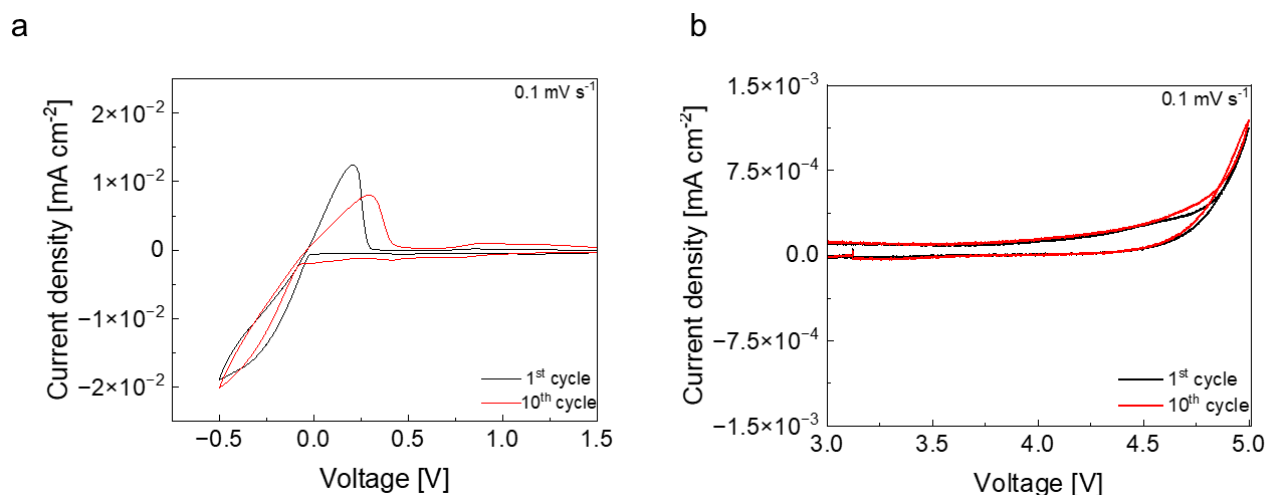
Figure 6.9 Cycling voltammetries of stainless steel/Lithium metal with Jeffamine/EC-Li electrolyte performed at 0.1 mV s^{-1} between (a) – 0.5 and 1.5 V and (b) and between 3 and 5 V

Jeffamine/EC-Li PE was tested towards oxidation stability, where emerged its major issue. While ethyl cellulose demonstrated to be stable upon oxidation until 5 V [262], Jeffamine doesn't possess a similar stability towards oxidation and as a result an increase in the anodic current, starting from 4.3 V, is due to progressive oxidation of the PE over cycling.

The stability of Jeffamine/EC-Li PE towards lithium plating and stripping was further investigated in symmetric lithium metal cells at 70 °C, starting with 5 cycles at a current density of 10 µA cm^{-2} and then prolonged cycling at 50 µA cm^{-2}. The plating and stripping cycles are visible in Figure 6.10. Symmetric coin cells cycled for over 1000 cycles without underwent short circuit. However, the overvoltages steadily increased upon cycling eventually reaching 380 mV. This behaviour could be ascribed both to the formation of layer composed by dead lithium and, to a lesser extent, to lithium ions depletion at the electrode surface as a result of transport limitations within the Jeffamine/EC-Li PE, that became relevant at the higher current density.
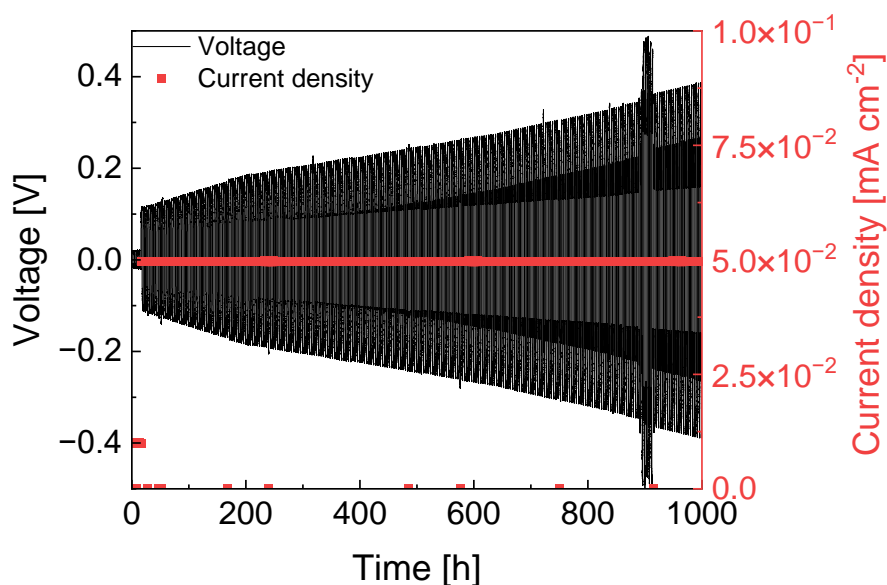
Figure 6.10 Deposition and stripping cycles of Li//Li symmetrical cells with Jeffamine/EC-Li at 10 and 50 µA cm⁻²

The detail of deposition and stripping processes are shown in Figure 6.11. As explained in chapter 5.5, smooth and flat lithium surface results from uniform lithium deposition, where only the freshly deposited lithium is stripped, is observed during the first cycles at 10 µA cm^{-2}. This process maintains a constant overvoltage, as stripping occurs on a surface with uniform resistance.

On the contrary, during cycles at 50 µA cm^{-2} the typical arched profile appears, due to hindered mass transport and to rough contact interphase between electrode and electrolyte, and maintains after 500 hours, as well as after 1000 hours.
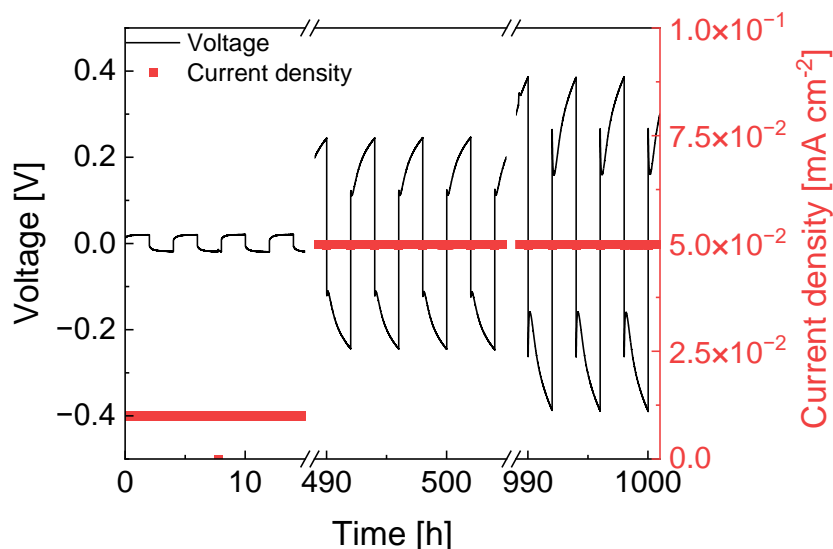
Figure 6.11 Selected overvoltage profiles of lithium deposition and stripping in Li//Li symmetrical cell with Jeffamine/EC-Li at 10 and 50 µA cm⁻²

Jeffamine/EC-Li PE behaviour was tested with an LFP cathode and lithium metal anode at 70 °C, starting with 5 formation cycles at C/20 and then prolonged cycling at C/10. Figure 6.12 shows the profiles of LFP at C/20 and C/10.

Charge and discharge profiles appears with a good symmetry between oxidation and reduction at both C-rates, and displays low values of overpotential between reduction and oxidation plateaux, in the order of 50 and 90 mV at C/20 and C/10, respectively.
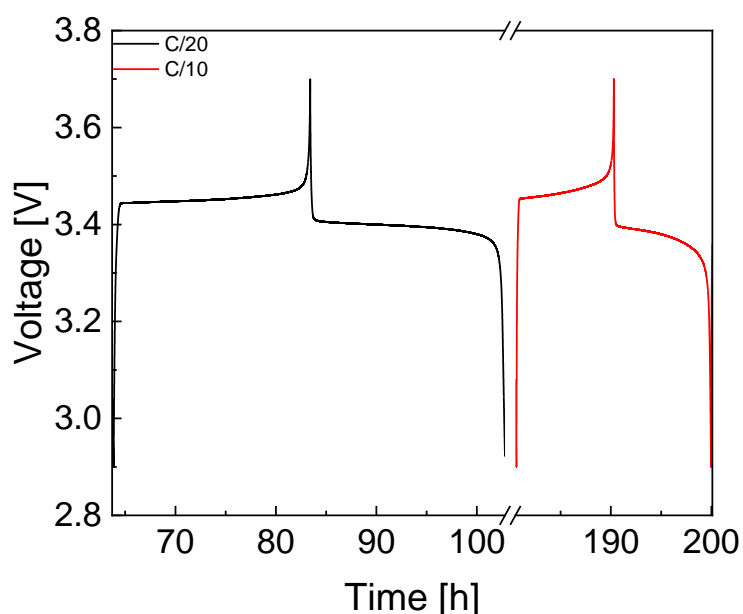
Figure 6.12 Potential vs time profiles of LFP//Li cell with Jeffamine/EC-Li electrolyte during GCD cycles at C/10 (black line) and C/2 (red line) at 70 °C

The specific capacity values and coulombic efficiency values of cells with LFP cathode and lithium metal anode with Jeffamine/EC-Li, are shown in Figure 6.13.

Since the very first cycles at C/20, cell exhibited high specific capacity values close to 150 mAh g^{-1}. Increasing the C-rate at C/10, apart from some cycles where some spikes could be seen because of forced breaks due to equipment maintenance, coulombic efficiency values remain constant around 100%, and no drop of specific capacity values is reported, which are maintained almost constant for 35 cycles. After 40 cycles due, a steady decrease of the specific capacity values is observed, with a recorded value of 135 mAh g^{-1}, due probably to lithium-ion diffusion issue across the PE.

Nevertheless, the behaviour observed can tell us that no critical interactions arise with the use of LFP electrode with Jeffamine/EC-Li PE over prolonged cycling, suggesting its suitability with these cathodes.
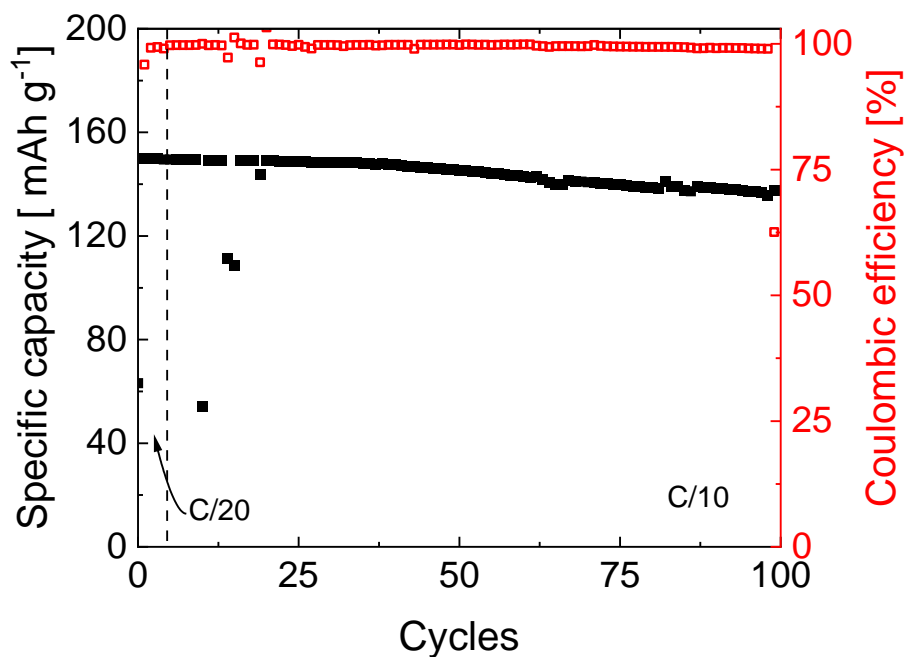
Figure 6.13 Specific capacity (full black dots) and coulombic efficiency (void red dots) data of LFP/Li cell with Jeffamine/EC-Li polymer electrolyte over testing at C/20 and C/10

6 Applications and specifications

As reported in this chapter, it was demonstrated that single-ion polymer electrolyte by implementing biopolymer as host matrix could be a viable option to realize more sustainable PEs and, thus, environmental benign LIBs.

The use of solid-state electrolytes represents the most promising solution for addressing safety concerns associated with the combination between polymer separators and flammable organic liquid electrolytes. In particular, with batteries featuring lithium metal anodes, PEs have the advantage of providing a physical barrier towards lithium dendrites growth and penetration.

While the most employed PEs make use of PEO and PVdF-HFP polymers coupled with fluorinated salts, which exhibit high ionic conductivity even at RT and good

flexibility, there is huge research to lower the content of fluorine and increase the use of biopolymers for improving the carbon footprint of the final device.

Single-ion conductor PEs could represent a viable solution for overcoming the relatively low ionic conductivity, that represents the biggest obstacle upon PEs use. The second major issue arise from high interfacial resistance, which could be addressed using polymer blend or tuning PEs composition with appropriate plasticizers in an appropriate manner not to block polymer motions thus maintaining a good lithium-ion mobility.

7 Conclusions

In this thesis new polymer materials originated from renewable sources for EESS, and the study of innovative processing techniques for the production of devices' components, have been investigated for the development of new energy storage technologies with low environmental impact. Among EESS, covering most of the energy and power requirements needing to support the current energy transition towards renewable energy sources, lithium-based battery technologies and aqueous EDLCs have been considered.

Aqueous EDLCs represent a promising choice to obtain more sustainable devices where high specific power represents the main requirement. For these systems, the attention was focused on the chemical modification of a water-soluble biobased binder for the electrodes to prevent their dissolution under use in aqueous environment. Activated carbon electrodes added with modified chitosan binder (AC MA) exhibited superior coulombic efficiency values of 99% at different specific currents, as well as increased specific capacitance values around 140 F g^{-1} at 0.5 A g^{-1}. These electrodes showed good stability over 5000 cycles, with a capacitance retention of ca. 90%. The feasibility of AC MA electrodes working in aqueous systems has been demonstrated, as well as the possibility of an easy and environmentally friendly direct recycling of electrodes materials without using time and energy consuming methods, occurring with an acid hydrolyzation of the crosslinking bridges with a diluted aqueous solution of acetic acid.

I also investigated separators, mainly for the use in lithium-based batteries, which currently represent the most used EESS for electronic devices and electrical vehicles, for improving their sustainability. Keeping in mind industrial processing requirements

for separator handling and batteries manufacturing as well as environmental concerns, an innovative all aqueous phase inversion casting process was developed for obtaining membranes made with poly(vinyl alcohol-*co*-ethylene) and chitosan. By choosing the antisolvent mixture of the coagulation bath and the immersion time for the phase inversion, I proved that it is possible to tailor porosity of the membranes. In collaboration with Manz Italy s.r.l., the feasibility upon lamination process of this separators was studied as well as the electrochemical performance in a LFP//FP cell. To overcome the brittleness of this separator, I introduced PEGDME as plasticizer, and preliminary cycling with lithium metal electrodes showed a better stability over prolonged stripping and deposition than those previously achieved, demonstrating better resistance even to lithium dendrites. Given the promising results obtained with the use of PEGDME as plasticizer, the next step would be to use a polymer plasticizer derived from renewable sources to obtain a membrane with a higher renewable content.

In addition, thanks to a collaboration with the department of Civil, Chemical, Environmental, and Materials Engineering of University of Bologna and Department of Industrial Engineering of University of Trento, a similar characterization of electrospun membranes based on poly(butylene 2,5 furanoate) (PBF), a polymer obtained completely by renewables feedstocks never used before as separator for LIBs, was carried out. Due to its extremely porous nature, this separator exhibited very low values of the MacMullin number, indicating an excellent capability of lithium ions migration across the membrane. PBF separator demonstrated good stability over 100 cycles of a symmetric LFP//FP cell marking coulombic efficiency close to 100% and specific capacity values that ultimately reached 135 mAh g^{-1} at C/2.

Finally, given the safety issues originated from lithium metal anodes, in particular from dendrites formation and growth, the adoption of a polymer electrolyte that merges both electrolyte and separator roles looks to be the most promising option to address those issues. The activities have been carried out during my period abroad at CIC Energigune (Spain) and focussed on the synthesis of a lithium polysalt, based on ethyl cellulose (EC-Li), which was mixed with Jeffamine to obtain a single-ion PE made with 50% wt/wt of renewable materials. The characterizations validated the effectiveness of the synthesis procedure and the best ionic conductivity and ease of handling of the 50% wt/wt mixture. The Jeffamine/EC-Li cycled for more than 1000 hours in symmetrical lithium metal electrodes cell, demonstrating good resistance to lithium dendrites at a current density of 50 μA cm^{-2}, and also in complete Li//LFP cell, with LFP achieving a specific capacity value above 135 mA g^{-1} for more than 100 cycles at C/10 at 70°C.

These results show the feasibility of the implementation of new separators and electrodes making use of less environmental harmful materials and processes. The separators are suitable to be implemented in continuous production lines, coupled with materials that are originated from renewable sources and/or might be able to biodegrade.

However, it is crucial to develop a membrane exhibiting appropriate physicochemical properties—such as density and electrolyte uptake—in order to avoid detrimental impacts on the specific energy of the cell. This consideration is particularly inherent given that batteries employing liquid electrolytes are characterized by high ionic conductivity, which is essential in high-power applications, as well as elevated energy density and specific energy for miniaturized devices. On the other hand, in scenarios where these performance metrics are less critical, solid-state polymer batteries offer

substantial safety advantages by mitigating the risks of fire and thermal runaway in the event of short circuits. These benefits arise from the use of a polymer electrolyte that is typically thicker than conventional separators and exhibits lower ionic conductivity at room temperature.

Future efforts will be focused on the adoption of biogenic plasticizers to improve the mechanical resistance of EVOH/chitosan membranes, as well as the development of a PE with a higher percentage of biopolymers.

Activities and publications

Schools

Elmo – Lion school, March – May 2023, 160 hours, 6 ETCS credits

Conventional and High-Energy Spectroscopies for Inorganic, Organic and Biomolecular Surfaces and Interfaces (CHESS) school in virtual mode, February 21st – 25th 2022

Conferences

L. Bargnesi, A. Rozzarin, C. Arbizzani, *Maleic anhydride-modified chitosan binder for sustainable aqueous electrochemical energy storage systems;* Giornate Italiane dell'elettrochimica 2022, Orvieto (TN), September 11th – 15th 2022, Poster

L. Bargnesi, C. Arbizzani, *Functionalized and Sustainable Separator Enabling Safer and Long Cycling Lithium Batteries*; 73rd Annual meeting of International Society of Electrochemistry, virtual mode, September 12th – 16th 2022, Oral

L. Bargnesi, A. Rozzarin, G. Lacarbonara, S. Tombolesi, C. Arbizzani, *Sustainable modification of chitosan binder for electrodes operating in aqueous electrolytes;* 30 years of INSTM, Bressanone (BZ), January 22nd – 25th 2023, Oral

L. Bargnesi, G. Lacarbonara, C. Arbizzani, *Sustainable Separator for Lithium-ion and Lithium Metal batteries*; 74th annual meeting of the International Society of Electrochemistry, Lyon (FR), September 3rd – 8th 2023; Oral

L. Bargnesi, S. Santi, G. Fredi, M. Soccio, N. Lotti, A. Dorigato, C. Arbizzani, *Electrospun membranes of polyethylene furanoate derivatives for multi – purpose applications*, 28th conference of the Italian Chemical Society, Milano, August 26th – 29th 2024; Poster

L. Bargnesi, T. Ivancic, N. Boaretto, I. Aldalur, D. Shanmukaraj, M. Martinez, M. Armand, C. Arbizzani, *Novel polymer electrolyte for greener and safer solid-state*

batteries, 2024 Materials Research Society Fall meeting & exhibit, Boston (US), December 1st – 6th 2024, Poster

ISEECap 2022, Bologna, July 11th – 15th 2022 (Student Helper)

Publications

L. Bargnesi; F. Gigli; N. Albanelli; C. Toigo; C. Arbizzani *Crosslinked chitosan binder for sustainable aqueous batteries* Nanomaterials 2033, *12*(2), 254.

L. Sheng, X. Xie, C. Arbizzani, L. Bargnesi, Y. Bai, G. Liu, H. Dong, T. Wang, J. He *A tailored ceramic composite separator with electron-rich groups for high-performance lithium metal anode* Journal of Membrane Science 2022, 657

L. Bargnesi; A. Rozzarin; G. Lacarbonara; S. Tombolesi; C. Arbizzani *Sustainable Modification of Chitosan Binder for Capacitive Electrodes Operating in Aqueous Electrolytes* ChemElectroChem 2023, 10, e202201080

D. Di Cillo; L. Bargnesi; G. Lacarbonara; C. Arbizzani *Ammonium and Tetraalkylammonium Salts as Additives for Li Metal Electrodes* Batteries 2023, 9, 142

S. Tombolesi; N. Zanieri; L. Bargnesi; M. Mernini; G. Lacarbonara; C. Arbizzani *A Sustainable Gel Polymer Electrolyte for Solid-State Electrochemical Devices* Polymers 2023, 15, 3087

G. Lacarbonara, M. Sadd, J. Rizell, L. Bargnesi, A. Matic, C. Arbizzani *Operando insights into ammonium-mediated lithium metal stabilization: surface morphology modulation and enhanced SEI development* Journal of Colloid and Interface Science 2024, 669

M. Hashem; R. S. El-Tawil; S. M. Abbas; A. E. – S. Abdel-Ghany; L. Bargnesi; C. Arbizzani; A. Mauger; C. M. Julien *Properties of Co-free Ni-Rich LiNi0.8Mn0.1Fe0.1O2 as Cathode Material for Lithium-Ion Batteries* Preprints 2024, 2024072320

In preparation:

L. Bargnesi, S. Santi, G. Fredi, M. Soccio, N. Lotti, A. Dorigato, C. Arbizzani, *Electrospun membranes of polyethylene furanoate derivatives for multi – purpose applications*

L. Bargnesi, T. Ivancic, N. Boaretto, I. Aldalur, D. Shanmukaraj, M. Martinez, M. Armand, C. Arbizzani, *Novel polymer electrolyte for greener and safer solid-state batteries*

Acknowledgments

Completing this thesis was only possible with the support of many different people and organizations.

First and foremost, I want to thank my supervisor Prof. Catia Arbizzani, who gave me the opportunity for continuous support during my first steps in the electrochemistry field. Thanks for being a brilliant supervisor who has given me many chances to grow. I want to thank all my colleagues in these years. We have spent many pleasant moments in the lab, and each of you has helped me complete this thesis and overcoming difficult moments in this years.

A special thank goes to Dr. Maria Martinez, who welcomed me in Vitoria-Gasteiz, making me feel at home. The Polymer electrolyte group at CIC Energigune is a constructive and unique environment in which I have worked with you having a lot of fun. Thanks to Dr. Itziar Aldalur, Dr. Nicola Boaretto, Dr. Leire Meabe and Dr. Devaraj Shanmukharaj, I will never forget your help and the constructive discussions with you.

In this regard, I would like to thank the Marco Polo programme for the funds that helped me during my time abroad in Spain.

A special thanks to Dr. Silvio Fugattini and Dr. Francesco Pagani and Manz Italy s.r.l. that kindly provided the equipment and expertise for lamination and membrane characterization tests.

8 Bibliography

1. Filonchyk, M. et al. Greenhouse gases emissions and global climate change: Examining the influence of CO2, CH4, and N2O. Science of the Total Environment vol. 935,173359 (2024).

2. Bhatti, U. A. et al. Global production patterns: Understanding the relationship between greenhouse gas emissions, agriculture greening and climate variability. Environ Res 245, (2024).

3. Hansen, J. et al. Assessing 'dangerous climate change': Required reduction of carbon emissions to protect young people, future generations and nature. PLoS One 8, (2013).

4. Nunes, L. J. R. The Rising Threat of Atmospheric CO2: A Review on the Causes, Impacts, and Mitigation Strategies. Environments - MDPI vol. 10(4), 66(2023).

5. Moss, R. H. et al. The next generation of scenarios for climate change research and assessment. Nature vol. 463 747–756 (2010).

6. Bellard, C.et al. Impacts of climate change on the future of biodiversity. Ecology Letters vol. 15 365–377 (2012).

7. UN Framework Convention Center on Climate Changes, ADOPTION OF THE PARIS AGREEMENT - Paris Agreement Text English.

8. Pandey, A. et al. Assessment of energy and environmental sustainability in South Asia in the perspective of the Sustainable Development Goals. Renewable and Sustainable Energy Reviews 165, (2022).

9.   Sharvini, S. R. et al. Energy consumption trends and their linkages with renewable energy policies in East and Southeast Asian countries: Challenges and opportunities. Sustainable Environment Research vol. 28 257–266 (2018).

10.   Harichandan, S. et al. Energy transition research: A bibliometric mapping of current findings and direction for future research. Cleaner Production Letters vol. 3, 100026 (2022).

11.   Burke, M. J. et al. Political power and renewable energy futures: A critical review. Energy Res Soc Sci 35, 78–93 (2018).

12.   Lawder, M. T. et al. Battery energy storage system (BESS) and battery management system (BMS) for grid-scale applications. Proceedings of the IEEE 102, 1014–1030 (2014).

13.   Khalid, M. Smart grids and renewable energy systems: Perspectives and grid integration challenges. Energy Strategy Reviews vol. 51, 101299 (2024).

14.   Tan, K. M. et al. Empowering smart grid: A comprehensive review of energy storage technology and application with renewable energy integration. Journal of Energy Storage vol. 39, 102591 (2021).

15.   Ulissi, U. et al. Past, present, and future of electrochemical energy storage: A brief perspective. in Frontiers of Nanoscience vol. 19 1–28 (2021).

16.   Zhang, S. S. Status, opportunities, and challenges of electrochemical energy storage. Frontiers in Energy Research vol. 1 (2013).

17.   Worku, M. Y. Recent Advances in Energy Storage Systems for Renewable Source Grid Integration: A Comprehensive Review. Sustainability (Switzerland) vol. 14 (2022).

18. Badwal, S. P. S. et al. Emerging electrochemical energy conversion and storage technologies. Frontiers in Chemistry vol. 2 (2014).

19. Schipper, F. et al. A brief review: Past, present and future of lithium ion batteries. Russian Journal of Electrochemistry 52, 1095–1121 (2016).

20. Masias, A. et al. Opportunities and Challenges of Lithium Ion Batteries in Automotive Applications. ACS Energy Letters vol. 6 621–630 (2021).

21. Itani, K. et al. A. Review on New-Generation Batteries Technologies: Trends and Future Directions. Energies vol. 16(22), 7530 (2023).

22. Wu, F. et al. Guidelines and trends for next-generation rechargeable lithium and lithium-ion batteries. Chemical Society Reviews vol. 49 1569–1614 (2020).

23. Arshad, F. et al. Life Cycle Assessment of Lithium-ion Batteries: A Critical Review. Resources, Conservation and Recycling vol. 180, 106164 (2022).

24. Yu, M. et al. Evaluating environmental impacts and economic performance of remanufacturing electric vehicle lithium-ion batteries. J Clean Prod 321, (2021).

25. Mrozik, W., Rajaeifar, M. A., Heidrich, O. & Christensen, P. Environmental impacts, pollution sources and pathways of spent lithium-ion batteries. Energy and Environmental Science vol. 14 6099–6121 (2021).

26. 2024 73rd Statistical Review of World Energy, Energy Institute (2024).

27. Kober, T. et al. Global energy perspectives to 2060 – WEC's World Energy Scenarios 2019. Energy Strategy Reviews 31, (2020).

28. 2017 International Energy Outlook, U.S. Energy Information Administration (2017)

29. Gür, T. M. Review of electrical energy storage technologies, materials and systems: Challenges and prospects for large-scale grid storage. Energy and Environmental Science vol. 11 2696–2767 (2018).

30. CO_2 Emissions in 2023, International Energy Agency (2023).

31. Lacis, A. A. et al. Atmospheric CO2: Principal Control Knob Governing Earth's Temperature. Science (1979) 330, 353–356 (2010).

32. Nikolaidis, P. et al. A Comparative Review of Electrical Energy Storage Systems for Better Sustainability Journal of Power Technologies 97 (3) 220-245 (2017).

33. IRENA (2024), Renewable capacity statistics 2024, International Renewable Energy Agency, Abu Dhabi.

34. Abdalla, O. H. 2016 Eighteenth International Middle-East Power Systems Conference (MEPCON) Proceedings : 27-29 December 2016, Helwan University, Cairo - Egypt. (IEEE, 2016).

35. Dell, R. M. et al. Energy Storage-a Key Technology for Global Energy Sustainability Journal of Power Sources 100 2–17 (2001).

36. Sayed, E. T. et al. Renewable Energy and Energy Storage Systems. Energies vol. 16(3) 1415 (2023).

37. Zhang, L. et al. Hybrid electrochemical energy storage systems: An overview for smart grid and electrified vehicle applications. Renewable and Sustainable Energy Reviews vol. 139 110581 (2021).

38. Yang, Z. et al. Electrochemical energy storage for green grid. Chemical Reviews vol. 111 3577–3613 (2011).

39. Liu, J. et al. Advanced Energy Storage Devices: Basic Principles, Analytical Methods, and Rational Materials Design. Advanced Science vol. 5 1700322 (2018).

40. Mitali, J. et al. Energy storage systems: a review. Energy Storage and Saving vol. 1 166–216 (2022).

41. Armand, M. & et al. Building Better Batteries Nature 451 652-657 (2008).

42. Biesheuvel, P. M. et al. Environmental Electrochemical Engineering. (Wageningen University & Research, 2023).

43. Bard, A. J. et al. Electrochemical Methods : Fundamentals and Applications. (John Wiley & Sons, Inc., 2001).

44. Winter, M. et al. What are batteries, fuel cells, and supercapacitors? Chem Rev 104, 4245–4269 (2004).

45. Dyer, C et al. Encyclopedia of Electrochemical Power Sources. 1st edition (2009).

46. Wakihara, M. et al. Lithium Ion Batteries Fundamentals and Performance. (1998).

47. Dunn, B. et al. Electrical energy storage for the grid: a battery of choices. Science. 334 928-35 (2011)

48. Shao, Y. et al. Design and Mechanisms of Asymmetric Supercapacitors. Chemical Reviews vol. 118 9233–9280 (2018).

49. Chen, Y. et al. A review of lithium-ion battery safety concerns: The issues, strategies, and testing standards. Journal of Energy Chemistry vol. 59 83–99 (2021).

50. Chen, R. et al. Advanced cathode materials for lithium-ion batteries using nanoarchitectonics. Nanoscale Horizons vol. 1 423–444 (2016).

51.   Jang, J. et al. A review of functional separators for lithium metal battery applications. Materials vol. 13 1–37 (2020).

52.   Huang, X. Separator technologies for lithium-ion batteries. Journal of Solid State Electrochemistry vol. 15 649–662 (2011).

53.   Huang, Q. et al. Thermal study on single electrodes in lithium-ion battery. J Power Sources 156, 541–546 (2006).

54.   Kaliaperumal, M. et al. Cause and mitigation of lithium-ion battery failure a review. Materials 14(19) (2021).

55.   Deng, D. Li-ion batteries: Basics, progress, and challenges. Energy Science and Engineering vol. 3 385–418 (2015).

56.   Abraham, K. M. Prospects and limits of energy storage in batteries. Journal of Physical Chemistry Letters vol. 6 830–844 (2015).

57.   Whittingham, M. S. et al. Fifty years of lithium-ion batteries and what is next? MRS Bulletin vol. 48 1118–1124 (2023).

58.   Ogumi, Z. et al. Lithium-Ion Batteries--The 25th Anniversary of Commercialization. Interface magazine 25, 65–65 (2016).

59.   Nykvist, B. et al. Rapidly falling costs of battery packs for electric vehicles. Nat Clim Chang 5, 329–332 (2015).

60.   Orangi, S. et al. Historical and prospective lithium-ion battery cost trajectories from a bottom-up production modeling perspective. J Energy Storage 76 109800 (2024).

61.   Liu, Y et al. iScience Perspective Current and future lithium-ion battery manufacturing. iScience 24, 102332 (2021).

62.   Zu, C. X. et al. Thermodynamic analysis on energy densities of batteries. Energy
        Environ Sci 4, 2614–2624 (2011).

63.   Obrovac, M. N. et al. Alloy negative electrodes for Li-ion batteries. Chemical Reviews
        vol. 114 11444–11502 (2014).

64.   Acebedo, B. et al. Current Status and Future Perspective on Lithium Metal Anode
        Production Methods. Advanced Energy Materials vol. 13 202203744 (2023).

65.   Cheng, X. B.et al. Toward Safe Lithium Metal Anode in Rechargeable Batteries: A
        Review. Chemical Reviews vol. 117 10403–10473 (2017).

66.   Adenusi, H. et al. Lithium Batteries and the Solid Electrolyte Interphase (SEI)—
        Progress and Outlook. Advanced Energy Materials vol. 13 2203307 (2023).

67.   Wang, X. et al. Stress-driven lithium dendrite growth mechanism and dendrite
        mitigation by electroplating on soft substrates. Nat Energy 3, 227–235 (2018).

68.   Goriparti, S. et al. Review on recent progress of nanostructured anode materials for
        Li-ion batteries. Journal of Power Sources vol. 257 421–443 (2014).

69.   Tao, R. et al. Kinetics Tuning the Electrochemistry of Lithium Dendrites Formation in
        Lithium Batteries through Electrolytes. ACS Appl Mater Interfaces 9, 7003–7008
        (2017).

70.   Manthiram, A. A reflection on lithium-ion battery cathode chemistry. Nature
        Communications vol. 11 1550 (2020).

71.   Goodenough, J. B. et al. Challenges for rechargeable Li batteries. Chemistry of
        Materials vol. 22 587–603 (2010).

72. Whittingham, M. S. Ultimate limits to intercalation reactions for lithium batteries. Chemical Reviews vol. 114 11414–11443 (2014).

73. Julien, C. M. et al. Comparative Issues of Cathode Materials for Li-Ion Batteries. Inorganics (Basel) 2, 132–154 (2014).

74. Murdock, B. E. et al. A Perspective on the Sustainability of Cathode Materials used in Lithium-Ion Batteries. Advanced Energy Materials vol. 11 2102028 (2021).

75. Xiang, J. et al. Building Practical High-Voltage Cathode Materials for Lithium-Ion Batteries. Advanced Materials vol. 34 2200912 (2022).

76. He, W. et al. Challenges and Recent Advances in High Capacity Li-Rich Cathode Materials for High Energy Density Lithium-Ion Batteries. Advanced Materials vol. 33 2005937 (2021).

77. Li, A. et al. A review on lithium-ion battery separators towards enhanced safety performances and modelling approaches. Molecules vol. 26(2) 478 (2021).

78. Chen, R.et al. The pursuit of solid-state electrolytes for lithium batteries: From comprehensive insight to emerging horizons. Materials Horizons vol. 3 487–516 (2016).

79. Xu, K. Electrolytes and interphases in Li-ion batteries and beyond. Chemical Reviews vol. 114 11503–11618 (2014).

80. Cheng, Z. et al. Recent advances in organic-inorganic composite solid electrolytes for all-solid-state lithium batteries. Energy Storage Materials vol. 34 388–416 (2021).

81. Zhang, H. et al. Single lithium-ion conducting solid polymer electrolytes: Advances and perspectives. Chemical Society Reviews vol. 46 797–815 (2017).

82. Turkson, C. et al. Sustainability assessment of energy production: A critical review of methods, measures and issues. Journal of Environmental Management vol. 264 (2020).

83. Schrijvers, D. et al. A review of methods and data to determine raw material criticality. Resources, Conservation and Recycling vol. 155 104617 (2020).

84. Ramasubramanian, B. et al. Ten major challenges for sustainable lithium-ion batteries. Cell Reports Physical Science vol. 5 102032 (2024).

85. Piątek, J. et al. Sustainable Li-Ion Batteries: Chemistry and Recycling. Advanced Energy Materials vol. 11 2003456 (2021).

86. Dühnen, S. et al. Toward Green Battery Cells: Perspective on Materials and Technologies. Small Methods vol. 4 2000039 (2020).

87. Pagliaro, M. et al. Lithium battery reusing and recycling: A circular economy insight. Heliyon vol. 5(6) (2019).

88. Fu, X. et al. Biomaterials for High-Energy Lithium-Based Batteries: Strategies, Challenges, and Perspectives. Advanced Energy Materials vol. 9 1901774 (2019).

89. Zhang, M. et al. Lignocellulosic materials for energy storage devices. Ind Crops Prod 203, (2023).

90. Dalwadi, S. et al. The Integration of Biopolymer-Based Materials for Energy Storage Applications: A Review. Int. J. Mol. Sci. 24(4), 3975 (2023).

91. Jeong, S. S. et al. Natural cellulose as binder for lithium battery electrodes. J Power Sources 199, 331–335 (2012).

92. Chen, Y. et al. Chitosan as a functional additive for high-performance lithium-sulfur batteries. J Mater Chem A Mater 3, 15235–15240 (2015).

93. Tang, K. et al. Advances of Carbon-Based Materials for Lithium Metal Anodes. Frontiers in Chemistry vol. 8 595972 (2020).

94. Jeschull, F. et al. Water-Soluble Binders for Lithium-Ion Battery Graphite Electrodes: Slurry Rheology, Coating Adhesion, and Electrochemical Performance. Energy Technology 5, 2108–2118 (2017).

95. Wu, Z. H. et al. Self-healing alginate–carboxymethyl chitosan porous scaffold as an effective binder for silicon anodes in lithium-ion batteries. Rare Metals 38, 832–839 (2019).

96. Zhu, P. et al. A review of current collectors for lithium-ion batteries. Journal of Power Sources vol. 485 229321 (2021).

97. Matsumoto, F. et al. Review of Current Collector-, Binder-, Conductive Additive-Free, and Freestanding Electrodes in Lithium and Related Batteries. Batteries vol. 10(9) 330 (2024).

98. Chen, C.H. et al Simple way of making free-standing cathode electrodes for flexible lithium-ion batteries RSC Adv. 12, 9249-9255 (2022)

99. Li, A. et al. A review on lithium-ion battery separators towards enhanced safety performances and modelling approaches. Molecules vol. 26(2) 478 (2021).

100. Zhang, J. et al. Sustainable, heat-resistant and flame-retardant cellulose-based composite separator for high-performance lithium ion battery. Sci Rep 4, (2014).

101. Zhang, T. W. et al. Prawn shell derived chitin nanofiber membranes as advanced sustainable separators for Li/Na-Ion Batteries. Nano Lett 17, 4894–4901 (2017).

102. Tan, L. et al. Preparation and Properties of an Alginate-Based Fiber Separator for Lithium-Ion Batteries. ACS Appl Mater Interfaces 12, 38175–38182 (2020).

103. Reizabal, A. et al. Silk fibroin and sericin polymer blends for sustainable battery separators. J Colloid Interface Sci 611, 366–376 (2022).

104. Huang, J. et al. Recent Progress of Rechargeable Batteries Using Mild Aqueous Electrolytes. Small Methods vol. 3 1800272 (2019).

105. Bresser, D. et al. Alternative binders for sustainable electrochemical energy storage-the transition to aqueous electrode processing and bio-derived polymers. Energy Environ Sci 11, 3096–3127 (2018).

106. Bouguern, M. D. et al. Engineering Dry Electrode Manufacturing for Sustainable Lithium-Ion Batteries. Batteries vol. 10(1) 39 (2024).

107. Lizundia, E. et al. Advances in Natural Biopolymer-Based Electrolytes and Separators for Battery Applications. Advanced Functional Materials vol. 31 2005646 (2021).

108. Barbosa, J. C. et al. Toward Sustainable Solid Polymer Electrolytes for Lithium-Ion Batteries. ACS Omega vol. 7 14457–14464 (2022).

109. Li, J. et al. From Materials to Cell: State-of-the-Art and Prospective Technologies for Lithium-Ion Battery Electrode Processing. Chemical Reviews vol. 122 903–956 (2022).

110. Wood, D. L. et al. Prospects for reducing the processing cost of lithium ion batteries. J Power Sources 275, 234–242 (2015).

111. Loeffler, N. et al. In Situ Coating of Li[Ni0.33Mn0.33Co0.33]O2 Particles to Enable Aqueous Electrode Processing. ChemSusChem 9, 1112–1117 (2016).

112. Du, Z. et al. Enabling aqueous processing for crack-free thick electrodes. J Power Sources 354, 200–206 (2017).

113. Kvasha, A. et al. Towards high durable lithium ion batteries with waterborne LiFePO4 electrodes. Electrochim Acta 215, 238–246 (2016).

114. Salini, P. S. et al. Toward Greener and Sustainable Li-Ion Cells: An Overview of Aqueous-Based Binder Systems. ACS Sustainable Chemistry and Engineering vol. 8 4003–4025 (2020).

115. Yoon, J. et al. Polymeric Binder Design for Sustainable Lithium-Ion Battery Chemistry Polymers 16(2), 254 (2024)

116. Costa, C. M., Lizundia, E. & Lanceros-Méndez, S. Polymers for advanced lithium-ion batteries: State of the art and future needs on polymers for the different battery components. Progress in Energy and Combustion Science vol. 79 Preprint at https://doi.org/10.1016/j.pecs.2020.100846 (2020).

117. Varoon, K. et al. Dispersible exfoliated zeolite nanosheets and their application as a selective membrane. Science (1979) 334, 72–75 (2011).

118. Han, L. et al. Undervalued Roles of Binder in Modulating Solid Electrolyte Interphase Formation of Silicon-Based Anode Materials. ACS Applied Materials and Interfaces vol. 13 45139–45148 (2021).

119. Chen, H. et al. Exploring Chemical, Mechanical, and Electrical Functionalities of Binders for Advanced Energy-Storage Devices. Chemical Reviews vol. 118 8936–8982 (2018).

120. Zhang, L. et al. Exploring More Functions in Binders for Lithium Batteries. Electrochemical Energy Reviews vol. 6(36) (2023).

121. Cho, K. Y. et al. Evaluation of slurry characteristics for rechargeable lithium-ion batteries. Mater Res Bull 48, 2922–2926 (2013).

122. Yang, H. et al. Ionic conductivity and ion transport mechanisms of solid-state lithium-ion battery electrolytes: A review. Energy Science and Engineering vol. 10 1643–1671 (2022).

123. Chen, J.et al. Unveiling the Roles of Binder in the Mechanical Integrity of Electrodes for Lithium-Ion Batteries. J Electrochem Soc 160, A1502–A1509 (2013).

124. Brennan, N. M. et al. Trends in the regulation of per-and polyfluoroalkyl substances (PFAS): A scoping review. International Journal of Environmental Research and Public Health vol. 18 10900 (2021).

125. Zhong, L. et al. Poly(Acrylic Acid)-Based Polymer Binders for High-Performance Lithium-Ion Batteries: From Structure to Properties. Small 20 2407297 (2024).

126. Qiu, L. et al. Carboxymethyl cellulose lithium (CMC-Li) as a novel binder and its electrochemical performance in lithium-ion batteries. Cellulose 21, 2789–2796 (2014).

127. Zhang, L. et al. Chitosan, a new and environmental benign electrode binder for use with graphite anode in lithium-ion batteries. Electrochim Acta 105, 378–383 (2013).

128. Zhang, S. J. et al. Sodium-Alginate-Based Binders for Lithium-Rich Cathode Materials in Lithium-Ion Batteries to Suppress Voltage and Capacity Fading. ChemElectroChem 5, 1321–1329 (2018).

129. Lingappan, N. et al. The significance of aqueous binders in lithium-ion batteries. Renewable and Sustainable Energy Reviews vol. 147 111227 (2021).

130. Rasheed, T. et al. Biopolymer Based Materials as Alternative Greener Binders for Sustainable Electrochemical Energy Storage Applications. ChemistrySelect vol. 7 e202203202 (2022).

131. von Wald Cresce, A. et al. Aqueous lithium-ion batteries. Carbon Energy vol. 3 721–751 (2021).

132. Han, J. et al. Fluorine-Free Water-in-Salt Electrolyte for Green and Low-Cost Aqueous Sodium-Ion Batteries. ChemSusChem 11, 3704–3707 (2018).

133. Ahn, H. et al. Challenges and possibilities for aqueous battery systems. Communications Materials vol. 4 37 (2023).

134. Dubal, D. P. et al. Hybrid energy storage: The merging of battery and supercapacitor chemistries. Chemical Society Reviews vol. 44 1777–1790 (2015).

135. González, A. et al.Review on supercapacitors: Technologies and materials. Renewable and Sustainable Energy Reviews vol. 58 1189–1206 (2016).

136. Chaudhary, S. et al. A review on the different types of electrode materials for aqueous supercapacitor applications. Advances in Natural Sciences: Nanoscience and Nanotechnology 12, (2021).

137. Zhong, C. et al. A review of electrolyte materials and compositions for electrochemical supercapacitors. Chemical Society Reviews vol. 44 7484–7539 (2015).

138. Sharma, S. et al. Supercapacitor and electrochemical techniques: A brief review. Results in Chemistry vol. 5 100885 (2023).

139. Zhang, Y. et al. Progress of electrochemical capacitor electrode materials: A review. International Journal of Hydrogen Energy vol. 34 4889–4899 (2009).

140. Ricketts, B. W. et al. Self-Discharge of Carbon-Based Supercapacitors with Organic Electrolytes. Journal of Power Sources vol. 89 64-69 (2000).

141. Wei, Y. Z. et al. A novel electrode material for electric double-layer capacitors. J Power Sources 141, 386–391 (2005).

142. Zhang, H. et al. Carbon nanotube arrays and their composites for electrochemical capacitors and lithium-ion batteries. Energy Environ Sci 2, 932–943 (2009).

143. Mendhe, A. et al. A review on electrolytes for supercapacitor device. Discover Materials vol. 3 29 (2023).

144. Béguin, F. et al. Carbons and electrolytes for advanced supercapacitors. Advanced Materials 26, 2219–2251 (2014).

145. Wang, G. et al. A review of electrode materials for electrochemical supercapacitors. Chem Soc Rev 41, 797–828 (2012).

146. Kötz, R. et al. Principles and Applications of Electrochemical Capacitors. Electrochimica Acta vol. 45 2483-2498 (2000).

147. Pandolfo, A. G. et al. Carbon properties and their role in supercapacitors. Journal of Power Sources vol. 157 11–27 (2006).

148. Sajjad, M. et al. A review on selection criteria of aqueous electrolytes performance evaluation for advanced asymmetric supercapacitors. Journal of Energy Storage vol. 40 102729 (2021).

149. Bargnesi, L. et al. Sustainable Modification of Chitosan Binder for Capacitive Electrodes Operating in Aqueous Electrolytes. ChemElectroChem 10, e202201080 (2023).

150. Bargnesi, L. et al. Crosslinked Chitosan Binder for Sustainable Aqueous Batteries. Nanomaterials 12(2) 254 (2022).

151. Pal, B. et al. Electrolyte selection for supercapacitive devices: A critical review. Nanoscale Adv 1, 3807–3835 (2019).

152. Kim, H. et al. Aqueous rechargeable Li and Na ion batteries. Chemical Reviews vol. 114 11788–11827 (2014).

153. Suo, L. et al. 'water-in-Salt' electrolytes enable green and safe Li-ion batteries for large scale electric energy storage applications. J Mater Chem A Mater 4, 6639–6644 (2016).

154. Frackowiak, E. et al. Carbon Materials for the Electrochemical Storage of Energy in Capacitors. Carbon vol. 39(6) 937-950 (2001).

155. Frackowiak, E. Carbon materials for supercapacitor application. Physical Chemistry Chemical Physics 9, 1774–1785 (2007).

156. Lagadec, M. F. et al. Characterization and performance evaluation of lithium-ion battery separators. Nature Energy vol. 4 16–25 (2019).

157. Huang, X. et al. Lithium ion battery separators: Development and performance characterization of a composite membrane. J Memb Sci 425–426, 163–168 (2013).

158. Lee, H. et al. A review of recent developments in membrane separators for rechargeable lithium-ion batteries. Energy and Environmental Science vol. 7 3857–3886 (2014).

159. Arora, P. et al. Battery separators. Chem Rev 104, 4419–4462 (2004).

160. Tanji, H. Secondary batteries-Lithium Rechargeable Systems-Lithium ion Separators Encyclopedia of Electrochemical Power Sources, 2009

161. Heidari, A. A. et al. Recent Development of Polyolefin-Based Microporous Separators for Li−Ion Batteries: A Review. Chemical Record vol. 20 570–595 (2020).

162. Luiso, S. et al. Lithium-ion battery separators: Recent developments and state of art. Current Opinion in Electrochemistry vol. 20 99–107 (2020).

163. Li, Y. et al. Polypropylene/polyethylene multilayer separators with enhanced thermal stability for lithium-ion battery via multilayer coextrusion. Electrochim Acta 264, 140–149 (2018).

164. Hou, Y. et al. Bifunctional separators design for safe lithium-ion batteries: Suppressed lithium dendrites and fire retardance. Nano Energy 97, (2022).

165. Gullace, S. et al. Covalent organic framework-based Li-S batteries: functional separators promoting Li+ transport and polysulfide trapping. J. Mater. Chem. A 12, 25359-25370 (2024)

166. Sheng, L. et al. A tailored ceramic composite separator with electron-rich groups for high-performance lithium metal anode. J Memb Sci 657, (2022).

167. Deimede, V. et al. Separators for Lithium-Ion Batteries: A Review on the Production Processes and Recent Developments. Energy Technology 3, 453–468 (2015).

168. Schilling, A.et al. Analyzing Bending Stresses on Lithium-Ion Battery Cathodes induced by the Assembly Process. Energy Technology 4, 1502–1508 (2016).

169. Kim, N. et al. Electrode Alignment: Ignored but Important Design Parameter in Assembling Coin-Type Full Lithium-Ion Cells. J Electrochem Soc 169, 023502 (2022).

170. Leithoff, R. et al. Process-Product Interdependencies in Lamination of Electrodes and Separators for Lithium-Ion Batteries. Energies (Basel) 15, (2022).

171. Zhong, S. et al. Recent progress in thin separators for upgraded lithium ion batteries. Energy Storage Materials vol. 41 805–841 (2021).

172. Lin, D. et al. All-Integrated Bifunctional Separator for Li Dendrite Detection via Novel Solution Synthesis of a Thermostable Polyimide Separator. J Am Chem Soc 138, 11044–11050 (2016).

173. Waqas, M. et al. Recent Development in Separators for High-Temperature Lithium-Ion Batteries. Small vol. 15 1901689 (2019).

174. Kritzer, P. Nonwoven support material for improved separators in Li-polymer batteries. J Power Sources 161, 1335–1340 (2006).

175. Yi, W. et al. Wet-laid non-woven fabric for separator of lithium-ion battery. J Power Sources 189, 616–619 (2009).

176. Truong, Y. B. et al. Electrospun poly(vinylidene fluoride)-lithium bistrifluoromethanesulfonamide separators for applications in ionic liquid batteries. Aust J Chem 66, 252–261 (2013).

177. Xu, M. et al. Electrospun-Technology-Derived High-Performance Electrochemical Energy Storage Devices. Chemistry - An Asian Journal vol. 11 2967–2995 (2016).

178. Orendorff, C. J. et al. Polyester separators for lithium-ion cells: Improving thermal stability and abuse tolerance. Adv Energy Mater 3, 314–320 (2013).

179. Li, Z. et al. Preparation and application of a high-temperature–resistant EVOH-SO3Li/PI fiber membrane with self-closing pores. High Perform Polym 32, 1102–1111 (2020).

180. Jung, S. J. et al. Dimethylacetamide-induced hepatic injuries among spandex fibre workers. Clin Toxicol 45, 435–439 (2007).

181. Yan, N. et al. Shutdown-Functionalized Poly Ethylene-Vinyl Alcohol Sulfonate Lithium and Poly (Vinyl Alcohol) Composite Lithium-Ion Battery Separator. J Electrochem Soc 168, 110510 (2021).

182. Zou, M. et al. High-performance electrospun membrane for lithium-ion batteries. J Memb Sci 637, (2021).

183. Emblem, A. Plastics properties for packaging materials. in 13 Packaging Technology 287–309 (Elsevier, 2012).

184. Rosato, D. V. Plastic Product Material and Process Selection Handbook in 4 Injection molding 192-226 (Elsevier, 2004)

185. McKeen, L. W. Permeability Properties of Plastics and Elastomers in 9 Polyolefins, Polyvinyls, and Acrylics. (2016).

186. Pérez-Blanco, C. et al. Characterization, biodegradation and cytotoxicity of thermoplastic starch and ethylene-vinyl alcohol copolymer blends. Carbohydr Polym 298 120085 (2022).

187. Kenawy, E.-R. et al. Electrospinning of Poly(Ethylene-Co-Vinyl Alcohol) Fibers. Biomaterials vol. 24(6) 907-913 (2003).

188. Xia, L. et al. Ethylene-vinyl alcohol copolymer/gelatin/cellulose acetate bionic trilayer fibrous membrane for moisture-adjusting. Carbohydr Polym 300(15) 120269 (2023).

189. Wang, X. L. et al. Preparation and properties of biodegradable polymeric blends from poly(propylene carbonate) and poly(ethylene-co-vinyl alcohol). J Biomed Mater Res B Appl Biomater 83, 373–379 (2007).

190. Tang, Y. et al. A review on models and simulations of membrane formation via phase inversion processes. Journal of Membrane Science vol. 640 119810 (2021).

191. Hołda, A. K. et al. Understanding and guiding the phase inversion process for synthesis of solvent resistant nanofiltration membranes. J Appl Polym Sci 132 42130 (2015).

192. Roudaut, G. et al. Molecular mobility around the glass transition temperature: A mini review. Innovative Food Science and Emerging Technologies vol. 5 127–134 (2004).

193. Diab, M. A. et al. Thermal stability and degradation of chitosan modified by benzophenone. Spectrochim Acta A Mol Biomol Spectrosc 79, 1057–1062 (2011).

194. Neto, C. G. T. et al. Thermal analysis of chitosan based networks. Carbohydr Polym 62, 97–103 (2005).

195. Lagarón, J. M. et al. Phase Morphology, Crystallinity and Mechanical Properties of Binary Blends of High Barrier Ethylene-vinyl Alcohol Copolymer and Amorphous Polyamide and a Polyamide-Containing Ionomer Polymer vol. 42(17) 7381-7394 (2001)

196. Mathot, V. B. F. et al. Dynamic DSC, SAXS and WAXS on homogeneous ethylene-propylene and ethylene-octene copolymers with high comonomer contents. Journal of Thermal Analysis 46, 681–718 (1996)

197. Wu, Y. S. et al. PVDF-HFP/PET/PVDF-HFP composite membrane for lithium-ion power batteries. Int J Hydrogen Energy 42, 6862–6875 (2017).

198. Ciurduc, D. E. et al. Development of high performing polymer electrolytes based on superconcentrated solutions. J Power Sources 506, 230220 (2021).

199. Liu, F. et al. Recent developments in natural mineral-based separators for lithium-ion batteries. RSC Advances vol. 11 16633–16644 (2021).

200. Kaden, N. et al. A Systematic Literature Analysis on Electrolyte Filling and Wetting in Lithium-Ion Battery Production. Batteries vol. 9(3) 164 (2023).

201. Zhu, G.-L. et al. Dependence of Separator Thickness on Li-Ion Battery Energy Density. J Electrochem Soc 168, 110545 (2021).

202. Wu, M. et al. Comparative analysis of different separators for the electrochemical performances and long-term stability of high-power lithium-ion batteries. Ionics 27, 1551–1558 (2021).

203. Dermeik, B. et al. Highly Filled Papers, on their Manufacturing, Processing, and Applications. Advanced Engineering Materials vol. 21 1900180 (2019).

204. Terella, A. et al. Functional separators for the batteries of the future. J Power Sources 449(15) 227556 (2020).

205. Di Cillo et al. Ammonium and Tetraalkylammonium Salts as Additives for Li Metal Electrodes. Batteries 9(2) 142 (2023).

206. Dahbi, M. et al. Comparative study of EC/DMC LiTFSI and LiPF6 electrolytes for electrochemical storage. J Power Sources 196, 9743–9750 (2011).

207. An, H. et al. Separator Dependency on Cycling Stability of Lithium Metal Batteries Under Practical Conditions. Energy and Environmental Materials 6, (2023).

208. Barton J. L. et al. The electrolytic growth of dendrites from ionic solutions Proc. R. Soc. Lond. A268485–505 (1962)

209. Lung-Hao Hu, B. et al. Graphene-modified LiFePO4 cathode for lithium ion battery beyond theoretical capacity. Nat Commun 4 1687 (2013).

210. Dai, Z. et al. Nafion/PEG hybrid membrane for CO2 separation: Effect of PEG on membrane micro-structure and performance. Sep Purif Technol 214, 67–77 (2019).

211. Lim, D. H. et al. Polymer electrolytes based on poly(vinylidene fluoride-co-hexafluoropropylene) nanofibrous membranes containing polymer plasticizers for lithium batteries. in Solid State Ionics vol. 225 631–635 (2012).

212. Menkin, S. et al. Insights into soft short circuit-based degradation of lithium metal batteries. Faraday Discuss 248, 277–297 (2023).

213. Fei, X. et al. Biobased Poly(ethylene 2,5-furancoate): No Longer an Alternative, but an Irreplaceable Polyester in the Polymer Industry. ACS Sustainable Chemistry and Engineering vol. 8 8471–8485 (2020).

214. Pellis, A., et al. Renewable polymers and plastics: Performance beyond the green. New Biotechnology vol. 60 146–158 (2021).

215. Soccio, M. et al. Novel fully biobased poly(butylene 2,5-furanoate/diglycolate) copolymers containing ether linkages: Structure-property relationships. Eur Polym J 81, 397–412 (2016).

216. Laurita, R. et al. Plasma Processing of Electrospun Li-Ion Battery Separators to Improve Electrolyte Uptake. Plasma Processes and Polymers 13, 124–133 (2016).

217. Yerkinbekova, Y. et al. Photo-crosslinked lignin/PAN electrospun separator for safe lithium-ion batteries. Sci Rep 12 18272 (2022).

218. Zhao, L. et al. Electrolyte-Wettability Issues and Challenges of Electrode Materials in Electrochemical Energy Storage, Energy Conversion, and Beyond. Advanced Science vol. 10 2300283 (2023).

219. Zheng, H. et al. A comprehensive understanding of electrode thickness effects on the electrochemical performances of Li-ion battery cathodes. Electrochim Acta 71, 258–265 (2012).

220. Armand, M. The History of Polymer Electrolytes. Solid State Ionics Vol.69(3-4) 309-319 (1994).

221. Chattopadhyay, J. et al. Applications of Polymer Electrolytes in Lithium-Ion Batteries: A Review. Polymers vol. 15(19) 3907 (2023).

222. Zhou, D. et al. Polymer Electrolytes for Lithium-Based Batteries: Advances and Prospects. Chem vol. 5 2326–2352 (2019).

223. Chae, W. et al. A Brief Review of Gel Polymer Electrolytes Using In Situ Polymerization for Lithium-ion Polymer Batteries. Polymers vol. 15(4) 803 (2023).

224. Fergus, J. W. Ceramic and polymeric solid electrolytes for lithium-ion batteries. Journal of Power Sources vol. 195 4554–4569 (2010).

225. Sashmitha, K. et al. A comprehensive review of polymer electrolyte for lithium-ion battery. Polymer Bulletin vol. 80 89–135 (2023).

226. Kainat, S., et al. Electrolytes in Lithium-Ion Batteries: Advancements in the Era of Twenties (2020's). Materials Chemistry and Physics vol. 313 128796 (2024).

227. Sharma, A. L. et al. Polymer-ion-clay interaction based model for ion conduction in intercalation-type polymer nanocomposite. Ionics (Kiel) 16, 339–350 (2010).

228. Shan, C. et al. A comprehensive review of single ion-conducting polymer electrolytes as a key component of lithium metal batteries: From structural design to applications. Energy Storage Materials vol. 63102955 (2023).

229. Li, J. et al. Review of electrolyte strategies for competitive dual-ion batteries. Materials Today Sustainability 19, 100188 (2022).

230. Fan, P. et al. High Performance Composite Polymer Electrolytes for Lithium-Ion Batteries. Advanced Functional Materials vol. 31 2101380 (2021).

231. Li, J. et al. Polymers in Lithium-Ion and Lithium Metal Batteries. Advanced Energy Materials vol. 11 2003239 (2021).

232. Stolz, L. et al. Single-Ion versus Dual-Ion Conducting Electrolytes: The Relevance of Concentration Polarization in Solid-State Batteries. ACS Appl Mater Interfaces 14, 11559–11566 (2022).

233. Yang, H. et al. Ionic conductivity and ion transport mechanisms of solid-state lithium-ion battery electrolytes: A review. Energy Science and Engineering vol. 10 1643–1671 (2022).

234. Ratner, M.A. et al. Polymer Electrolytes: Ionic Transport Mechanisms and Relaxation Coupling. MRS Bulletin 25, 31–37 (2000)

235. Liu, Z. et al. Lithium-ion transport in covalent organic framework membrane. Chemical Engineering Journal 433(2) 133550 (2022).

236. Aziz, S. B. et al. A conceptual review on polymer electrolytes and ion transport models. Journal of Science: Advanced Materials and Devices vol. 3 1–17 (2018).

237. Wang, W. M. Study on all solid-state composite polymer electrolyte. in Advanced Materials Research vol. 571 13–16 (2012).

238. Meyer, W. H. Polymer Electrolytes for Lithium-Ion Batteries. Adv. Mater. 10 439-448 (1998)

239. Bruce, P.G. Structure and electrochemistry of polymer electrolytes Electrochim Acta 40(13-14) 2077-2085 (1995)

240. Chen, A. et al. Manufacturing Strategies for Solid Electrolyte in Batteries. Frontiers in Energy Research vol. 8 571440 (2020).

241. Li, Z. et al. Scalable fabrication of Solvent-Free composite solid electrolyte by a continuous Thermal-Extrusion process. J Colloid Interface Sci 628, 64–71 (2022).

242. Otake, Y. et al. Effects of Molecular Structure of Cross-Linked Solid Polymer Electrolytes on Ionic Conduction Behavior. J Electrochem Soc 170, 040510 (2023).

243. Ghazali, N. M. et al. Progress on biopolymer as an application in electrolytes system: A review study. in Materials Today: Proceedings vol. 49 3668–3678 (2020).

244. Buraidah, M. H. et la. Characterization of chitosan/PVA blended electrolyte doped with NH 4I. J Non Cryst Solids 357, 3261–3266 (2011).

245. Barbosa, J. C. et al. Toward Sustainable Solid Polymer Electrolytes for Lithium-Ion Batteries. ACS Omega vol. 7 14457–14464 (2022).

246. Mazuki, N. F. et al. An investigation on the abnormal trend of the conductivity properties of CMC/PVA-doped NH4Cl-based solid biopolymer electrolyte system. Ionics (Kiel) 25, 2657–2667 (2019).

247. Vieira, D. F. et al. Conductivity study of a gelatin-based polymer electrolyte. Electrochim Acta 53, 1404–1408 (2007).

248. Fuzlin, A. F. et al. Studies on favorable ionic conduction and structural properties of biopolymer electrolytes system-based alginate. Polymer Bulletin 78, 2155–2175 (2021).

249. Hadad, S. et al. Starch acetate and carboxymethyl starch as green and sustainable polymer electrolytes for high performance lithium ion batteries. Appl Energy 324, 119767 (2022).

250. Lizundia, E. et al. Advances in Natural Biopolymer-Based Electrolytes and Separators for Battery Applications. Advanced Functional Materials vol. 31 2005646 (2021).

251. Aldalur, I. et al. Jeffamine-Based Polymers for Rechargeable Batteries. Batteries and Supercaps vol. 3 30–46 (2020).

252. Bar, H. et al. Modification of shellac coating using Jeffamine® for enhanced mechanical properties and stability. Prog Org Coat 141, 105559 (2020).

253. Ranque, P. et al. Feasibility of Multifunctional Cellulose-Based Polysalt as a Polymer Matrix for Li Metal Polymer Batteries. ACS Appl Mater Interfaces 15, 51089–51099 (2023).

254. Hu, J. et al. Solid polymer electrolyte based on ionic bond or covalent bond functionalized silica nanoparticles. RSC Adv 7, 54986–54994 (2017).

255. Lai, H. L. et al. Characterisation of the thermal properties of ethylcellulose using differential scanning and quasi-isothermal calorimetric approaches. Int J Pharm 386, 178–184 (2010).

256. Li, Z. et al. Ionic Conduction in Polymer-Based Solid Electrolytes. Advanced Science vol. 10 2201718 (2023).

257. Olmedo-Martínez, J. L. et al. Effect of chemical structure and salt concentration on the crystallization and ionic conductivity of aliphatic polyethers. Polymers (Basel) 11(3), 452 (2019).

258. Piszcz, M. et al. New Single Ion Conducting Blend Based on PEO and PA-LiTFSI. Electrochim Acta 255, 48–54 (2017).

259. Evans, J., Vincent et al. Electrochemical Measurement of Transference Numbers in Polymer Electrolytes Polymer, 28(13) 2324-2328

260. Porcarelli, L. et al. Single-Ion Conducting Polymer Electrolytes for Lithium Metal Polymer Batteries that Operate at Ambient Temperature. ACS Energy Lett 1, 678–682 (2016).

261. Luo, Y. et al. A new review of single-ion conducting polymer electrolytes in the light of ion transport mechanisms. Journal of Energy Chemistry vol. 89 543–556 (2024).

262. Zuo, X. et al. Self-supporting ethyl cellulose/poly(vinylidene fluoride) blended gel polymer electrolyte for 5 V high-voltage lithium-ion batteries. Electrochim Acta 271, 582–590 (2018).